A METHOD FOR EVALUATING THE EFFECTS OF STRESSES AND ROCK STRENGTH ON FLUID FLOW ALONG THE SURFACES OF MECHANICAL DISCONTINUITIES IN LOW PERMEABILITY ROCKS

BY

MILTON BOCK ENDERLIN

Bachelor of Science, 1977
Sonoma State University
Rohnert Park, California

Submitted to the Graduate Faculty of the
College of Science and Engineering
Texas Christian University
In partial fulfillment of the requirements for the degree of

MASTER OF SCIENCE

December, 2010

ACKNOWLEDGEMENTS

I would like to express sincere appreciation to my advisor and committee chairman, Dr. Helge Alsleben, for his guidance, criticisms, support, incredible patience and good sense of humor throughout this effort. I also wish to acknowledge the valuable contributions of the other committee members, Dr. John Breyer and Dr. Chris Zahm. In addition, I would like to thank Marvin Gearhart and the Gearhart Companies for providing the opportunity to make this project possible. I am grateful to the management and staff of ConocoPhillips Rock Mechanics Laboratories; in particular to Rico Ramos, David Chancellor and Teri Nichols.

Appreciation is due to Dr. Mark Zoback, Dr. Dan Moos, and Dr. Colleen Barton for starting me down this adventure and providing support and inspiration along the way.

I would like to acknowledge the TCU geology faculty and staff for a great graduate education. I have enjoyed my graduate experience at TCU.

I am thankful for the support of my daughters Ashley and Shelby and my father George W. Enderlin.

My gratitude seems inadequate for the love and support of my wife Vicky, but I am truly grateful nevertheless. I dedicate this thesis to her.

TABLE OF CONTENTS

LIST OF FIGURES

LIST OF TABLES

INTRODUCTION

Structurally, rocks respond to changes in confining stress by compacting, fracturing, faulting or folding. The consequence of an evolving stress and deformation history provides the potential for the development of folds and mechanical discontinuities with differing orientations. Chemical processes can alter rock cohesion and orientation-sensitive flow characteristics (Laubach et al., 2004) particularly in carbonate rocks. Here, I will only consider siliceous rocks that are strong (unconfined compressive strength, UCS >8000 psi (~55 MPa): see Table 1 for common abbreviations), fairly homogeneous and have nearly cohesionless mechanical discontinuities, such as fault, fractures, and bedding planes. I will address the question of how the mechanical discontinuities are oriented with respect to contemporary stress state and how that may encourage fluid flow along their surfaces.

One approach to answering this question is to first understand present-day state of stress (S) in terms of overburden stress (S_V), maximum horizontal stress (S_H), minimum horizontal stress (S_h), and pore pressure (P_p). If these properties, their orientation, and the orientation of existing mechanical discontinuities are known, then normal and shear stresses on these surfaces can be estimated. Typically, high normal stress discourages fluid flow (Bandis et al., 1983; Gidley et al., 1989; Gutierrez et al., 2000). However, if the shear stress magnitude is enough to overcome the product of the surface's coefficient of sliding friction and normal stress, the surface could fail in shear and slide, which is here referred to as *reactivation*. Reactivation will tend to dilate the discontinuity by mis-matching asperities along the surface, opening the discontinuity's aperture and, thereby, encouraging the flow of fluids (Barton et al., 1995; Gutierrez et al., 2000; Zoback, 2007). The following discussion will be limited to ultra-

Table 1. Common abbreviations used in text.

A	Atomic weight
AE	Acoustic Emissions
Amax	Largest aperture within a fracture
ARF	Angle between the axial stress and plane which best described rock failure
B_{ij}	Directional cosine term
BO	Breakout
cm	Centimeters
Co	Cohesion
DP	Pressure gradient
DTc	Compressional slowness (micro seconds per foot, μsec/ft)
DTs	Shear slowness (micro seconds per foot, μsec/ft)
E	Young's modulus
IFA	Internal Friction Angle
K_f	Permeability of a fracture
L	Fracture length
LOT	Leak off test
m	Meter
MaxHoop	Maximum hoop stress
m_{bfexl}	Slope of best fit extrapolated line on the plot of axial stress at failure and confining stress
MD	Measured depth
mL	Milliliter
min	Minute
MinHoop	Minimum hoop stress
MPa	Megapascal
n	Viscosity
NF	Normal fault
Pf, P_f	Pressure within a fracture or fault
Pfr, P_{fr}	Pressure within a fracture required for reactivation
Pi	3.1416
Pm, P_m	Pressure exerted by drilling fluids
Pp, P_p	Pore pressure
ppg	Pounds per gallon
psi	Pounds per square inch
PSSF	Patchy stick-slip flow
Q	Flow rate
RF	Reverse fault
Rhob, Rho_b	Bulk density (grams per cubic centimeter, g/cm^3)
avRho_b	Average bulk density
Rhog	Grain density (grams per cubic centimeter, g/cm^3)
S	Stress
Sc'	Effective confining stress

Table 1 (continued). Common abbreviations used in text.

SH, S_H	Maximum horizontal stress
SHaz, S_{Haz}	Azimuth of S_H measured clockwise from north to the direction of S_H
Sh, S_h	Minimum horizontal stress
Sn	Normal stress
Sn’	Effective normal stress
Ss	Shear stress
SS	Strike-slip fault
SV, S_V	Overburden stress
Sw	Water saturation
S1, S2, S3	Principal stresses
S_1, S_2, S_3	Principal stresses
TC	Tensile crack
TVD	True vertical depth
u (μ)	Coefficient of sliding friction
UCS	Unconfined Compressive Strength
US	Ultimate Strength
v	Poisson’s ratio
Vclay	Volume clay
Vshale	Volume shale
W	Distance between two parallel plates, Fracture Width, Fracture Aperture
Z	Atomic number

low permeability rock, implying a low "leak-off" of fluids and pressure. In this way, a difference can exist between the pressures in the rock matrix pores (P_p) and pressure within the fracture plane (P_f) over the time frames of drilling, completion and production.

The methodology will be presented in three segments: approach and background, flow experiment, and application. The objective of the flow experiment is to replicate the approach in a laboratory setting whereas the application section provides a field example that shows the usefulness of the approach.

APPROACH AND BACKGROUND

Definitions and Concepts:

Pressure and stress are forces per a unit area (e.g., pounds per square inch). Here, the units of stress and pressure will be given in both English "oil field" and SI units (pounds per square inch = psi, and megapascal = MPa, where 1MPa = 145.038 psi). When referring to the change of stress and pressure with vertical depth (in feet = ft), the units of psi/ft and pounds per gallon (ppg) will be used (1 psi/ft is ~19.25 ppg). Positive values are used to denote compressive stress and shortening strain, whereas negative values denote tensional stress and lengthening strain. The directionality of stress is represented by the combination of three mutually orthogonal components; two of which reside in the horizontal plane, while the third is vertical. The vertical stress component is S_V, while the two components in the horizontal plane, are the maximum (S_H) and minimum (S_h) horizontal stresses. "Minimum" and "maximum" refer to their relative magnitudes ($S_H > S_h$), with no inference to how they may compare to S_V. The above stresses are related to the principal stresses (S_1, S_2, and S_3 where $S_1 \geq S_2 \geq S_3$), which are also represented in a mutually orthogonal coordinate system. Following Anderson's

theory of faulting (Anderson, 1951), one of the three principal stresses will be vertical, pointing to the center of the Earth. How S_1, S_2, and S_3 are related to S_V, S_H, and S_h will be discussed in detail later.

To describe the state of stress in the subsurface, four parameters need to be defined: the magnitude of S_V (which corresponds to the weight of the overburden), the magnitude of S_h, the magnitude of S_H, and the azimuth of S_H (S_{Haz}). To understand how the state of stress affects the rock matrix, we must also know the magnitude of the pressure within the pores (the quotient of pore volume and bulk volume is often referred to as "porosity") of the rocks, since the effective stress (S') acting on the rock is equal to the total stress less its pore pressure (P_p) (Terzaghi, 1943).

Rocks find relief from tensional stress by opening perpendicular to the stress, forming a mechanical discontinuity when they fail. Such opening failure is referred to as a Mode I fracture. The formation of macroscopic Mode I fractures usually requires a free surface and at least one of the three stress magnitudes to be practically equal to zero. Such conditions are difficult to obtain in confining subsurface environments except in specific circumstances. With confinement, one would expect the rock to fail macroscopically in shear before failing in Mode I. However, high tensile stresses can be generated in compressional settings on a microscopic scale at grain contacts known as "stress risers" and Mode I microfractures can develop (Engelder et al., 1981).

Under compression, when the effective stress acting on the rock matrix exceeds the compressional strength of the intact matrix, the relief response of the rock is to fail. The failure style is a sliding motion to form a shear fracture or compacting to occupy a smaller volume, or both. If the shear sliding is parallel to the fracture surface and perpendicular to the fracture

front, the failure is referred to as Mode II. If, rather, the sliding motion is parallel to the fracture surface and to the fracture front (in a scissor-like tearing), then the failure is referred to as Mode III. With respect to the horizontal, the manner in which the rocks break and slide depends on the stressing conditions, that is, the relative magnitudes of S_V, S_H, S_h and the strength of the rock. If the rock contains a preexisting mechanical discontinuity, then the manner of stress relief depends upon the discontinuity surface's coefficient of sliding friction, the stressing conditions and the orientation of the discontinuity with respect to S_H.

Values of the coefficient of sliding friction are equivalent to the tangent of the angle of repose. For natural materials at the surface, values ranges from 0.25 to 1 ("earth-on-earth", dry sand, clay, and mixed earth) while dry masonry and brickwork have values on the order of 0.6 to 0.7 (Kent, 1899). Byerlee (1978) compiled measurements of the coefficient of sliding friction relating the normal stress to the shear stress at failure for an assortment of rocks under different stress conditions and was able to fit the data with two straight lines. When the normal stress is less than 29000 psi (200 MPa), the shear stress at failure is equal to 0.85 of the normal stress. For normal stresses above 29000 psi (200 MPa) the shear stress at failure is equal to 0.6 of the normal stress plus 7250 psi (50 MPa). For general applications, Zoback (2007) suggests a coefficient of sliding friction of ~0.6.

Viewing the stress-strength interaction from a strength point of view; the strength of the intact rock (Moos, 2007) or the sliding friction and orientation (with respect to S_H) of a pre-existing mechanical discontinuity can control the magnitudes of the stresses (Moos and Zoback, 1990; Zoback, 2007). That is, when the magnitude of divergence between stresses acting on intact rock or a pre-existing mechanical discontinuity reaches the point of failure, divergence can no longer increase. This limits the magnitudes of the diverging stresses and

equilibrium between strength and stress is established. If the divergence begins to increase, the rock simply moves, maintaining the equilibrium. In either case, the strength of intact rock or the discontinuity is a very useful attribute to know.

When pressure pushes fluid through the rocks via pores and connecting pore throats, the ease by which the fluid flows (permeability) is indexed in units of darcy (d), millidarcies (md), microdarcies (μd), and nanodarcies (ηd) such that 1 d = 1000 md = 1 x 10^6 μd = 1 x 10^9 ηd. The greater the permeability, the easier it is for fluid to flow at the same pressure gradient, translating to a higher flow rate. For the following discussion, I will only deal with rock whose matrix permeability is less than 1 μd (0.001 md). Since the discussion here is limited to rocks with permeability in the range of a microdarcy or less, it is important to note that microcracks contribute greatly to what slight permeability exists (Ostensen, 1983).

Characterization of Rock Strength:

The strength of intact rock can be rated as the stress at which failure occurs when two of the three stresses, along with the pore pressure, are zero (i.e. no confinement). In practice, this condition is called the Unconfined Compressive Strength (UCS), and here it is indexed in pounds per square inch (psi). We can relate the rate at which the rock gains strength with confinement to the Internal Friction Angle (IFA) of the rock. The larger the IFA, the faster the rock strength increases with confinement. UCS and IFA can be determined from laboratory tests or estimated from well logs. Weingarten and Perkins (1995) presented useful correlations of IFA and cohesion (Co) using acoustic slowness (μsec/ft) and bulk density (Rho_b, g/cm^3). The correlations have been recast into a graphical expression (Figure 1) of UCS by

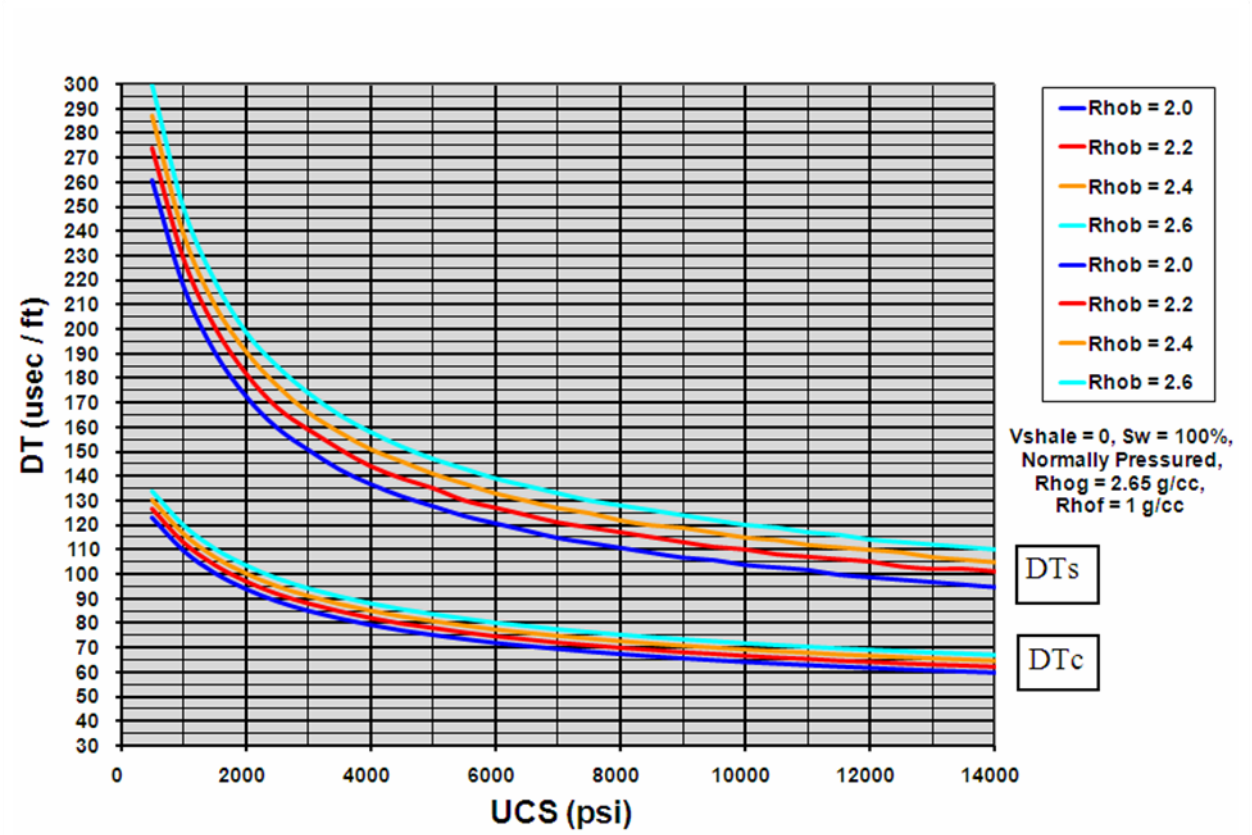

Figure 1. Correlation between bulk density (Rho_b), compressional slowness (DTc), and shear slowness (DTs) with unconfined compressional strength (UCS in psi) of clean sandstones, with matrix density of 2.65 g/cm^3, fully saturated with brine at normal pressure conditions. The formulation presented was developed from the equations presented by Weingarten and Perking (1995) and subsequently modified for ease of use.

$$UCS = 2\,Co\,\frac{(\text{Sin IFA})}{[(\text{Tan IFA})(1 - \text{Sin IFA})]}. \qquad \text{(Eq. 1)}$$

To visualize the dependence of UCS on IFA, two times the trigonometric function in Equation 1 is displayed in Appendix 2 as "Cohesion to UCS Multiplier from Internal Friction Angle."

In the laboratory, a convenient way to express the strength of rocks is to plot the axial stress at failure on the ordinate, and confinement on the abscissa from two or more companion samples subjected to triaxial compression test (Figure 2). A trend of increasing axial stress at failure with increase in confinement is the normal response (Van der Pluijm and Marshak, 2004). As a reference regarding the span of UCS values, Table 2 presents a list of a few known rock formations and associated UCS values.

Techniques such as indentation tests using a penetrometer with any one of assorted point sizes and shapes, rebound "hammers" of various sizes with a wide range of impact forces, and sonic devices with varying configurations are employed to determine rock strength. One particularly useful point-stress penetrometer is a handheld micro-conical point indenter referred to as the *Dimpler* (Figure 3). Its name refers to the small conical depression it creates (Ramos et al., 2008). The shape and depth of the indentation are recorded by means of a dyed conical tip that is impressed onto a compliant, removable tape affixed to the surface of interest. In the case of core, the surface is first covered with compliant tape that is about a square inch in size. The conical tip of the indenter is coated with a red dye and then forced, at a constant axial stress, through the tape and into the sample creating a conical red depression (dimple) on the tape. The combination of red dye and tape preserves a record of the dimple geometrical attributes. The geometrical attributes (e.g. diameter and depth) depend on the rock UCS and IFA (Ramos et al., 2008). The tape is then removed from the sample and placed on a flat

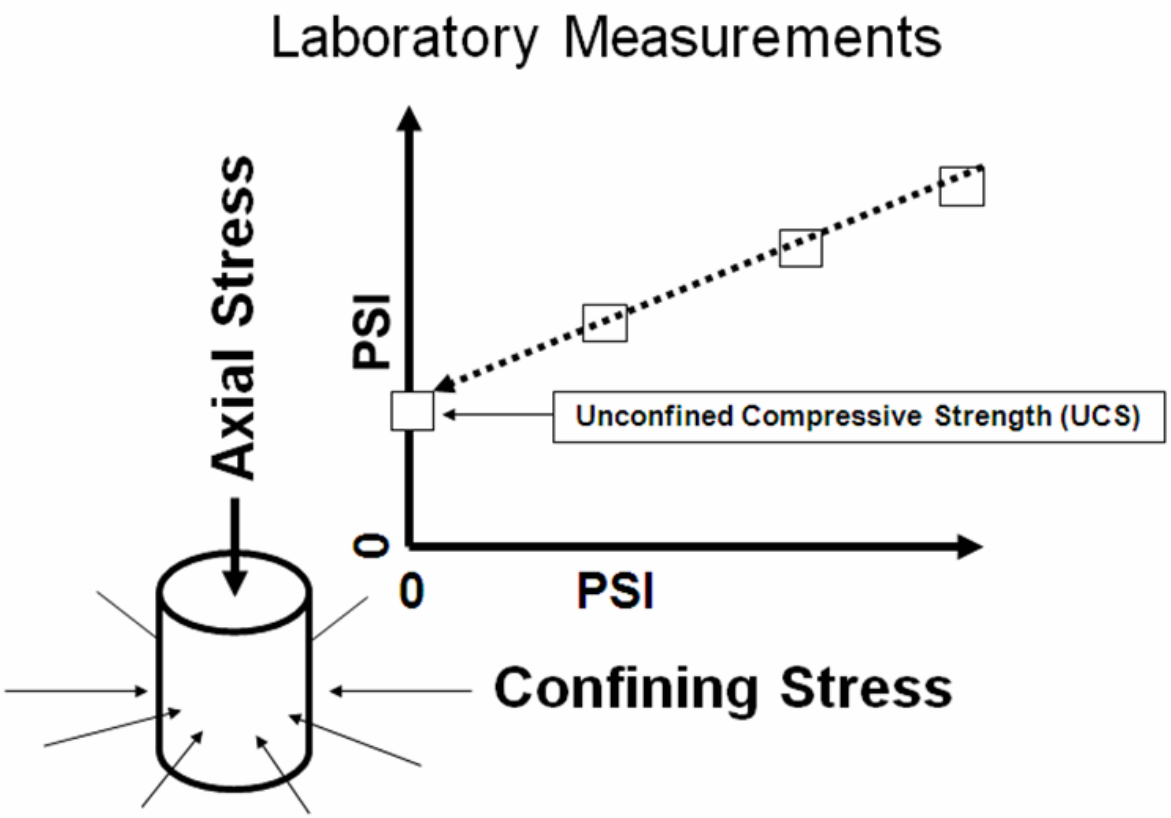

Figure 2. Triaxial compression test geometry and a plot of axial stress at failure for a given confinement from three separate triaxial tests of companion samples. Best fit line is projected through the data points and extrapolated to the ordinate (zero confinement). The value at zero confinement is referred to as the Unconfined Compressive Strength (UCS). The slope of the best-fit extrapolated line (m_{bfexl}) is related to the rock's Internal Friction Angle (IFA) by

$$IFA = \text{ArcSin}\frac{[\text{Tan}(\text{Tan}\,(m_{bfexl})) - 1]}{[\,\text{Tan}(\text{Tan}\,(m_{bfexl})) + 1]}.$$

Table 2: Collection of selected UCS values.

Rock	UCS, psi, (~MPa)	Source
Nevada Test Site tuff	1639 (11.3)	Goodman, 1989
Cement (oilfield)	~100 (.68) to 6500 (44.8)	Halliburton, 1978
Flaming Gorge shale	5100 (35.2)	Goodman, 1989
Bedford limestone	7400 (51)	Goodman, 1989
Berea sandstone	10700 (73.9)	Goodman, 1989
Micaceous shale	10900 (75.2)	Goodman, 1989
Barnett shale	~8000 (55.2) to 11000 (75.8)	Enderlin, 2009, unpublished
Lockport dolomite	13100 (90.3)	Goodman, 1989
James Lime (TX)	~7000 (48.3) to 15000 (103.4)	Enderlin, 2009, unpublished
Nevada Test Site granite	20500 (141.4)	Goodman, 1989
Navajo sandstone	31030 (214)	Goodman, 1989
Solenhofen limestone	35500 (244.8)	Goodman, 1989

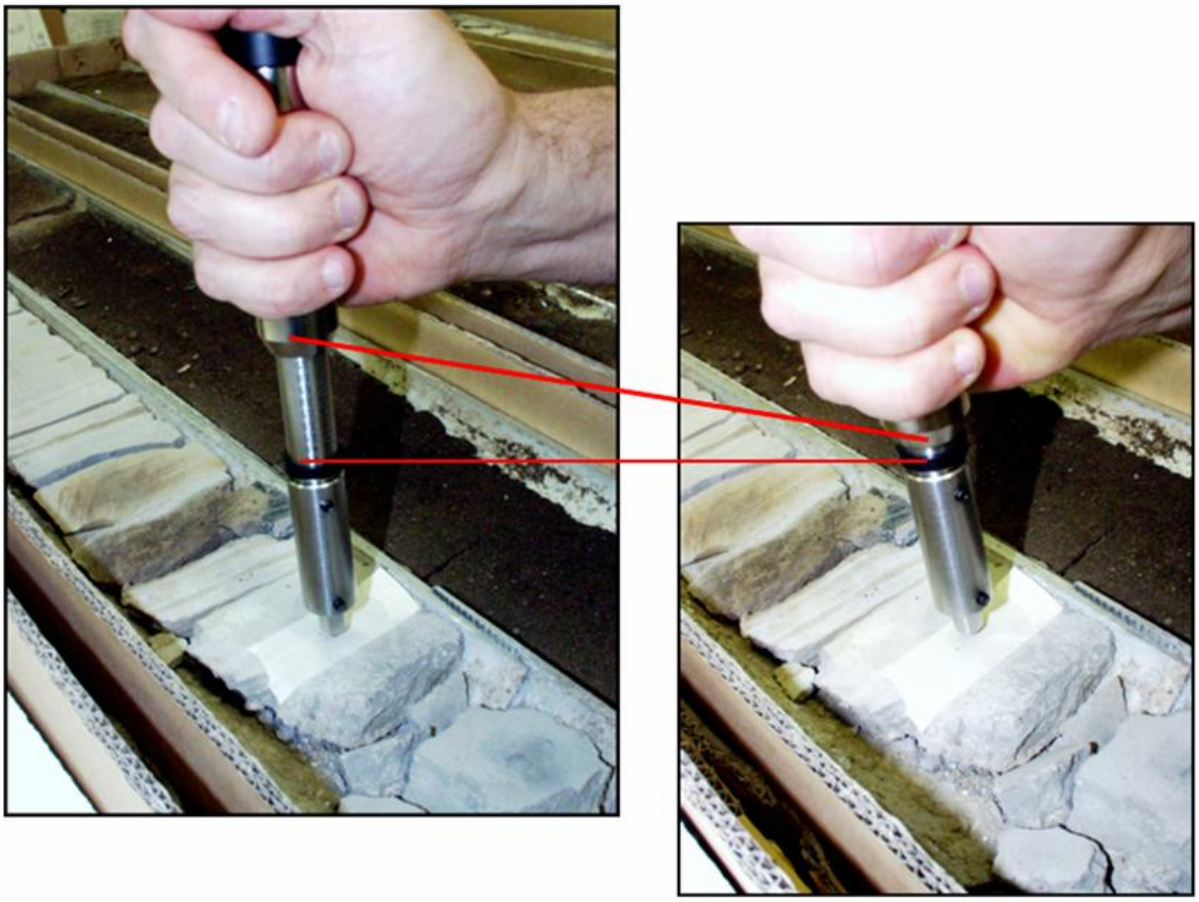

Figure 3. Dimpler point penetrometer test.

medium for archiving. The diameter of a dimple is measured with a graduated surface magnifying glass. Correlation between dimple diameter and UCS from triaxial testing has been established and is presented graphically in Figure 4 (Enderlin, 1998, unpublished).

Characterization of Stress Magnitude and Direction:

Overburden (S_V):

In the approach presented, S_V is the reference for S_H and S_h. Therefore, S_V needs to be carefully determined. In most cases, S_V is the stress exerted by the overburden above the point of interest in the subsurface, and can be expressed as a function of the densities of earth materials measured vertically from the surface to the point of interest. One approach is to sum the log bulk density (Rho_b, g/cm^3) readings one depth increment at a time, between the surface and the point of interest, then divide by the total number of depth increments used, obtaining an average density value ($avRho_b$) of the overburden. Multiplying the $avRho_b$ by 0.4335 $psig/ftcm^3$ (14.7 psi stands 33.91 vertical feet of 1 g/cm^3 water) and the True Vertical Depth (TVD, in feet) will yield an approximation of S_V in psi. Care needs to be taken to ascertain that the TVD log derived for the Measured Depth log (MD) is, in fact, equivalent in thickness and density to the section directly above the point of interest. Another caveat is the nature of the bulk density readings regarding the relationship between the "true density" and "calibrated electron density" (apparent log density) as a function of the quotient of the atomic number (Z) and atomic weight (A) (Schlumberger, 1972), where

$$\text{Apparent Log Density} = 1.0704 \times \left[\text{True Density} \times 2\left(\frac{Z}{A}\right)\right] - 0.1885 \qquad \text{(Eq. 2)}$$

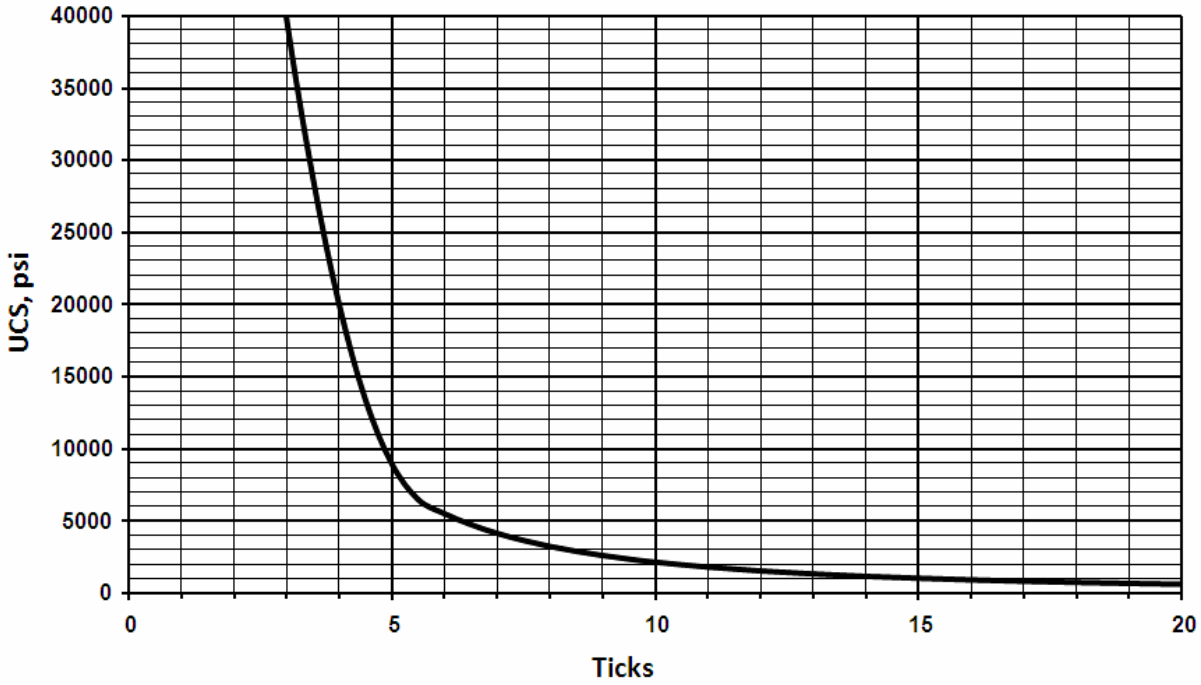

Figure 4. Correlation between the diameter of a dimple, measured in "ticks," (each tick is equal to 0.005 of an inch) and the UCS of the sample in psi (Enderlin, 1998, unpublished).

At first, a one hundredth of a g/cm^3 appears insignificant, but when added up over thousands of feet, the swing in magnitude of S_V could be many hundreds of psi. When bulk density to the surface is not available, some estimation is required. A value of 2.3 g/cm^3 (~19 ppg) works as an initial estimate for most clastic sedimentary rock columns and corresponds to a water-filled average porosity of about 15% (Zoback, 2007). The effect of water density cannot be neglected, and, if possible, the elevation of the water table should be noted and factored into bulk density estimates.

Horizontal stresses (S_H and S_h):

The relationship between S_V, S_H, and S_h can be visualized in the form of an orthogonal plot, with the magnitude of S_h on the abscissa and the magnitude S_H on the ordinate both with the same units (Figure 5). The equality line (a positive slope at 45° passing through the origin) carries the same magnitude of stress in both S_H and S_h. The portion of the plot below that equality line is, by definition, not possible since S_h cannot be larger than S_H and, therefore, is not used. The magnitude of S_V is posted on the equality line in the form of a dot. Two lines will originate at the S_V dot, with one extending upward, parallel to the ordinate, and the other to the left, parallel to the abscissa and terminating at the ordinate. These two lines divide the useable portion of the plot into three stress domains, two triangular and one rectangular (Figure 5). The lower left triangle represents the situation where S_V is greater than S_H and S_h ($S_V > S_H > S_h$) and would correspond to a normal fault (NF) in Anderson's classification scheme (Anderson, 1951; Moos and Zoback, 1990), implying that $S_1 = S_V$, $S_2 = S_H$, and $S_3 = S_h$. The upper right triangle represents the situation where S_H and S_h are both larger than S_V ($S_H > S_h > S_V$) and corresponds to reverse fault (RF) in Anderson's classification with $S_1 = S_H$, $S_2 =$

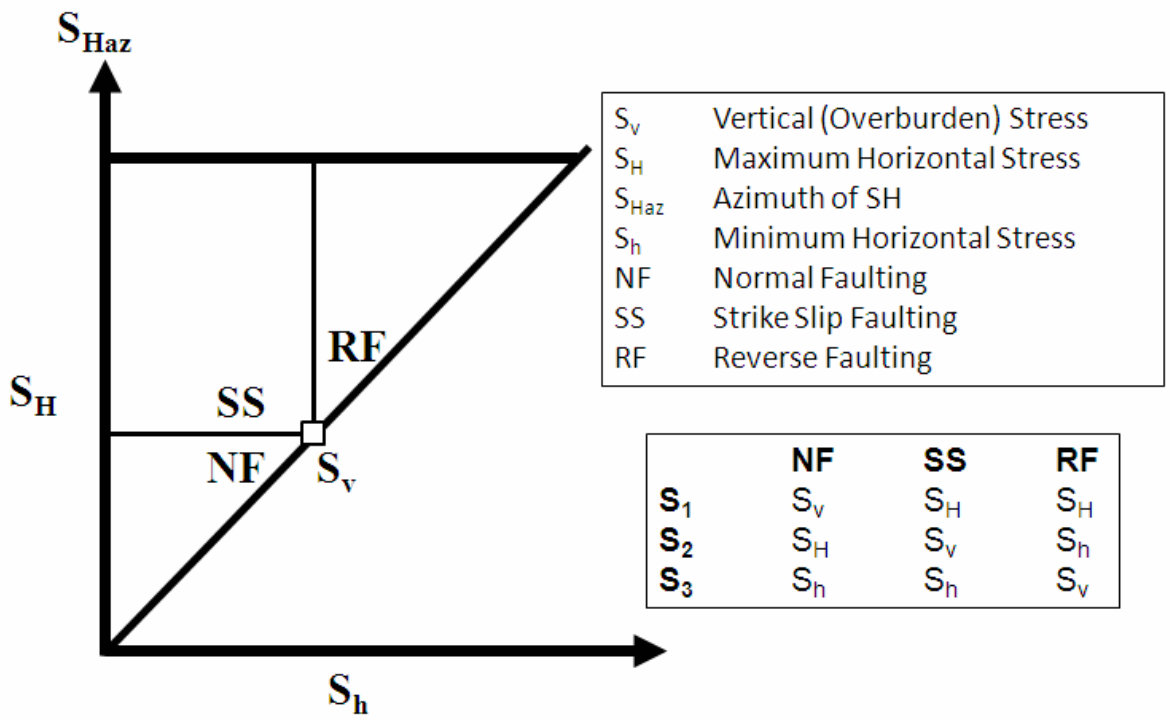

Figure 5. Plot of S_H versus S_h with the equality line and fault boundaries displayed. The location of S_V on the equality line is the singularity of normal fault, strike-slip and reverse fault stress domains as defined by Anderson (1951). Also presented are the appropriate association with S_1, S_2, and S_3.

S_h, and $S_3 = S_V$. The rectangle represents the situation where S_H is larger than S_V and S_V is larger than S_h ($S_H > S_V > S_h$), and corresponds to a strike-slip fault (SS) in Anderson's scheme, where $S_1 = S_H$, $S_2 = S_V$, and $S_3 = S_h$ (Figure 5).

Constraining the magnitudes of present-day horizontal stresses (S_H and S_h):

The magnitude of the divergence between stresses can be controlled by the sliding friction on favorably oriented mechanical discontinuities. The magnitudes of S_H and S_h can be constrained if S_V is constant and the coefficient of sliding friction (μ) and pore pressure (P_p) are known. Moos and Zoback (1990) published the following equations relating S_V, S_H, S_h, and P_p with μ for three faulting styles:

$$\text{Normal faulting: } \frac{S_1}{S_3} = \frac{(S_v - P_p)}{(S_h - P_p)} = \left\{\left[(\mu^2+1)^{0.5}\right]+\mu\right\}^2, \qquad \text{(Eq. 3)}$$

which considers the dip section through a normal fault mechanical discontinuity;

$$\text{Reverse faulting: } \frac{S_1}{S_3} = \frac{(S_H - P_p)}{(S_v - P_p)} = \left\{\left[(\mu^2+1)^{0.5}\right]+\mu\right\}^2, \qquad \text{(Eq. 4)}$$

which considers the dip section through a reverse fault mechanical discontinuity, or;

$$\text{Strike-slip faulting: } \frac{S_1}{S_3} = \frac{(S_H - P_p)}{(S_h - P_p)} = \left\{\left[(\mu^2+1)^{0.5}\right]+\mu\right\}^2, \qquad \text{(Eq. 5)}$$

which considers a strike-slip movement along a mechanical discontinuity. Taken together, the three equations describe a Stress Polygon (Figure 6).

The size of the Stress Polygon and, therefore, the number of potential S_H-S_h pairs adjusts with changes in pore pressure (P_p). Decreasing P_p increases the size of the Stress Polygon, allowing for more potential S_H-S_h pairs. Increasing P_p decreases the polygon size, thereby reducing the potential S_H-S_h pairs. At very high P_p, the polygon size approaches a

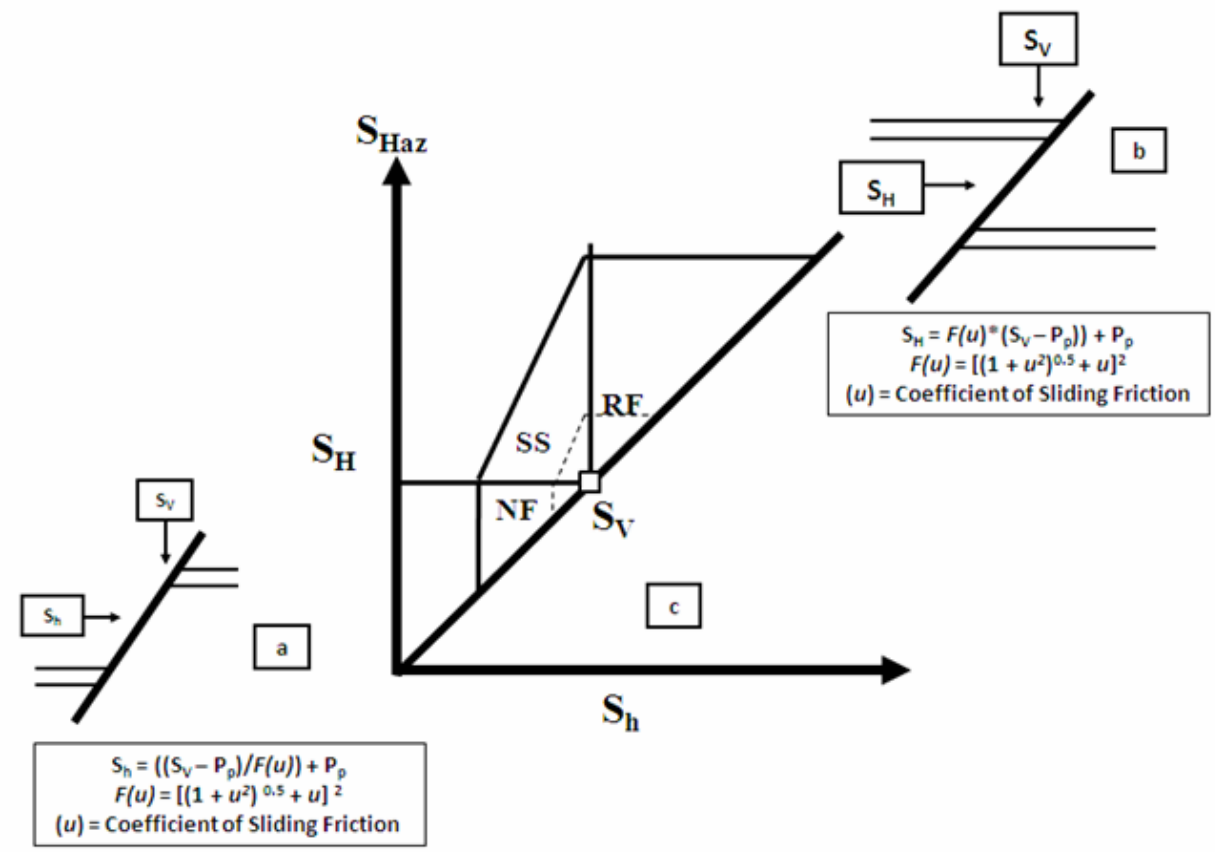

Figure 6. a. Dip section through a normal fault mechanical discontinuity. Equation 3 has been solved for the smallest value of S_h. b. Dip section through a reverse fault mechanical discontinuity. Equation 4 has been solved for the largest value of S_H. c. Equation 5 establishes combinations of S_H and S_h for strike slip fault domain and thereby completing the Stress Polygon for a given μ and P_p. At very high values of P_p, the Stress Polygon shrinks in size as represented by the dashed lines.

singularity (S_V), where normal faults, strike-slip faults, and reverse faults can exist simultaneously (Figure 6).

Setting the magnitudes of S_h via classical methods:

Based on Poisson's ratio (v), S_V, and Pp, Eaton (1969) suggested a technique for the determination of S_h, where

$$S_h = \left[\frac{v}{(1-v)}\right](S_v - P_p) + P_p. \quad \text{(Eq. 6)}$$

This technique has been elaborated by Gretner (1981) and Cumella and Scheevel (2008), who include the concept of strain and Young's modulus in the formulation.

Another method for determining the value of S_h is to produce a Mode I tensile fracture originating at the borehole wall by increasing the pressure within the borehole until the rock fails. In this case, the borehole wall acts as the free surface and a Mode I fracture forms. Analysis and interpretation of the pressure to initiate, propagate, and, once the pumping stops, the closing of the fracture ("closure pressure") can be used to evaluate the magnitude of S_h. All these analyses assume that a Mode I fracture was induced and no reactivation of pre existing mechanical discontinuities took place. The processes for inducing an assumed Mode I fracture go by many names including Leak Off Test (LOT, performed between setting casing and continued drilling), mini-fracture test, and fracture stimulation (Zoback, 2007). Unfortunately, in most cases, the values of LOT and "closure pressure" are reported, but information about the method of analysis or insights into the quality of the data are rarely available.

Setting the magnitudes of S_H and S_h utilizing stress related borehole failures and the Stress Polygon:

A borehole can be viewed as a stress magnifier. The stresses supported by rock before being removed by the bit are relocated and concentrated at the borehole wall. The concentrated stresses around the borehole are referred to as "hoop" stresses. For a vertical, cylindrical borehole, the magnitude of concentrated stress has been described by the Kirsch equations (Kirsch, 1898; Jaeger and Cook, 1979). A simplified expression for the largest magnitude of effective hoop (MaxHoop) stress concentration at the borehole wall is:

$$\text{effective MaxHoop stress} = 3S_H - S_h - 2P_p - (P_m - P_p) \quad \text{(Eq. 7)}$$

where P_m equals the stress exerted by the fluids in the borehole. For the smallest magnitude of effective hoop (MinHoop), stress concentration at the borehole wall is:

$$\text{effective MinHoop stress} = 3S_h - S_H - 2P_p - (P_m - P_p) \quad \text{(Eq. 8)}$$

If P_p and P_m are held constant then the above relationships reduce to

$$\text{effective MaxHoop stress} = 3S_H - S_h - \text{Constant} \quad \text{(Eq. 9)}$$

and

$$\text{effective MinHoop stress} = 3S_h - S_H - \text{Constant} \quad \text{(Eq. 10)}$$

This implies that for every S_H-S_h pair on the Stress Polygon, the value of effective MaxHoop stress can be determined and contours of equal stress can be plotted on the Stress Polygon (Figure 7). Where the effective MaxHoop stress exceeds the strength of the rock along the borehole wall, the rock fails in shear and pieces of rock (cavings) fall into the borehole, thereby enlarging the borehole size and leaving behind "breakouts". Such borehole enlargements are observable via open-hole logs, such as calipers, as a borehole diameter becomes larger than bit size (Plumb and Hickman, 1985) and, depending on the vertical scale, as dark spots or stripes

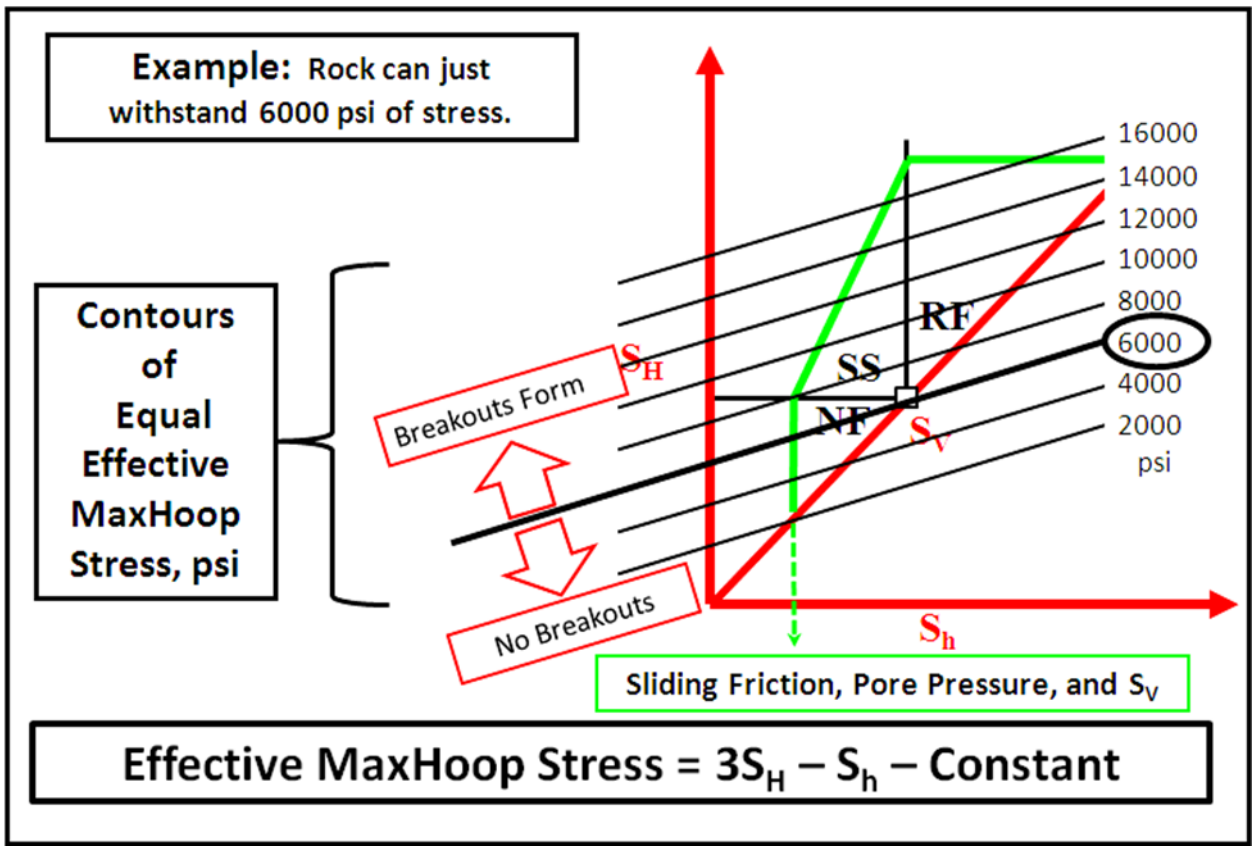

Figure 7. Contours of equal effective MaxHoop stress (in psi) as mapped on the Stress Polygon. Potential $S_H - S_h$ combinations are restricted by the presence or absence of breakouts for a rock that can just withstand 6000 psi (41.3 MPa) of stress before failing.

on borehole image logs. For example, if a rock can withstand 6000 psi of stress before failure, then observation of the presence or absence of breakouts partitions the possible S_H-S_h pairs that can exist at the 6000 psi contour line (Figure 7). If no breakouts are observed, then present-day stress state is below the 6000 psi contour line. On the other hand, the existence of breakouts indicates that the present-day stress state is above the 6000 psi contour line.

In the same manner, for every S_H-S_h pair on the Stress Polygon, the value of effective MinHoop stress can be determined and contours of equal stress can be constructed. If the effective MinHoop stress exceeds the tensile strength of the rock, a Mode I tensile fracture may develop. Since the span of tensile strength of rocks is much smaller than compressional strength, only the 0 stress contour is plotted on the Stress Polygon (Figure 8). Just as with breakouts, the presence or absence of tensile cracks partitions the possible S_H-S_h pairs that exist at the 0 psi contour line. Although the presence or absence of tensile cracks is best determined by analysis of borehole image logs, inferences can be made from analysis of drilling data such as "flow in – flow out". If tensile cracks are not observed, then present-day stress state is to the right of the 0 psi contour line. On the other hand, the existence of induced tensile fractures suggests that present-day stress state is to the left of the 0 psi contour line (Figure 8). Combining the effective MaxHoop stress with the effective MinHoop stress on the same Stress Polygon is the primary tool for setting the magnitudes of S_H and S_h (Figure 8).

Determining the direction of S_H (S_{Haz}):

One approach for resolving the direction of S_H (S_{Haz}) is to consider the Stress Polygon in map view. In such a view, we assume S_V to be vertical and the S_H axis (ordinate) to be a reference direction (Figure 9). Further, consider the boundaries of the Stress Polygon, less the

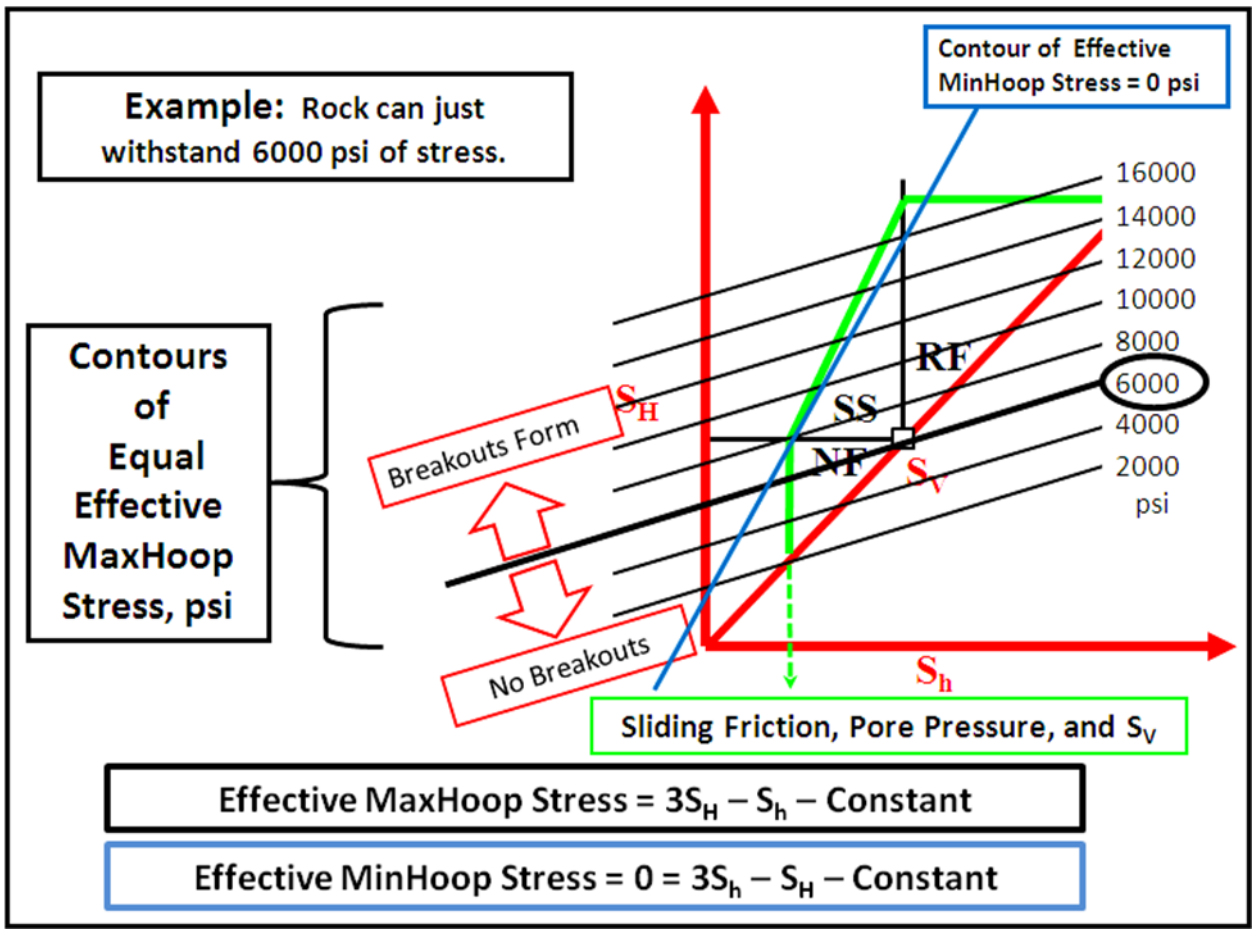

Figure 8. Contour of zero effective MinHoop stress (in blue) as mapped on the Stress Polygon. Potential S_H–S_h combinations are restricted by the presence or absence of tensile cracks. The mapped relationship of breakouts and tensile cracks on the Stress Polygon becomes the primary tool for settings the contemporary magnitudes of S_H and S_h.

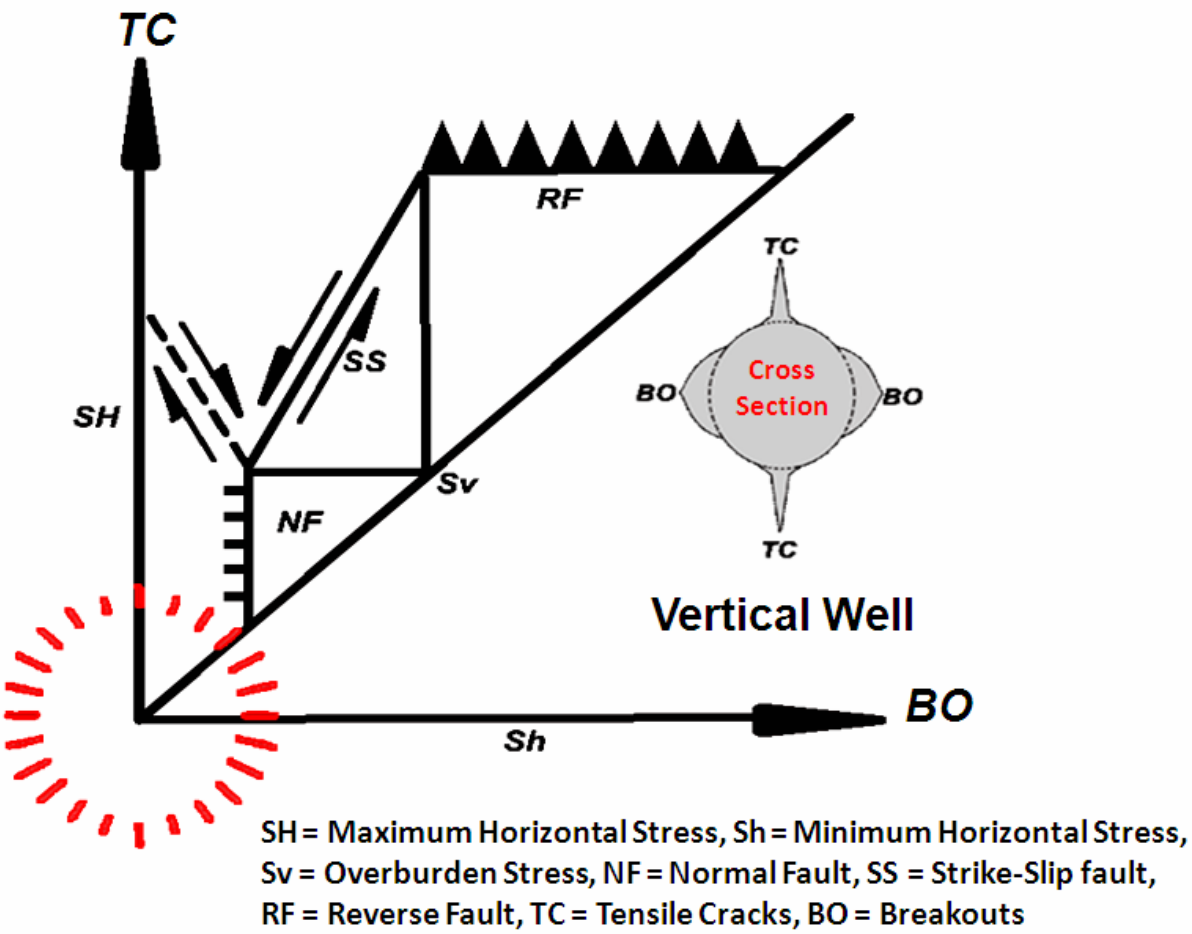

Figure 9. Stress Polygon printed on clear plastic (referred to as the *Clear Plastic Stress Polygon*), used in conjunction with a fault map and borehole failures (breakouts and tensile cracks) for the determination of S_{Haz}.

equality line, as the strike for the associated fault (normal fault = NF, strike-slip fault = SS, and reverse fault = RF). Printing the Stress Polygon on a clear plastic sheet (referred to as a *Clear Plastic Stress Polygon*) facilitates use with existing structure maps. Placing the Clear Plastic Stress Polygon over a structure map of nearby active faults, so that the appropriate polygon strike boundary is aligned parallel to the strike of the mapped faults, results in the S_H axis pointing in the direction (map coordinates) of S_H. S_{Haz} can be read directly with respect to geographic north via the red angular index (Figure 9).

Another method for determining S_{Haz} is to observe the heading of tensile cracks (TC) and/or breakouts (BO) on an image log. If tensile cracks and breakouts are observed, then S_{Haz} is in the direction of tensile cracks and S_h in the direction of breakouts. The same orientation relationship is noted on the cross section insert of Figure 9 and at the arrow end of both stress axes.

To illustrate the quantitative aspects of the stress polygon two examples will be used. The example 1 is a continuation of Figures 7 and 8 (unstated pore pressure, coefficient of sliding friction (μ), S_{Haz} and stress units) but includes a cartoon of borehole images. Example 2 extends the concepts with realistic values for all variables.

Example 1

For a vertical well, if breakouts and tensile cracks are found in a rock able to withstand 6000 psi, then present-day magnitudes of S_H and S_h can be constrained (Figure 10). In this case, the S_H-S_h pair is above the 6000 psi (41.3 MPa) MaxHoop stress contour line and to the left of the 0 psi MinHoop stress contour line and resides within the borders of the Stress

Polygon as determined from sliding friction, pore pressure and S_V. Experience indicates that choosing the lower magnitudes for S_H and S_h that accommodate the observation is a reasonable

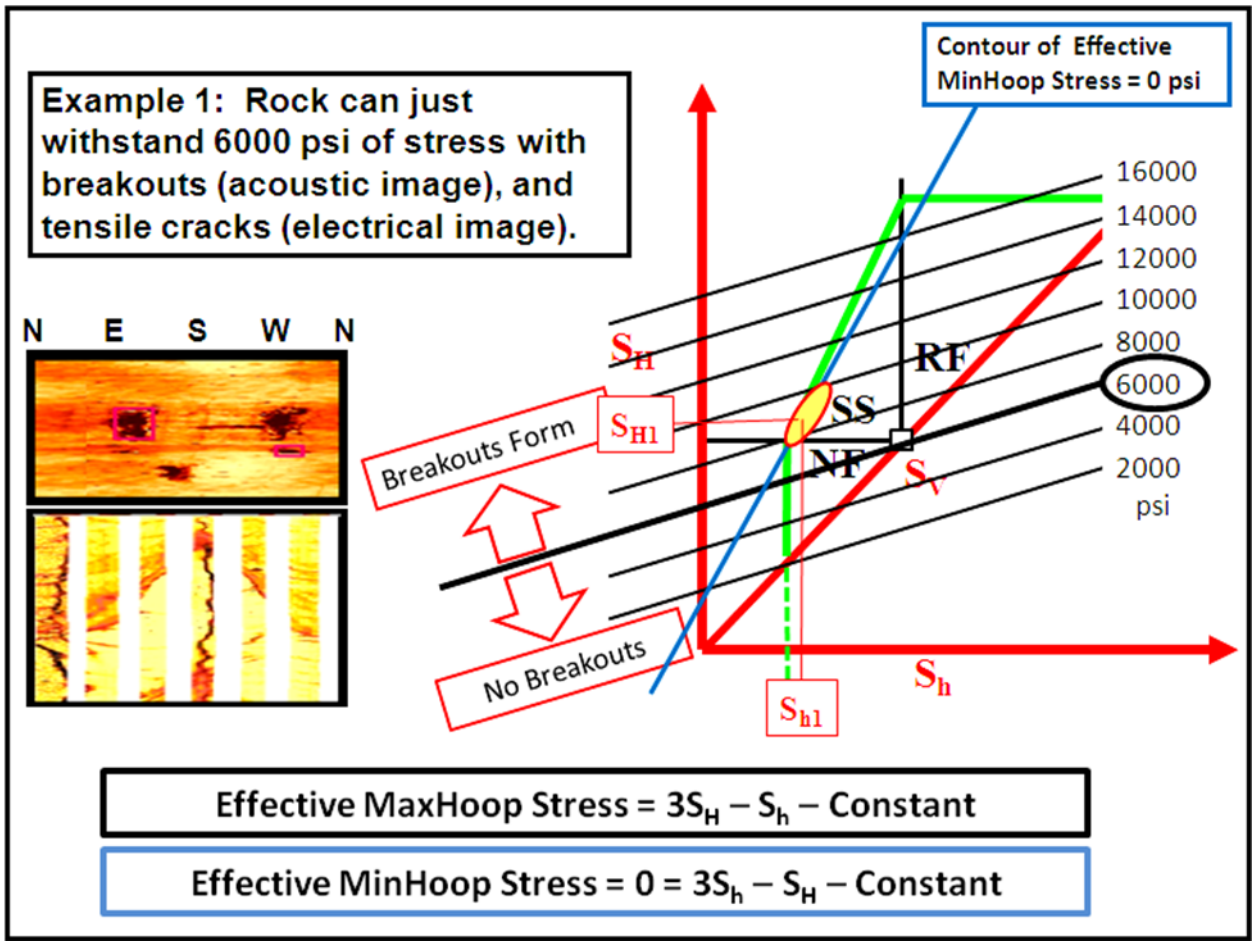

Figure 10. Determining S_H and S_h magnitudes (yellow ellipse) by observing (1) that a rock capable of just withstanding 6000 psi (41.3 MPa) of stress before failing forming breakouts and (2) tensile cracks have formed. The breakouts are recognized and orientation observed (with respect to N, E, S, and W) in the uppermost of the two borehole image inserts on the left (the two dark spots). The lower borehole image shows tensile fractures as dark irregular vertical streaks. S_{H1} and S_{h1} are the selected values of stress.

first estimation of the stress state (yellow spot in the strike-slip domain on Figure 10). The estimated values of S_{H1} and S_{h1} may be thus selected. Since the breakouts in Figure 10 are east-southeast to west-northwest trending and tensile cracks are trending north-northeast to south-southwest, S_{Haz} is oriented north-northeast to south-southwest. Hence, the characterization of present-day state of stress is determined and S_{Haz} is approximately 030° (N30°E). Since the stress state resides in the strike-slip stress domain, then $S_1 = S_{H1}$, $S_2 = S_V$, and $S_3 = S_{h1}$.

Example 2

For the following discussion on magnitudes of the normal stress and shear stress acting on an arbitrarily oriented planar mechanical discontinuity, all appropriate variables need to be assigned practical numeric values. To that end, Example 2 is offered and displayed as a Stress Polygon (Figure 11). Compared to the Stress Polygon for Example 1 (Figure 10), the 6000 UCS psi (41.3 MPa) strength contour has moved down on the Stress Polygon. This is because of the greater depth, mud weight (Pm), and pore pressure (Pp) values in this example. The values at approximately 8000 ft (2438 m) True Vertical Depth (TVD) are posted in Table 3. The orientation of the planar mechanical discontinuity can be described by its strike and dip.

Normal and Shear Stress Magnitudes Acting on an Arbitrarily Oriented Planar Mechanical Discontinuity:

Having estimated the state of present-day stress (Table 3), the magnitudes of the normal stress and shear stress acting on an arbitrarily oriented planar mechanical discontinuity can be estimated (Figure 12).

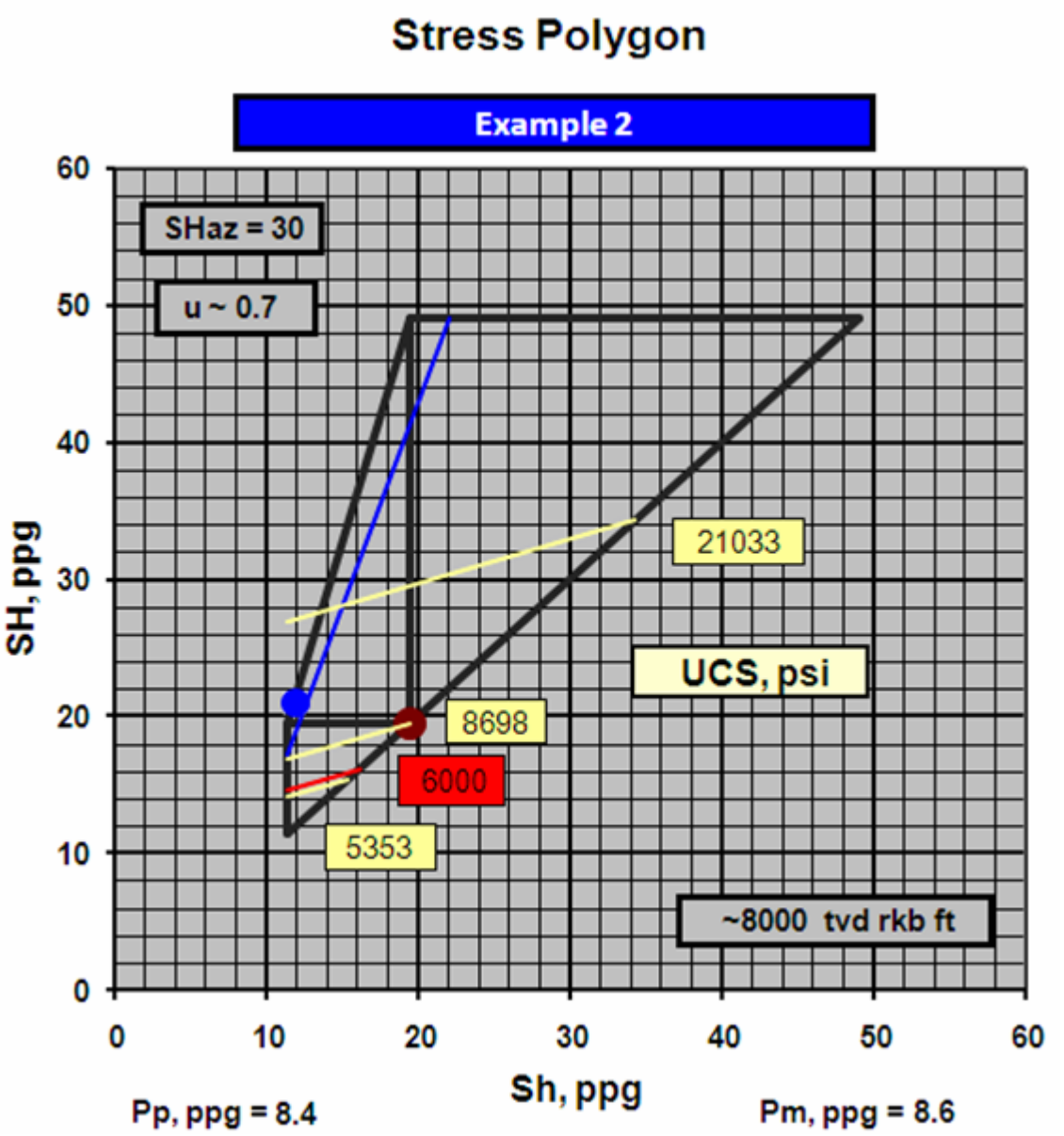

Figure 11. Stress Polygon with four rock strength contour lines and their UCS values plotted. The yellow rock strength lines are positioned, for reference only, along the equality line, one through S_V (dark red dot), one half-way between S_V and the lower left end of the equality line, and last one halfway between S_V and the upper right end of the equality line. The red line and associated value box corresponds to the estimated rock strength of interest (6000 psi: 41.3 MPa). The blue dot marks the estimated present-day state of stress.

Table 3. Example 2 information.

	~ ppg	psi	MPa
$S_H = S_1$	21	8706	60.0
$S_V = S_2$	19.4	8079	55.7
$S_h = S_3$	11.8	4933	34.0
P_m	8.6	3576	24.6
P_p	8.4	3491	24.1

Coefficient of sliding friction (u) = 0.7
Strike-slip stress domain.
Reference depth = 8000 feet TVD (2438.4 m)

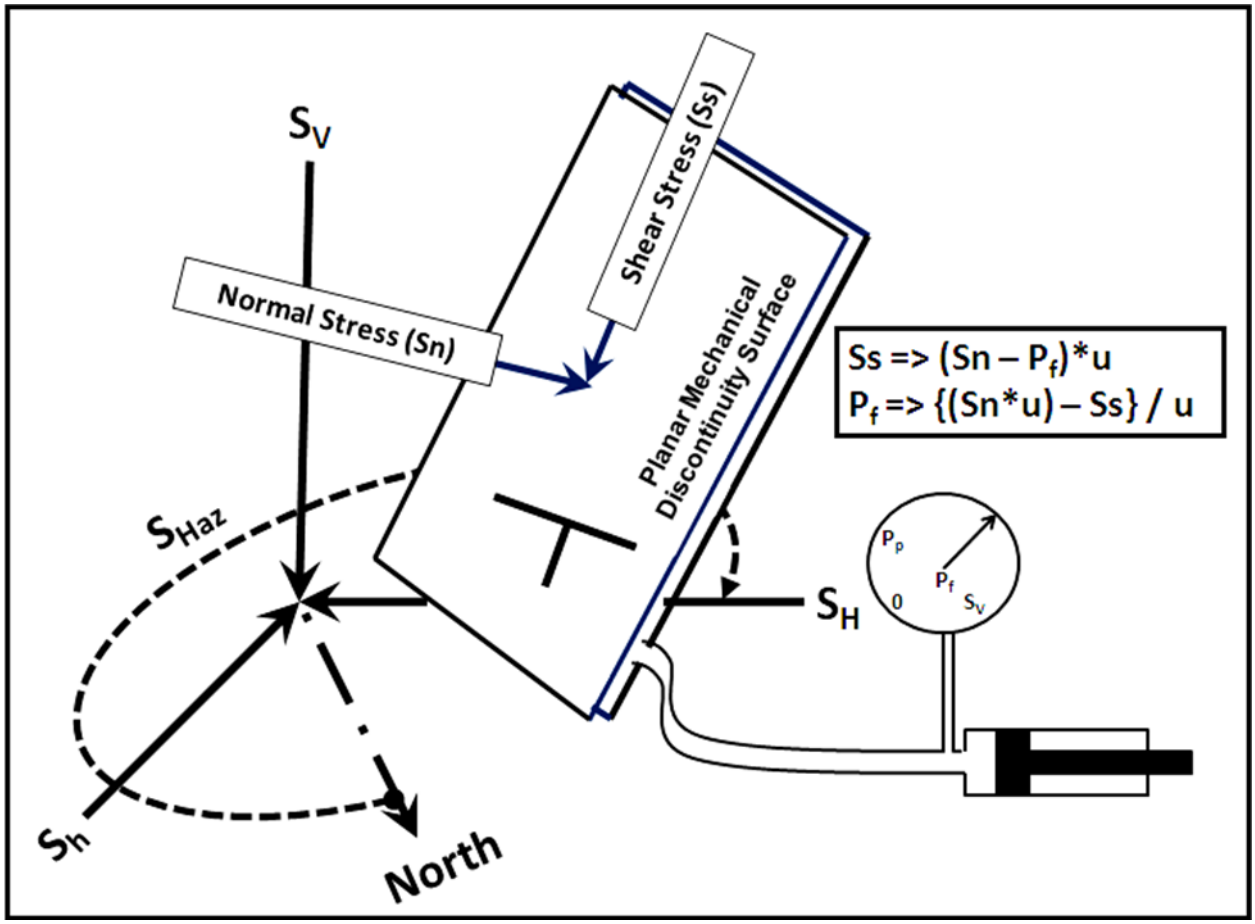

Figure 12. Arbitrary planar mechanical discontinuity surface spatially described by strike and dip is placed in a stress field described by S_V, S_H, S_h, and S_{Haz}. The normal stress (Sn) and shear stress (Ss) can be calculated. Reactivation occurs by increasing P_f such that the product of (Sn - P_f) and u is less than Ss.

Determination of normal and shear stress magnitudes:

The normal stress (Sn) and effective shear stress (Ss) can be calculated by

$$Sn = (B_{11})^2S_1 + (B_{12})^2S_2 + (B_{13})^2S_3 \quad \text{(Eq. 11)}$$

and

$$Ss = (B_{11})\,(B_{21})S_1 + (B_{22})\,(B_{12})S_2 + (B_{23})\,(B_{12})S_3 \quad \text{(Eq. 12)}$$

(Jaeger and Cook, 1979). The (B_{ij}) terms are the directional cosines between the surface of the mechanical discontinuity and the stress field. Table 4 displays the Sn and Ss for selected dip and strike combinations for the conditions posted in Table 3.

Effect of normal stress on fluid flow along a planar mechanical discontinuity:

The subject of fluid flow through fractures has been extensively discussed in the literature (e.g., Tolman, 1937; Levorsen, 1967; Aguilera, 1980; Gidley et al., 1989). Of note is the compilation by the Committee on Fracture Characterization and Fluid Flow, National Research Council (1996). Flow rate (Q) through a fracture as the flow between two parallel plates has been modeled, where

$$Q = \frac{[(W^3)(DP)]}{(12\ n)}. \quad \text{(Eq. 13)}$$

In this case, the flow rate (Q) is a function of the cube of the plate separation (W, also known as aperture and fracture width), for a given viscosity (n) and pressure gradient (DP). Zoback (2007) pointed out that the largest separation distance (Amax) between the sides of a elliptical cross-section fracture at its midpoint is a function of the fluid pressure in the fracture (Pf), the length of the fracture (L), Poisson's ratio (v) and Static Young's modulus (E) of the host rock, and S_3 such that

DIP	Sn	Ss	Sn	Ss	Sn	Ss	Sn	Ss	Sn	Ss	Sn	Ss	Sn	Ss	DIP
85	5893	5130	5208	4464	4957	3764	5208	4464	5893	5130	6829	5374	7766	5119	85
75	6024	5163	5380	4654	5144	4277	5380	4654	6024	5163	6904	5340	7784	5071	75
65	6270	5195	5703	4891	5495	4696	5703	4891	6270	5195	7045	5268	7820	4977	65
55	6601	5183	6138	5055	5968	4969	6138	5055	6601	5183	7234	5146	7867	4838	55
45	6978	5087	6632	5084	6506	5064	6632	5084	6978	5087	7449	4966	7921	4657	45
35	7354	4887	7127	4954	7044	4969	7127	4954	7354	4887	7665	4724	7975	4440	35
25	7686	4581	7562	4669	7517	4696	7562	4669	7686	4581	7854	4423	8023	4192	25
DIP	Sn	Ss	Sn	Ss	Sn	Ss	Sn	Ss	Sn	Ss	Sn	Ss	Sn	Ss	DIP
Strike	0		15		30		45		60		75		90		Strike

DIP	Sn	Ss	Sn	Ss	Sn	Ss	Sn	Ss	Sn	Ss	Sn	Ss	Sn	Ss	DIP
85	7766	5119	8451	4431	8702	3545	8451	4431	7766	5119	6829	5374	5893	5130	85
75	7784	5071	8429	4407	8665	3648	8429	4407	7784	5071	6904	5340	6024	5163	75
65	7820	4977	8387	4358	8595	3731	8387	4358	7820	4977	7045	5268	6270	5195	65
55	7867	4838	8331	4284	8500	3786	8331	4284	7867	4838	7234	5146	6601	5183	55
45	7921	4657	8266	4184	8393	3805	8266	4184	7921	4657	7449	4966	6978	5087	45
35	7975	4440	8202	4060	8286	3786	8202	4060	7975	4440	7665	4724	7354	4887	35
25	8023	4192	8146	3915	8191	3731	8146	3915	8023	4192	7854	4423	7686	4581	25
DIP	Sn	Ss	Sn	Ss	Sn	Ss	Sn	Ss	Sn	Ss	Sn	Ss	Sn	Ss	DIP
Strike	90		105		120		135		150		165		180		Strike

Table 4. Normal and shear stresses (psi) acting on planes defined by dip and strike for conditions outlined in Table 3. This table of strike direction (columns) and dip magnitude (rows) is a discretization (with 15° bin for strike and 10° bin for dip, excluding dip magnitudes below 25° and above 85°) of the continuum of strike and dip combinations of planar mechanical discontinuities surfaces. The value within each cell is the normal effective stress (Sn) and effective shear stress (Ss) calculated using the strike and dip values stated on the respective axis.

$$Amax = \frac{[2(P_f - S_3)\, L\, (1 - v^2)]}{E}. \qquad \text{(Eq. 14)}$$

This indicates the dependence of aperture on the magnitude of S_3, which controls flow rate (Q) as described by

$$Q = \left(\frac{\pi}{8n}\right)\left(\frac{[L\,(1\text{-}v^2)\,(P_f\text{-}S_3)]}{E}\right)^3 DP. \qquad \text{(Eq. 15)}$$

Thus, the flow rate through a fracture responding to a pressure gradient will be proportional to the cube of the product of fracture length (L) times the difference between the fluid pressure (P_f) inside the fracture and S_3. That is, the fluid pressure (P_f) inside the fracture is trying to open the fracture, while S_3 is trying to close the fracture.

Aguilera (1980) cast the flow through fractures in terms of permeability (K_f in Darcy) as

$$K_f = (54 \text{ X } 10^6)\, W^2, \qquad \text{(Eq. 16)}$$

where W (fracture width, fracture aperture) is in inches. Consequently, the flow rate through a fracture is proportional to the cube of the aperture responding to S_3 (Equation 13), where fracture permeability is proportional to the square of the aperture responding to S_3 (Equation 16). For reference, Aguilera (1980) pointed out that the average permeability, or "system permeability," of 13510 millidarcy (md) results when a 1 md rock with dimensions of one cubic foot (1 ft^3) contains three fractures each with an aperture of 0.01 of an inch. Fractures make a great difference in system permeability. It is the fracture's aperture, responding to stress, that controls the magnitude of that difference.

Bandis et al. (1983) illustrated, through laboratory experiments, that fracture aperture is controlled by stress normal to the fracture. Stress of 3000 psi (20.6 MPa) normal to a fracture

surface will reduce the initial aperture by 40% with one stressing cycle. After three cycles of stressing the aperture is reduced by approximately 60%. Gutierrez et al. (2000) completed a series of laboratory experiments on shales and documented that stress of 1450 psi (10 MPa) normal to a fracture surface will reduce the initial permeability by 90%. Stress can degrade fracture permeability even if one places propping agents in the fracture aperture. Gidley et al. (1984) demonstrated that a fracture packed with propping agents experienced a substantial loss of permeability due to grain crushing, embedment, and subsequent development and migration of fines when exposed to normal stress above 3000 psi (20.6 MPa) to 4000 psi (27.6 MPa). In summary, normal effective stresses above 2000 psi (13.7 MPa) to 3000 psi (20.6 MPa) can significantly discourage the ability of a fracture to allow fluids to flow along the surface.

Effect of shear stress on fluid flow along a planar mechanical discontinuity:

In a situation where the host rock permeability is much less than 0.001 md, the pressure within the mechanical discontinuity (P_f) can be different than the pore pressure (P_p) of the host rock (i.e., low leak off). A planar mechanical discontinuity oriented within a stress field defined by S_V, S_H, S_h, and S_{Haz} (as depicted in Figure 12), will fail in shear (Mode II or Mode III) when the magnitude of the shear stress (Ss) is greater than the product of the coefficient of sliding friction (μ) and the normal stress (Sn) less the pressure within the mechanical discontinuity (P_f),

$$Ss > \mu (Sn - P_f). \qquad \text{(Eq. 17)}$$

Such shear failure results in sliding along the surface and subsequent dilation (opening) due to riding up on asperities positioned along the surface (Barton et al., 1985). Such a state of shear failure is recognized as a “critically stressed” situation, although the term *reactivation* is

preferred here. Barton et al. (1995) recognized that fluid flow is encouraged along reactivated faults; a principle that was subsequently extended to fractures by Zoback (2007) and is corroborated by personal experience.

Considering the relationship

$$Ss = \mu (Sn - P_{fr}) \qquad \text{(Eq. 18)}$$

such that P_{fr} is the pressure within the mechanical discontinuity (not P_p) which will be responsible for the initiation of reactivation. Solving for P_{fr}, the relationship

$$P_{fr} = \frac{(\mu\, Sn - Ss)}{\mu} \qquad \text{(Eq. 19)}$$

is obtained. Therefore, for a given set of Sn, Ss, and μ, the P_{fr} can be calculated.

In the previous section, estimates of Sn and Ss were obtained for a surface described by strike and dip. Following the same logic, one can now calculate P_{fr} for a given coefficient of sliding friction (μ) for any strike-dip combination. Results of such calculations using parameters of Example 2 (Table 3) are presented in Table 5 in the same discretized strike and dip format as Table 4. In this case, the lowest value of P_{fr} occurs in two places, strike of 0° and dip of 85°, and strike of 60° with dip of 85°. Thus, if fractures with these orientations exist, they would be more apt to encourage fluid flow along their surfaces than other strike-dip combinations.

Worth noting is the phenomenon that once a mechanical discontinuity has been reactivated, the "fall-off" pressure response to the process of "deactivation" should not be misconstrued as "closure pressure" associated with a value for S_h from a linear elastic Mode I fracture. Couzens-Schultz and Chan (2010) present a field study demonstrating the potential confusion.

Dip	0	15	30	45	60	75	90	105	120	135	150	165	180	195	Strike	Dip
85	3553	3819	4567	3819	3553	4139	5440	7106	8623	7106	5440	4139	3553	3819	4567	85
75	3636	3719	4019	3719	3636	4264	5527	7119	8441	7119	5527	4264	3636	3719	4019	75
65	3836	3703	3774	3703	3836	4505	5698	7148	8249	7148	5698	4505	3836	3703	3774	65
55	4185	3902	3857	3902	4185	4871	5943	7198	8079	7198	5943	4871	4185	3902	3857	55
45	4696	4355	4260	4355	4696	5340	6255	7277	7946	7277	6255	5340	4696	4355	4260	45
35	5361	5037	4933	5037	5361	5901	6620	7389	7863	7389	6620	5901	5361	5037	4933	35
25	6130	5881	5797	5881	6130	6525	7019	7539	7846	7539	7019	6525	6130	5881	5797	25
0.7	0	15	30	45	60	75	90	105	120	135	150	165	180	195	210	Strike

Table 5. The value in each cell represents the pressure (P_{fr} in psi) within a fault, fracture, crack, bedding plane surface required to reactivate and fail in shear at the posted strike and dip values. Values assume constant coefficient of sliding friction (u) of 0.7 (posted in the lower most left cell) and zero cohesion. Color code is as follows: Yellow: Required pressure for reactivate that is less than S_h.; Blue: Reactivate at pressures that are greater than S_h; Red: Reactivation pressure less than mud pressure.

Given the influence on fluid flow that stress normal to the discontinuity commands, the effectiveness and preservation potential of shear-induced dilation along a discontinuity can be evaluated by combining the reactivation pressure and the normal stress acting on that discontinuity. Table 6 represents such a combination by taking the average of the effective, reactivation pressure (removing the influence of pore pressure) and the effective normal stresses as a function of strike and dip. Such a combination can shift the orientation of the most likely for preservation from the orientation of the most likely for reactivation (Table 5).

Summary

I have presented a methodology for evaluating the potential for flow along the surfaces of mechanical discontinuities (faults and fractures) as a function of reactivation. The approach is to first describe the rock strength, then characterize the present-day stresses. Next, one establishes the normal and shear stresses acting on surfaces of mechanical discontinuities that are described spatially by strike and dip. This is followed by determining the pressure magnitude within each surface required to initiate reactivation. Finally, one has to review the magnitude of pressure sources such as pore pressure, drilling fluids, completion fluids, and injection fluids with respect to the reactivation pressures. If any of the sources exceeds the reactivation pressure for a particular strike and dip, then fractures in that orientation are prone to reactivate and allow fluids to flow along their surfaces.

	= Bottom 25%															Lowest
Dip	0	15	30	45	60	75	90	105	120	135	150	165	180	195	Strike	Dip
85	1232	1023	1271	1023	1232	1993	3112	4288	5172	4288	3112	1993	1232	1023	1271	85
75	1339	1059	1091	1059	1339	2093	3165	4283	5062	4283	3165	2093	1339	1059	1091	75
65	1562	1212	1144	1212	1562	2284	3268	4277	4931	4277	3268	2284	1562	1212	1144	65
55	1902	1529	1422	1529	1902	2562	3414	4274	4799	4274	3414	2562	1902	1529	1422	55
45	2346	2003	1892	2003	2346	2904	3597	4281	4679	4281	3597	2904	2346	2003	1892	45
35	2867	2591	2498	2591	2867	3292	3807	4305	4584	4305	3807	3292	2867	2591	2498	35
25	3417	3231	3166	3231	3417	3699	4030	4352	4528	4352	4030	3699	3417	3231	3166	25
	0	15	30	45	60	75	90	105	120	135	150	165	180	195	210	Strike

Table 6. Results showing effective reactivation and effective normal stress derived from Example 2 stress state. Compared to Table 5, notice how the orientation of the lowest value has moved closer to the orientation of S_{Haz}. For a natural fractured system, such a plot could indicate the fracture orientation that has the highest chance for reactivation and permeability preservation.

LABORATORY FLOW EXPERIMENT

Introduction:

A series of experiments, which monitored the flow of dry air as a function of stress along the strike of preexisting fractures in a cylindrical sample of Berea Sandstone (Figure 13) were conducted at ConocoPhillips' Rock Mechanics Laboratories in Bartlesville Oklahoma. The object of the experiments was to set up a laboratory experiment which would emulate the presented methodology and duplicate the field observations of Barton et al. (1995) that associated fluid flow with reactivation along preexisting mechanical discontinuities. The flow rate was monitored as the confining and axial stresses were increased through reactivation.

Procedure:

A cylindrical sample was extracted from a block of Berea Sandstone, which has a permeability to air of approximately 300 millidarcy and a porosity of roughly 20%. After trimming the ends square, the approximately 1 inch (2.54 cm) in diameter and 2 inches (5.08 cm) long sample was placed into a Teflon jacket (Figure 14). The sample was then positioned in a cell so that confining stress could be applied and the sample pore pressure could be vented to the atmosphere (drained test). Placing the confining cell in a stiff loading system (Figure 15), allowed application of axial stress and established the triaxial loading system. Subsequently, the sample was subjected to an increase of axial stress from 1300 psi (9 MPa) to 13157 psi (90.7 MPa) at room temperature and a constant confining stress of 1000 psi (6.9 MPa). Applying axial stress of 13157 psi (90.7 MPa) just exceeded the strength of the rock (Ultimate Strength) and induced failure, which resulted in the formation of a set of conjugate

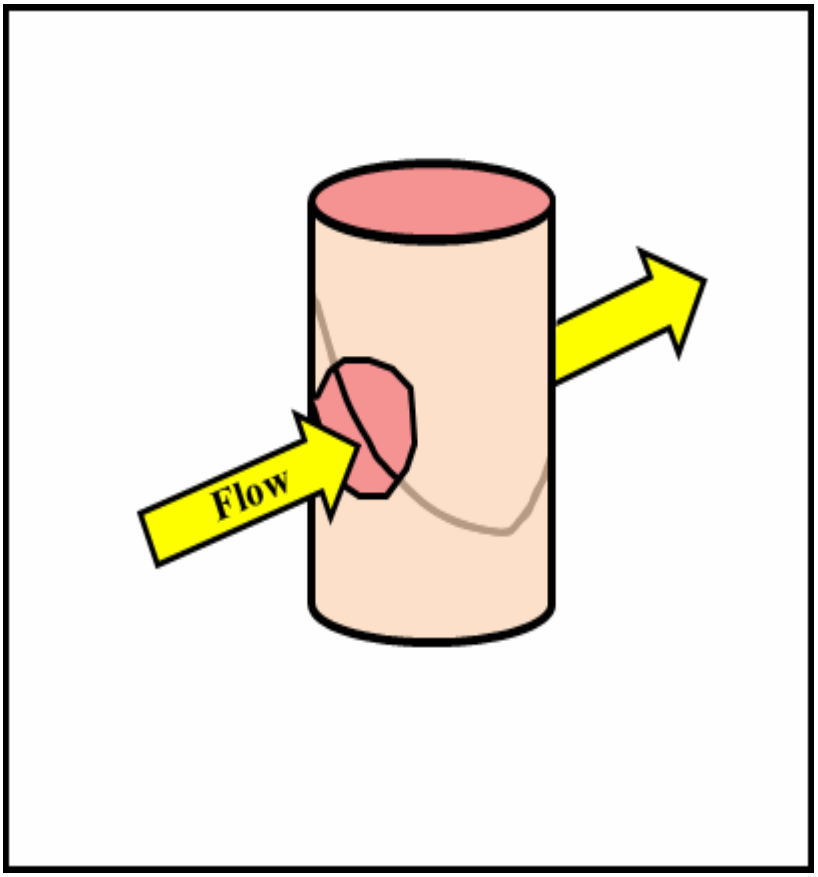

Figure 13. Illustration of air flow along the strike of a preexisting fracture in a cylindrical sample encased within a semitransparent jacket into which openings have been cut.

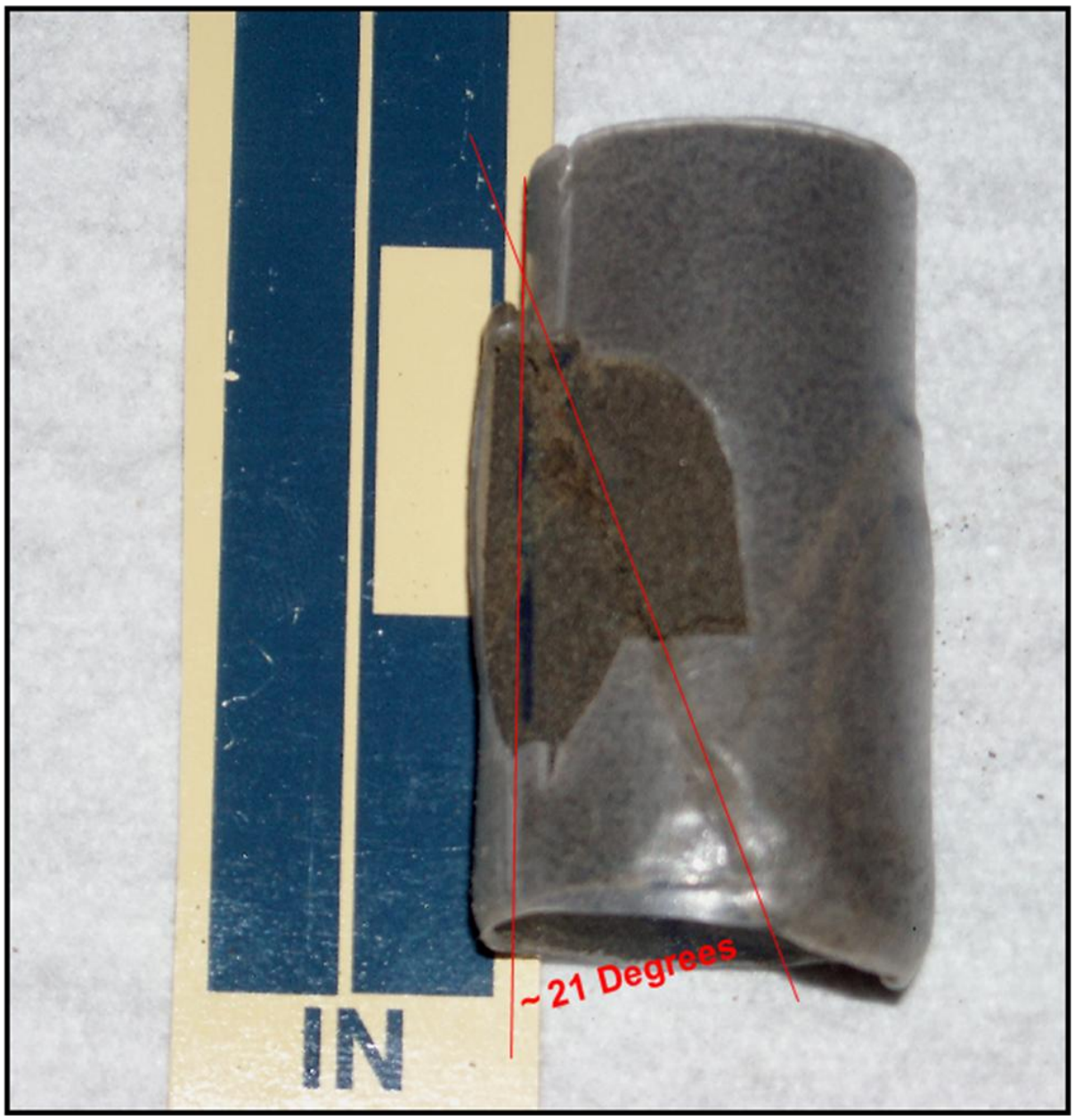

Figure 14. Photograph of shear-fractured sample in the Teflon jacket with openings after being extracted from the radial flow-through Hassler coreholder at the conclusion of the test. During the final unloading processes, the test sample was exposed to hydraulic fluid resulting in a color darkening compared to natural dry state (*see* Figure 18). The angle between the sample axis and dominate fracture is approximately 21°.

Figure 15. TerraTek 375 ton stiff loading system used for the experiment.

shear fractures (Figure 14). Throughout the experiment, stress and strain data were recorded (Figure 16).

After failure, the rock sample was removed from the triaxial loading system. Two openings, aligned along the strike of the induced fractures, were cut into the Teflon jacket (Figure 14). The jacketed sample was placed in a radial flow-through Hassler coreholder (Figure 17a) with the ports of the coreholder aligned with the openings in the Teflon jacket and strike of the fracture. The sample was then repositioned in the triaxial loading system (Figure 17b). With a constant up-stream pressure of 56 psi (0.38 MPa), the flow rate of dry air at room temperature was continually monitored with an Agilent AMD2000 digital flow meter as the air passed through the radial flow-through Hassler coreholder and the fractured sample before venting to the atmosphere. Under normal circumstances flow rate should have been recorded, in milliliter per minute (mL/min), via a RS232 interface every 4.9 seconds throughout the 16 hour stressing. Unfortunately, a persistent problem would randomly halt the flow data from being recorded and required a manual restart. As a result there are numerous intervals of missing flow data (Figure 18).

Initially the confining stress on the sample was brought to 494 psi (3.4 MPa), while the axial stress was increased to about 700 psi (4.8 MPa). Around hour 18.5 of system elapsed time, the axial stress was increased, under strain control, at a rate of 0.1 % strain per hour and continued at that rate for the next 10 hours except for a hold period between hour 22 and 23. At hour 28.65, unloading started and continued to hour 34 (Figure 18).

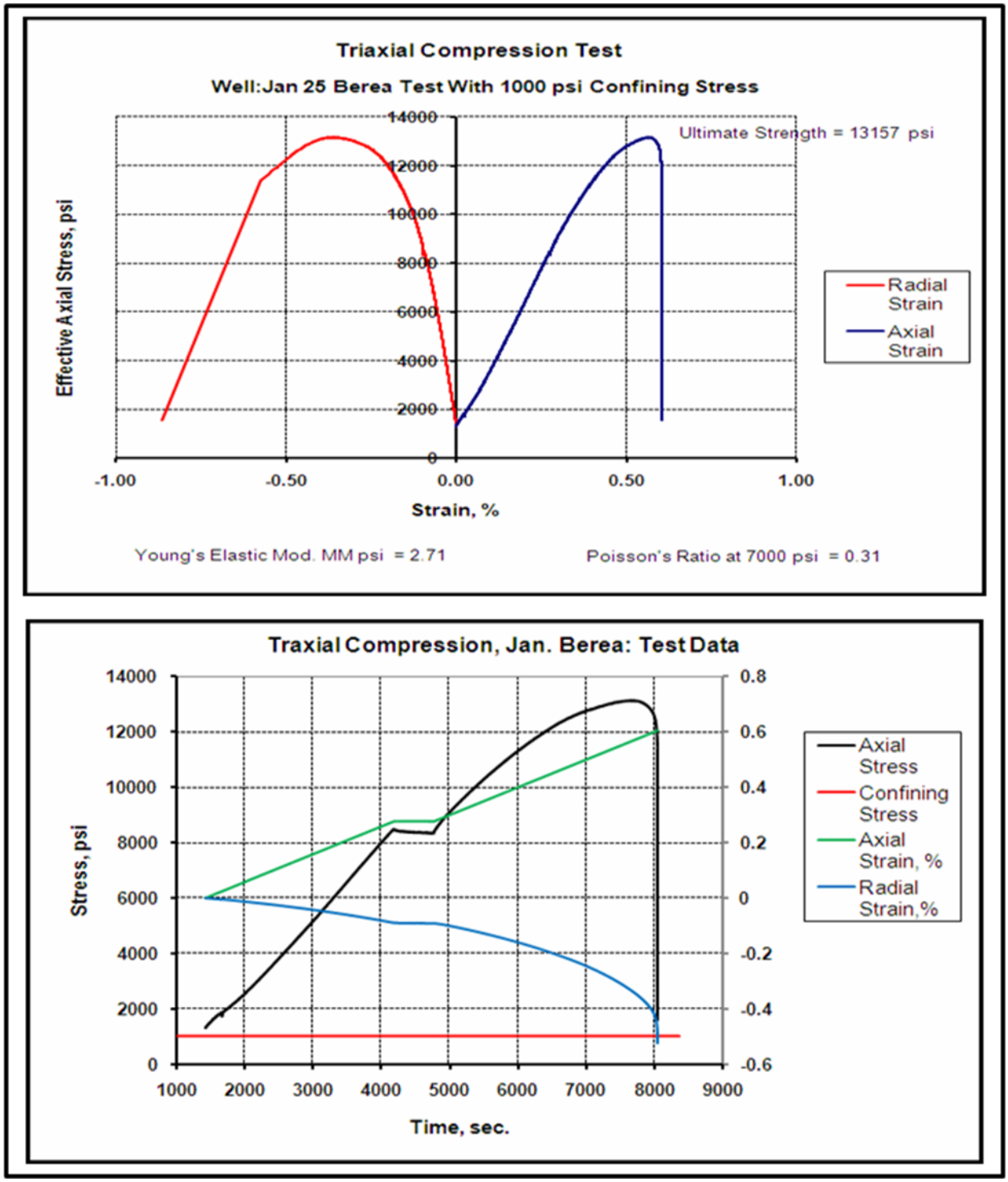

Figure 16. Stress strain record for the initial failure

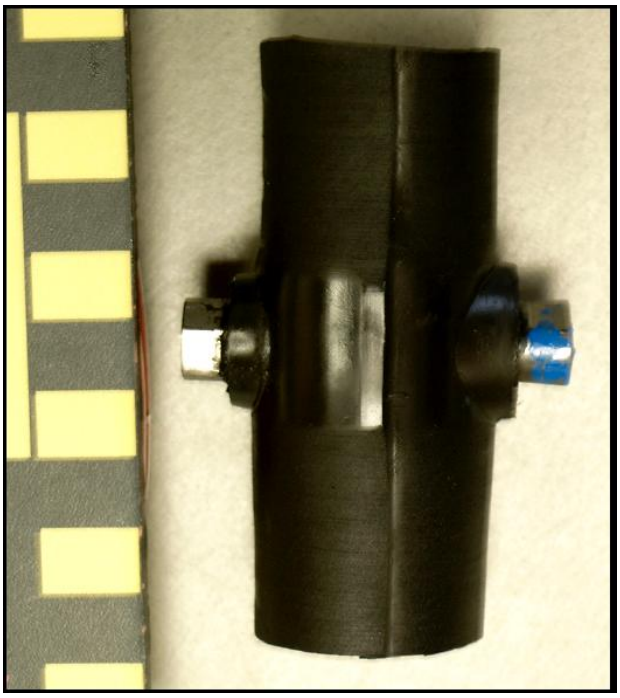

Figure 17a. Radial flow-through Hassler coreholder.

Figure 17b. Radial flow-through Hassler coreholder positioned in the triaxial compression loading configuration.

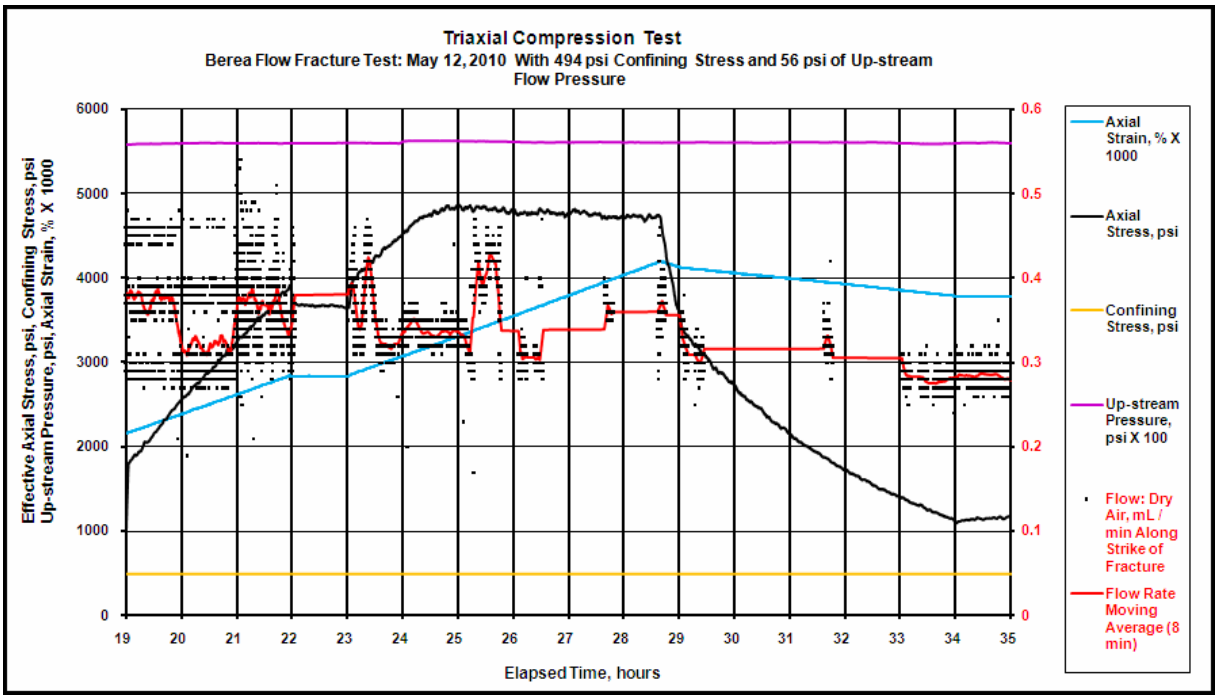

Figure 18.Data from flow test.

Discussion:

In much the same manner that UCS can be calculated from cohesion and internal friction angle (Eq. 1), UCS can also be estimated from a single triaxial test taken to failure using the effective confinement (Sc'), which is confining stress less the pore pressure, Ultimate Strength (US), and internal friction angle (IFA) in the following manner

$$UCS = US - (Sc' \{[1 + (\text{Tan IFA})^2]^{0.5} + (\text{Tan IFA})\}^2) \quad \text{(Eq. 20)}$$

For reference, the last part of Equation 20

$$(\{[1 + (\text{Tan IFA})^2]^{0.5} + (\text{Tan IFA})\}^2)$$

is presented in Appendix 2 as "Confinement Multiplier from Internal Fraction Angle". The IFA can be estimated from the angle that forms between the axial stress and the plane which best describes the rock failure (ARF) such that

$$IFA = 90 - 2ARF. \quad \text{(Eq. 21)}$$

For the sample in the experiment, ARF is approximately 21° (Figure 14) resulting in an IFA estimate of 48°. With US equal to 13157 psi (90.7 MPa) (Figure 16) and Sc' approximately 1000 psi (6.9 MPa), a UCS of 6300 psi (43.4 MPa) is calculated. Dimple analyses of the companion block of Berea Sandstone from which the test sample was extracted resulted in dimple diameters of 6 ticks (Figure 19), which suggest a UCS of approximately 5500 psi (37.9 MPa) (Figure 4). These two UCS values are in reasonable agreement. Dimple analyses of the test sample after the conclusion of the experiment resulted in dimple diameters of 10 ticks (Figure 18), which correlate with an UCS of approximately 2100 psi (14.5 MPa) (Figure 4). These measurements illustrate the effects of recently imbibed fluids, especially oil, on the analyses.

Figure 19. Berea Sandstone Dimple test of companion block and test sample. Dimple diameters of 6 and 10 ticks, respectively. The color darkening and larger Dimple diameter on the test sample is due to the exposure to hydraulic fluid.

With the axial stress vertical, the confining stress is equal to the horizontal stresses (S_h and S_H). Furthermore, since the axial stress within the triaxial loading cell is greater than confining stress, a normal fault condition persists. Since S_h and S_H are the same, the stress state of the sample within the cell lies on the equality line for the representative Stress Polygon (Figure 20).

With ARF equal to 21° and the axial stress being vertical, the plane which best describes the rock failure dips 69°. Using the method described earlier (*see* section "Normal and Shear Stresses Magnitudes Acting on an Arbitrarily Oriented Planar Mechanical Discontinuity") applied confining and axial stresses (Figure 18) are used to calculate both the normal (Sn) and shear (Ss) stresses acting on the plane dipping 69°. Reviewing the axial stress and strain curves (Figure 18), the axial stress curve starts to flatten between hour 24.7 and hour 25.3. Such a marked change of slope of the axial stress in a strain controlled experiment suggests slip movement (reactivation) along the fracture(s). Solving for coefficient of sliding friction (μ) in Equation 18 renders

$$\mu = Ss / (Sn - P_{fr}) \qquad \text{(Eq. 22)}$$

where Sn and Ss are the normal and shear stresses, respectively, acting on the fracture surface, and P_{fr} is the pressure within the mechanical discontinuity. At low injection (flow) rates P_{fr} is equal to pore pressure in a permeable rock. Using the normal and shear stress conditions for hour 25 of the experiment (Figure 21) and a P_{fr} equal to 25 psi (0.17 MPa), a μ of approximately 1.41 is obtained. Similar calculations for reactivation pressures can be performed for all time increments of the experiment (Table 7). For example at hour 24 with a μ

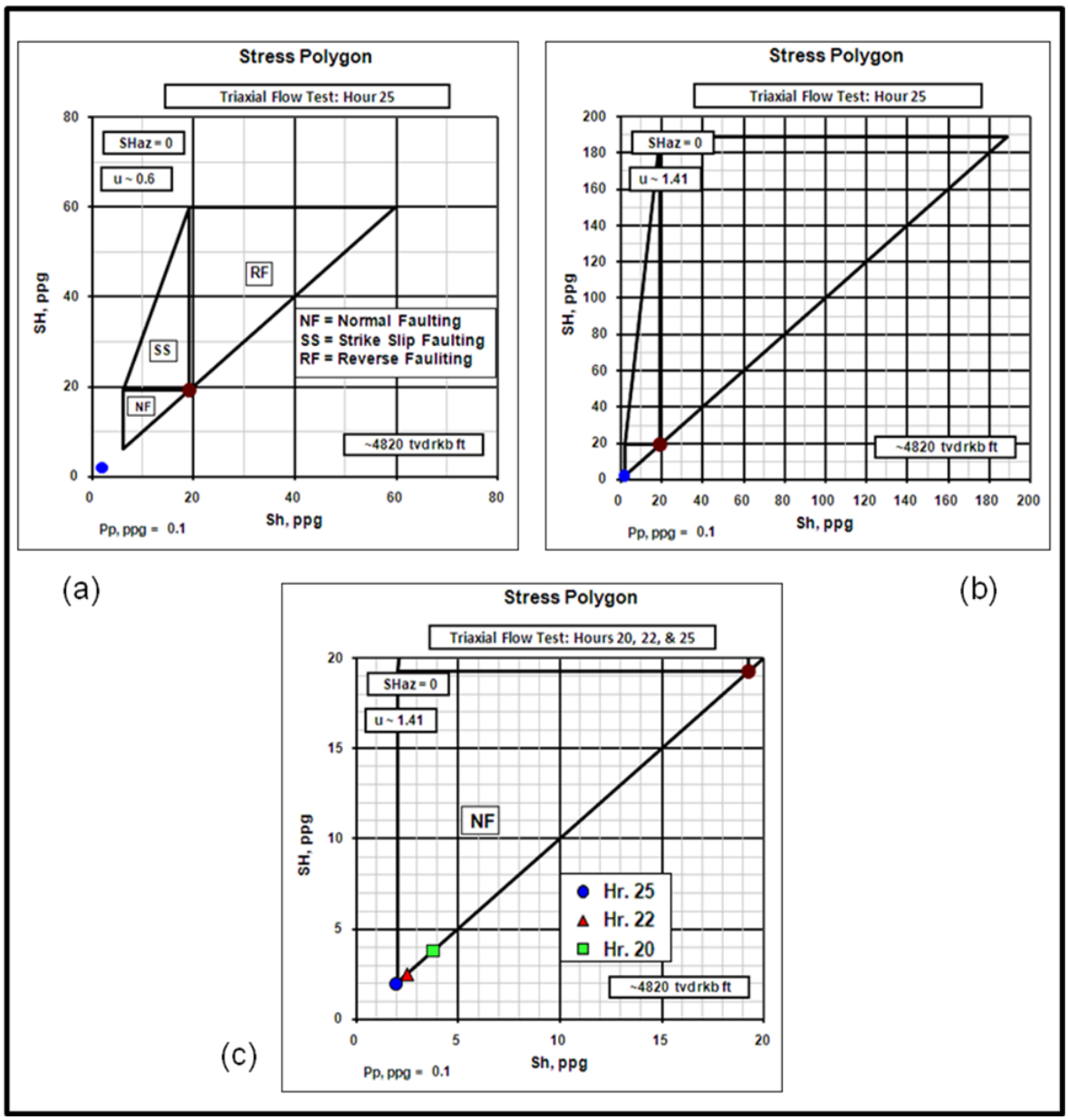

Figure 20. (a.) Stress Polygon representing the stress state within the stress cell at hour 25 using an anticipated μ of 0.6 derived from UCS (6300 psi) and Figure 21. In order to use the analysis tools available, it was necessary to emulate the conditions within the stress cell as a well drilled in an area that has a Sv gradient very close to 1 psi/ft and a pore pressure relative close to zero. Note that the stress state (blue dot) is outside the polygon suggesting a non-natural condition. Further note that the polygon is rather large due from the low pore pressure. (b) In order to get the stress state close to the polygon boundary a μ of 1.41 is necessary, which significantly increases the polygon. (c) Illustrates the Normal Fault section of (b) with the stress states posted for hour 20 and 22 along with hour 25 to help visualize the change of stress state through the first half of stressing cycle.

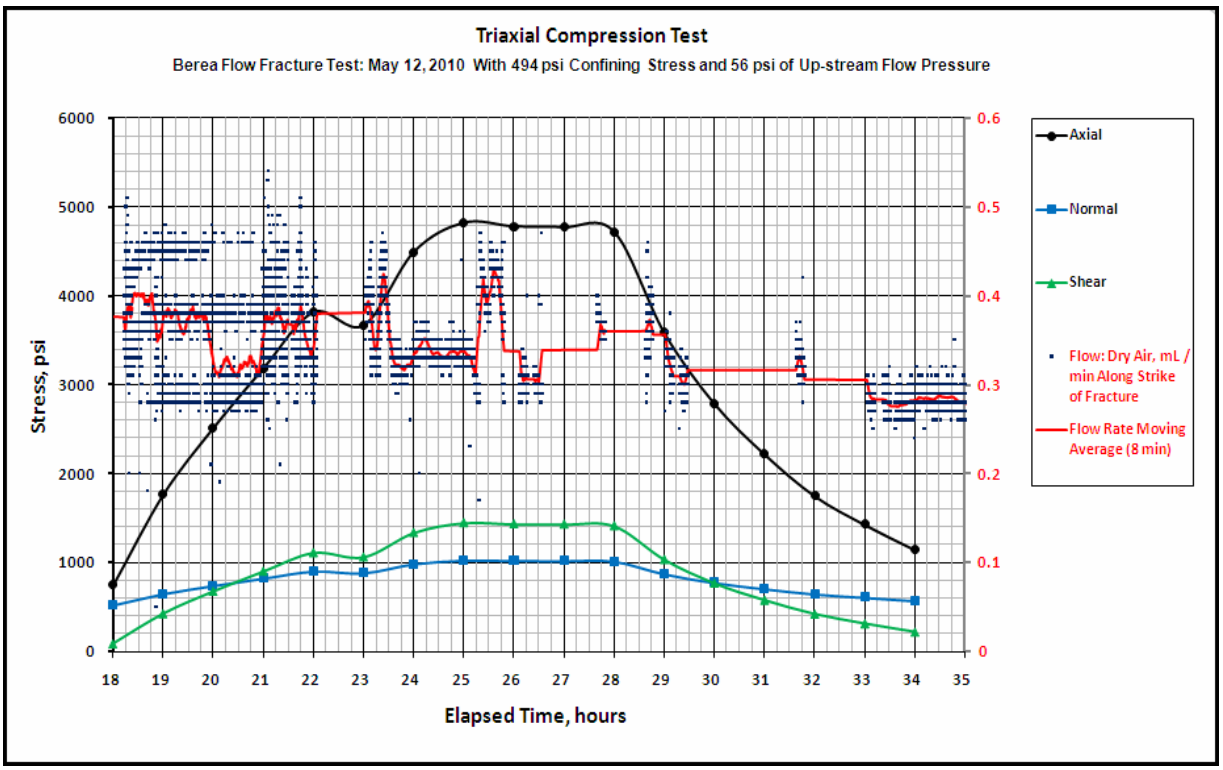

Figure 21. Flow data with axial stress and calculated normal and shear stresses acting on the fracture dipping at 69°.

Dip	0	15	30	45	60	75	90	105	120	135	150	165	180	195	Strike	Dip
85	260	260	260	260	260	260	260	260	260	260	260	260	260	260	260	85
75	15	15	15	15	15	15	15	15	15	15	15	15	15	15	15	75
65	90	90	90	90	90	90	90	90	90	90	90	90	90	90	90	65
55	476	476	476	476	476	476	476	476	476	476	476	476	476	476	476	55
45	1122	1122	1122	1122	1122	1122	1122	1122	1122	1122	1122	1122	1122	1122	1122	45
35	1956	1956	1956	1956	1956	1956	1956	1956	1956	1956	1956	1956	1956	1956	1956	35
25	2872	2872	2872	2872	2872	2872	2872	2872	2872	2872	2872	2872	2872	2872	2872	25
1.41	0	15	30	45	60	75	90	105	120	135	150	165	180	195	210	Strike

Table 7. As in Table 5, this table reflects the reactivation pressure (psi) for hour 25 stress conditions using a $\mu = 1.41$. Since $S_H = S_h$, directionality is lost and all strikes have the same value. In the stress cell, the fracture is dipping approximately 69°, which is not directly posted, the reactivation pressure resides between 90 psi (for 65° of dip) and 15 psi (for 75° of dip). Performing the calculation using Equations 11, 12, and 19 for a dip of 69° results in a value of 25 psi (0.17 MPa)

equal to 1.41 the reactivation pressure is 65 psi (0.45 MPa) (Table 8) which is 40 psi higher that that a hour 25. Interestingly, a μ of 1.41 appears high for rock strength of 6300 psi UCS where the expected values are in the range of μ equal to approximately to 0.6 (Figure 22). The two-fold increase in the coefficient of sliding friction most likely reflects the combined stiffening influence of the Teflon jacket, Hassler coreholder, and "end effects" on a relative small test sample.

At the beginning of the loading sequence, at hour 19, the dry air flow rate (Figure 18, 21, 23, and Appendix 1) averaged approximately 0.37 mL/min, while the flow rate decreased to approximately 0.28 mL/min near the end of the loading sequence at hour 34. During the intervening fifteen hours, the flow rate decreased by 24% as 4.2% strain occurred. 4.2% strain translates to 0.084 inch (0.2 cm) of displacement. The most abrupt decrease in flow rate occurred at hour 26.

The character of the flow rate seems to be associated with strain and changes in shear and normal stress acting on the fracture surfaces. Between hour 19 and hour 20, when the normal stress acting on the fracture surface is greater than the shear stress, the flow rate fluctuated symmetrically by plus or minus 0.09 mL/min around the average value of 0.37 mL/min, although the fluctuations appear to occur randomly with time (Figure 23a). Once the shear and normal stress were about equal, between hour 20 and hour 21, the flow rate fluctuated asymmetrically about 0.37 mL/min, with the majority of the excursions lower than 0.37 mL/min (Figure 23b). When the shear stress exceeded the normal stress at about hour 21, the character of the flow rate changed to an organized cyclic pattern in which a single cycle initially started with a relative rapid increase in flow rate followed by a slower apparently semi-linear decline in flow rate (Figure 23c). Repetition of the cycle produced an asymmetric

Dip	0	15	30	45	60	75	90	105	120	135	150	165	180	195	Strike	Dip
85	280	280	280	280	280	280	280	280	280	280	280	280	280	280	280	85
75	54	54	54	54	54	54	54	54	54	54	54	54	54	54	54	75
65	124	124	124	124	124	124	124	124	124	124	124	124	124	124	124	65
55	478	478	478	478	478	478	478	478	478	478	478	478	478	478	478	55
45	1075	1075	1075	1075	1075	1075	1075	1075	1075	1075	1075	1075	1075	1075	1075	45
35	1845	1845	1845	1845	1845	1845	1845	1845	1845	1845	1845	1845	1845	1845	1845	35
25	2692	2692	2692	2692	2692	2692	2692	2692	2692	2692	2692	2692	2692	2692	2692	25
1.41	0	15	30	45	60	75	90	105	120	135	150	165	180	195	210	Strike

Table 8. Reactivation pressure (psi) for hour 24 stress conditions. For a dip of 69°, the reactivation pressure is calculated to be approximately 65 psi (0.48 MPa).

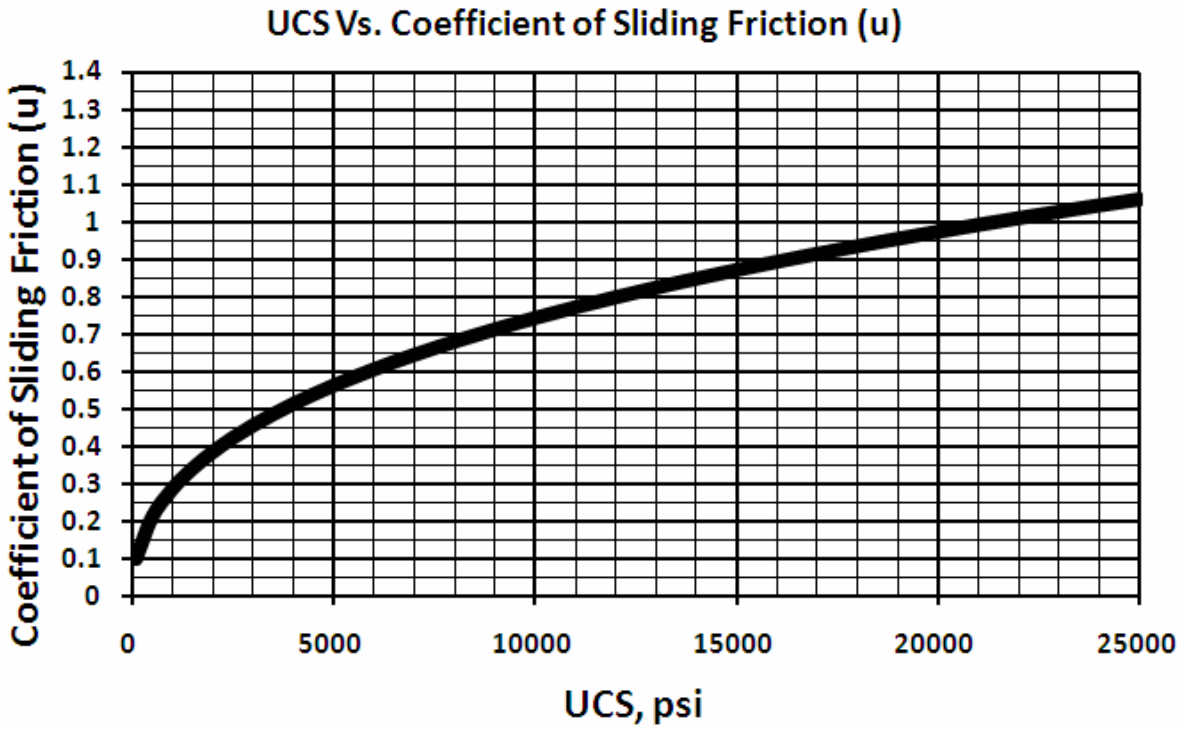

Figure 22. Correlation between UCS and Coefficient of Sliding Friction (μ) derived from incorporating the work of Byerlee (1978), Moos and Zoback (1990), and Zoback (2007) with personal field experience (Enderlin, 1998, unpublished).

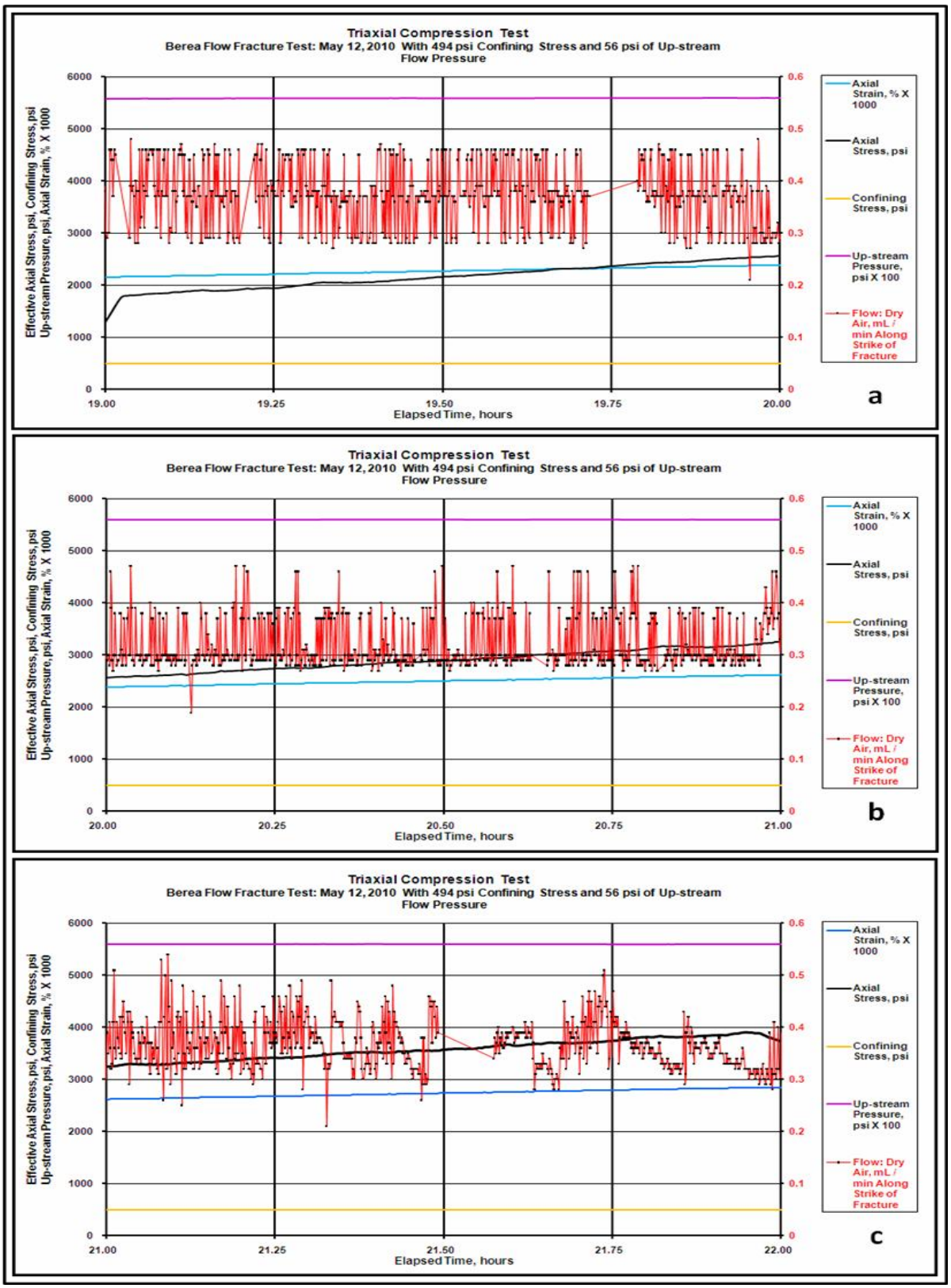

Figure 23. Changing character of flow rate with time. a. hour 19, b. hour 20, and c. hour 21.

saw-tooth pattern with time. The organization in the *saw-tooth* pattern became better defined and the time between saw-tooth flow maximums started to increase with increasing difference between the shear and normal stress. When the shear stress exceeded approximately 1000 psi (6.9 MPa) at hour 21.5, the time differential between maximums continued to increase and reached a maximum at onset of fracture surface sliding at hour 25 (Figure 24). Once sliding begins (reactivation), the flow rate retains a saw-tooth character, but the average rate first suddenly increases to an average of 0.43 mL/min at hour 25.6 (Figure 24) before rapidly decreasing to an average of 0.3 mL/min near the beginning of hour 26 (Figure 25). The decrease in flow rate at beginning of hour 26 seems significant as it precedes continued lower flow rates, although the gaps in the data make this interpretation ambiguous. Between hour 24 and hour 26, 0.2% strain accumulated, presumably by slip along the fracture. Strain of 0.2% translates to 0.004 inches (0.0049 cm) of sliding. For a rock with an average grain size of about 0.007 inches, it is unclear if 0.004 inches of sliding is enough to cause the generation of sufficient volume of gouge to partially plug the flow paths and reduce the flow rate (Barton and Choubey, 1977; Olsson. 1992,). Unfortunately, the flow data is sparse beyond hour 30 when the normal stress again exceeds the shear stress. However, by hour 33 the flow rate averages a value of 0.28 mL/min again with random pattern but smaller positive and negative fluctuations of 0.03 mL/min with time.

Implications:

The experiment needs to be viewed as preliminary and is only marginally applicable to the overall goals of this study since the Berea Sandstone is not a low permeability rock. The asymmetric saw-tooth flow rate pattern, however, is of interest since it consists of cycles of rapidly increasing flow rates followed by a slower semi-linear decline in flow rate with time.

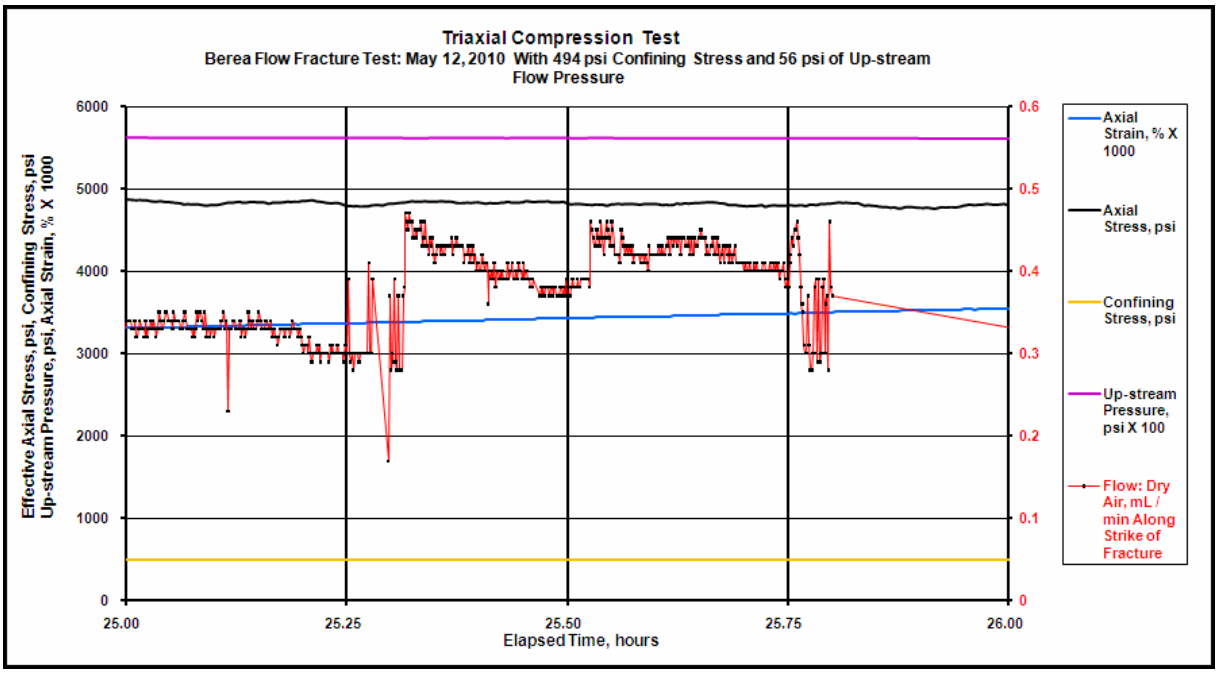

Figure 24. Character of flow rate for hour 25.

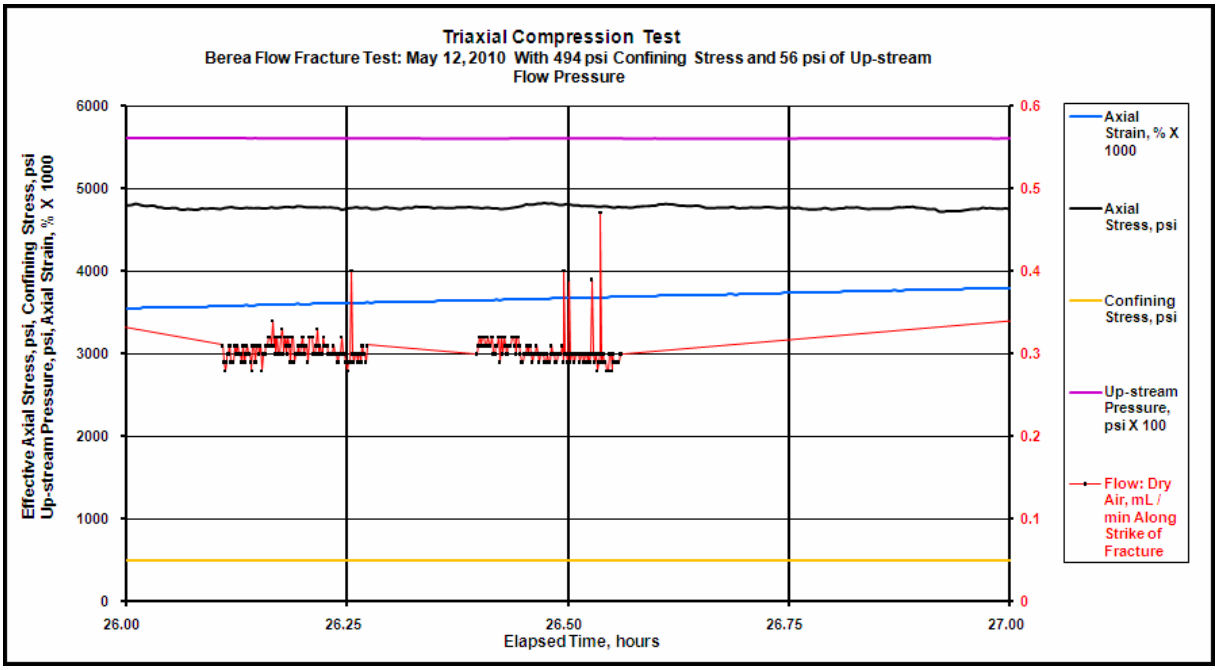

Figure 25. Character of flow rate for hour 26.

The dependence of the saw-tooth pattern development on relative magnitudes of shear and normal stress may seem perplexing. It is possible that the shear stress acting on asperities along the fracture surfaces is not evenly distributed. In that case, there are locations where some asperities are experiencing practically no shear stress, while other asperities are stressed to near failure. Furthermore, shear stress may act on asperities in a semi-uniaxial manner but with some directional confinement due to the effective normal stress. The asperities that are stressed to near failure experience dilatation via Mode I fracture or form proto-Mode II or Mode III fractures through coalescing Griffith cracks, thereby increasing flow. As the stress increases, asperities stressed to near failure will fail and the stress is shifted to neighboring asperities creating a patch of cascading *stick-slip* like stressing and failures, producing, in time, a semi-linear decay of the elevated flow rate that continues until equilibrium is restored. The cycles, much like smaller and smaller aftershocks follow a large earthquake, result in a *saw-tooth* flow pattern. The results are localized zones of patchy *stick-slip* flow (PSSF) that develop at stress magnitudes that are lower (e.g., hour 21 in the experiment) than the magnitudes required for the blocks on either side of the fracture surface to slip (complete reactivation) as apparently happened at hour 25. Such a supposition suggests that the level of shear stress and confinement on the asperities along a fracture surface is not uniform. The distribution of stress is likely bounded at zero on the low end and by the ultimate strength at the other, assuming full triaxial confinement. By definition the asperity is a rugged projection, implying numerous free surfaces, thereby reducing any confining effects from its surroundings (i.e. nearly unconfined). In that situation the normal stresses tend to reduce the fracture aperture and increase confinement on the asperities in a direction normal to the fracture surface. Even in conditions

of high normal stress, there are many other directions within the fracture plane that are potentially free from confinement that could permit the development of PSSF zones within the near surface volume. One might envision PSSF zones developing as a network along the fracture surfaces.

Although the nature of the stress distribution on asperities remains enigmatic, it is tempting to assume that a fracture surface in rocks of low UCS (below ~8000 psi; 55.1 MPa) would find more asperities stressed to near failure than a rock of high UCS (above ~15000 psi; 68.9 MPa) for a given shear stress. Such a circumstance would imply that for the same shear stress, fewer PSSF zones would occur in strong rocks compared to weaker rocks. If this situation is partially true, it would suggest an elevated fluid flow rate along the fracture surface of strong rocks requires a stress state that would induce reactivation (block movement). In contrast, block movement is not necessary to achieve elevated fluid flow rate along fracture surfaces in weak rocks and all that is required is that the stress state approaches reactivation.

Summary of Experiment and Future Direction:

The highest average flow rate (average just over 0.42 mL/min) occurs at hour 25.6 when blocks of the fracture surfaces initially slipped (reactivated). That being the case, the objective of the laboratory experiment was met.

The next set of experiments needs to repeat the Berea Sandstone test. Once repeatability is observed, following tests need to be conducted with strong very low permeability rock samples. Strength increase, in some measure, may offset the stiffening influence of the Teflon jacket and Hassler coreholder thereby achieving a more realistic coefficient of sliding friction. If possible, the experimental instrumentation should also include Acoustic Emissions (AE) measurements.

APPLICATION

The following section applies the above methodology to observations from the Barnett Shale derived from the T.P. Sims #2 well. The section consists of a concise step-by-step analysis beginning with required information and premises and concluding with a particular strike and dip combination that was apparently reactivated.

In 1990, Mitchell Energy drilled the near vertical T.P. Sims #2 well close to the county line between Wise and Denton counties in north-central Texas. Much of the Barnett Shale section was cored and stimulation diagnostic tests were performed. Most of the information used here comes from three sources: 1) Lancaster et al. (1992) provided reservoir engineering, core data, and basic fracture description; 2) Gale et al. (2007) presented fracture characterization; 3) rock strength data presented here.

Initial Information:

a. Depth: approximately 7700 ft (2346.9 m) (Lancaster et al., 1992)
b. Vertical well (Lancaster et al., 1992)
c. Reservoir fluid: Gas (Lancaster et al., 1992)
d. Pore pressure: approximately 4000 psi (27.5 MPa) (approximately 0.52 psi/ft) (Lancaster et al., 1992)
e. Average Rho_b for Barnett: 2.55 (Lancaster et al., 1992)
f. Average compressional slowness (DTc) for Barnett: approximately 82 μsec/ft (Lancaster et al., 1992)
g. Average log porosity for Barnett: approximately 5% (Lancaster et al., 1992)
h. Average "crushed" core porosity approximately 6% (Lancaster et al., 1992)

i. Average volume clay approximately 24% (Loucks and Ruppel, 2007)

j. Reservoir Temperature 190° F (87.8° C) (Lancaster et al., 1992)

k. Caliper log (Lancaster et al., 1992) through Barnett indicates a smooth "in-gauge" borehole therefore suggests the absence of breakouts.

l. Natural fractures strike 105° and dip at 74° (Lancaster et al., 1992; Gale et al., 2007)

m. Presence of some, not ubiquitous, drilling induced fractures (Lancaster et al., 1992; Gale et al., 2007)

n. Orientation of S_H (S_{Haz}) approximately 60° (Gale et al., 2007)

Initial Premises:

a. Static mud weight: approximately 9.4 ppg with effective circulating density (ECD) approximately 9.6 ppg

b. Average overburden density approximately 2.3 g/cm^3 = 19.4 ppg

Analysis Sequence

1. Determination of rock strength from log measurements and dimpler testing.
    a. Strength from logs:
        (1) The presence of over-pressured gas needs to be accounted for in both DTc (82 μsec/ft) and Rho_b (2.55 g/cm^3) measurements. After the gas has been replaced (Sw = 100%) with "brine" and reduced to "normal" pressure results DTc = 73 μsec/ft and Rho_b = 2.56 g/cm^3.

(2) Using Figure 1 (sandstone, Vshale = 0 algorithm) yields an Unconfined Compressive Strength (UCS) value of ~9000 psi (62 MPa). Since the Barnett shale is considered a mudstone, experience has indicated that for Vshale = Vclay between 10% and 35%, the UCS generally increases up to ~10% over the Vshale = 0 case resulting in a UCS of ~ 10000 psi (68.9 MPa).

b. Dimple testing: Figure 3 illustrates the device and measurement procedure. Figure 26 displays T.P. Sims #2 dimple measurements. Dimples between 4.7 and 5.1 "ticks" suggesting a UCS of ~9000 to 10000 psi (62 to 68.9 MPa) (Figure 4).

2. Estimating the Coefficient of Sliding Friction (μ):
    a. Byerlee (1978) would suggest 0.85
    b. Zoback (2007) would suggest approximately 0.6
    c. Using UCS of 10000 psi (68.9 MPa) and Figure 22, a value of approximately 0.73 is obtained.
3. Stress estimation: Applying initializing information and premises to a Stress Polygon at 7700 feet TVD (Figure 27), a stress state of S_V = 19.4 ppg (7776 psi) (53.6 MPa), S_H = 19.1 ppg (7636 psi) (52.7 MPa), and S_h = 12.4 ppg (4964 psi) (34.2 MPa) is obtained.
4. Evaluate reactivation:
    a. Calculating normal stress (Sn) and shear stresses (Ss) (Table 9).
    b. Calculating reactivation pressure (P_{fr}) (Table 10).
5. Combining reactivating pressure and normal stresses (Table 11).

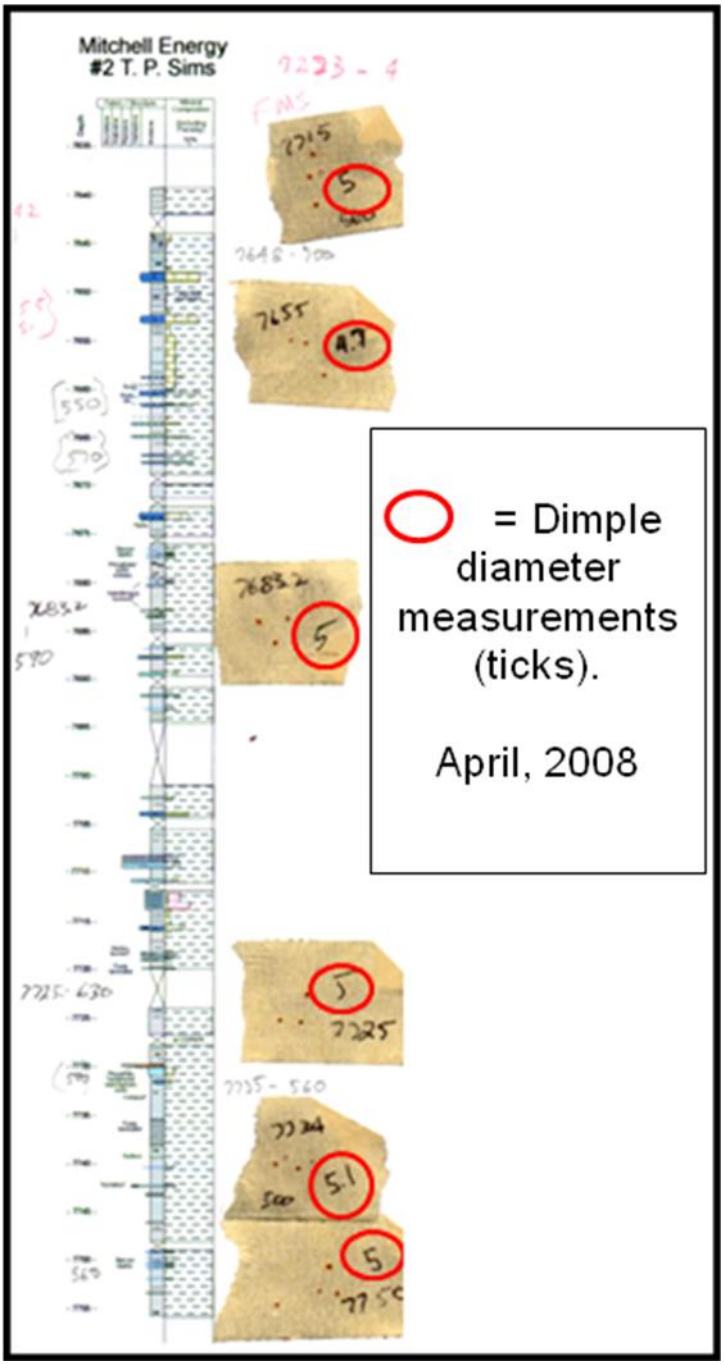

Figure 26. Dimpler measurements on the T. P. Sims #2 well. In the record above, dimples are the small red dots generally located to the left of large red circles which enclose the posted dimple diameter. The diameter of the dimples is measured with a surface magnifying glass scaled in "ticks." Field notes from Ruppel et al. (2008).

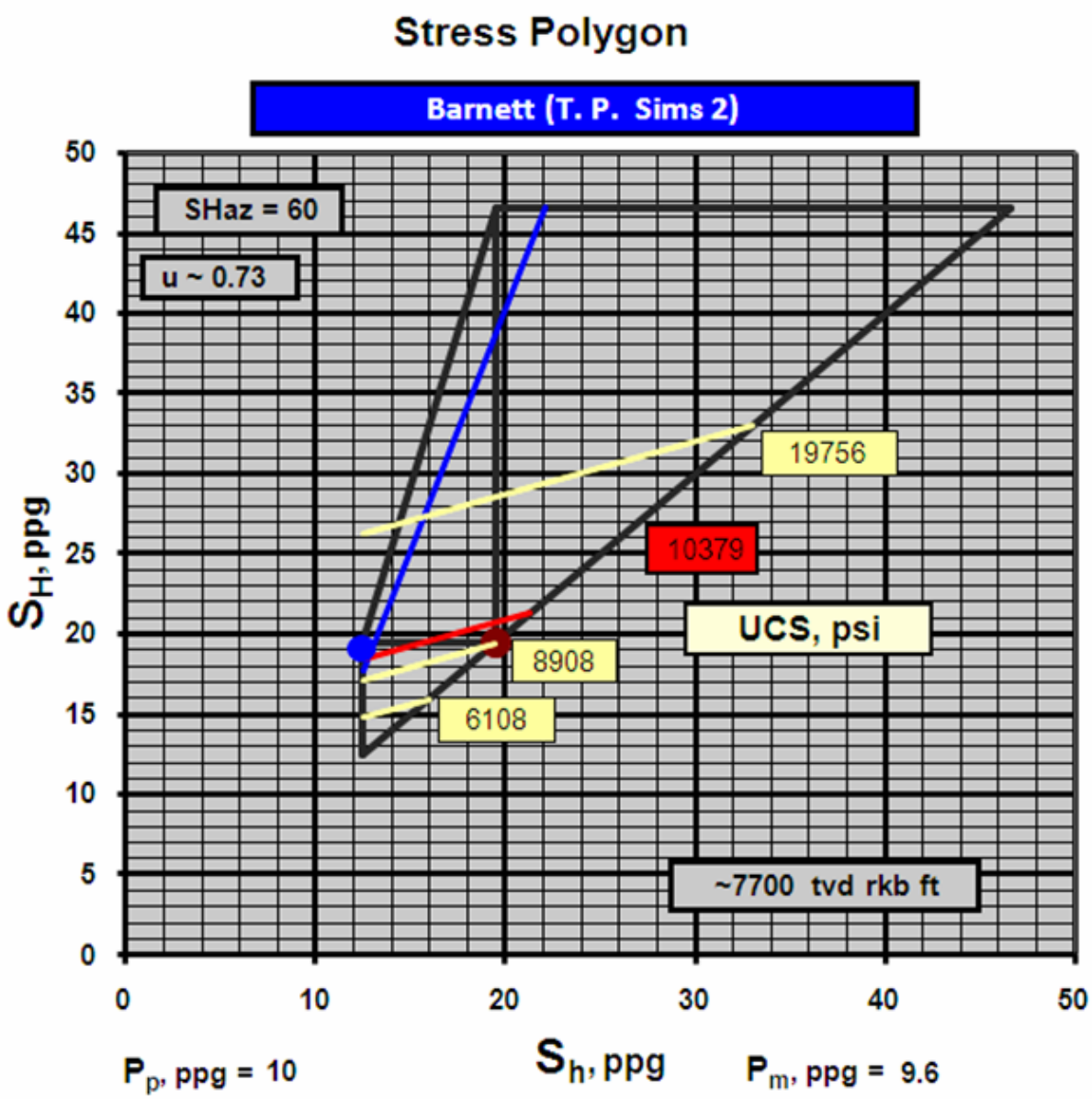

Figure 27. Stress Polygon for T. P. Sims #2 well.

DIP	Sn	Ss	Sn	Ss	Sn	Ss	Sn	Ss	Sn	Ss	Sn	Ss	Sn	Ss	DIP
85	6974	5155	6311	5337	5648	5168	5163	4704	4985	4244	5163	4704	5648	5168	85
75	7022	5136	6399	5342	5776	5239	5319	4922	5152	4703	5319	4922	5776	5239	75
65	7112	5093	6564	5336	6015	5332	5613	5176	5466	5077	5613	5176	6015	5332	65
55	7234	5021	6786	5296	6337	5383	6009	5353	5889	5321	6009	5353	6337	5383	55
45	7372	4912	7038	5199	6704	5349	6459	5399	6370	5406	6459	5399	6704	5349	45
35	7510	4765	7290	5034	7071	5206	6910	5295	6851	5321	6910	5295	7071	5206	35
25	7632	4579	7512	4799	7393	4956	7306	5047	7274	5077	7306	5047	7393	4956	25
DIP	Sn	Ss	Sn	Ss	Sn	Ss	Sn	Ss	Sn	Ss	Sn	Ss	Sn	Ss	DIP
Strike	0		15		30		45		60		75		90		Strike

DIP	Sn	Ss	Sn	Ss	Sn	Ss	Sn	Ss	Sn	Ss	Sn	Ss	Sn	Ss	DIP
85	5648	5168	6311	5337	6974	5155	7459	4666	7637	4012	7459	4666	6974	5155	85
75	5776	5239	6399	5342	7022	5136	7478	4650	7645	4035	7478	4650	7022	5136	75
65	6015	5332	6564	5336	7112	5093	7514	4618	7661	4054	7514	4618	7112	5093	65
55	6337	5383	6786	5296	7234	5021	7562	4567	7682	4066	7562	4567	7234	5021	55
45	6704	5349	7038	5199	7372	4912	7617	4499	7706	4070	7617	4499	7372	4912	45
35	7071	5206	7290	5034	7510	4765	7671	4411	7730	4066	7671	4411	7510	4765	35
25	7393	4956	7512	4799	7632	4579	7719	4308	7751	4054	7719	4308	7632	4579	25
DIP	Sn	Ss	Sn	Ss	Sn	Ss	Sn	Ss	Sn	Ss	Sn	Ss	Sn	Ss	DIP
Strike	90		105		120		135		150		165		180		Strike

Table 9. Normal and shear stresses (psi) acting on planes defined by dip and strike for T. P. Sims #2 well at 7700 feet (2346.9 m) TVD.

Dip	0	15	30	45	60	75	90	105	120	135	150	165	180	195	Strike	Dip
85	5392	4480	4048	4200	4652	4200	4048	4480	5392	6548	7620	6548	5392	4480	4048	85
75	5468	4560	4076	4056	4188	4056	4076	4560	5468	6588	7596	6588	5468	4560	4076	75
65	5616	4732	4192	4000	3992	4000	4192	4732	5616	6668	7588	6668	5616	4732	4192	65
55	5836	5012	4444	4156	4080	4156	4444	5012	5836	6784	7592	6784	5836	5012	4444	55
45	6124	5396	4856	4544	4444	4544	4856	5396	6124	6932	7612	6932	6124	5396	4856	45
35	6464	5876	5420	5136	5040	5136	5420	5876	6464	7108	7640	7108	6464	5876	5420	35
25	6840	6416	6084	5872	5800	5872	6084	6416	6840	7296	7676	7296	6840	6416	6084	25
0.73	0	15	30	45	60	75	90	105	120	135	150	165	180	195	210	Strike

Table 10. For the conditions Sv = 7776 psi (53.6 MPa), S_H = 7636 psi (52.7 MPa), and S_h = 4964 psi (34.2 MPa), the value within each cell (strike-dip combination) is the reactivation pressure (P_{fr} in psi) calculated using a coefficient of sliding friction of 0.73 (lower most left cell) and zero cohesion. Strike-dip combinations colored in yellow indicate that P_{fr} is less than S_h, whereas the blue strike-dip combinations indicate that P_{fr} is above S_h. The gold colored cell with red text is the lowest value presented.

	= Bottom 30%															Lowest
Dip	0	15	30	45	60	75	90	105	120	135	150	165	180	195	Strike	Dip
85	2183	1396	848	682	819	682	848	1396	2183	3004	3629	3004	2183	1396	848	85
75	2245	1480	926	688	670	688	926	1480	2245	3033	3621	3033	2245	1480	926	75
65	2364	1648	1104	807	729	807	1104	1648	2364	3091	3625	3091	2364	1648	1104	65
55	2535	1899	1391	1083	985	1083	1391	1899	2535	3173	3637	3173	2535	1899	1391	55
45	2748	2217	1780	1502	1407	1502	1780	2217	2748	3275	3659	3275	2748	2217	1780	45
35	2987	2583	2246	2023	1946	2023	2246	2583	2987	3390	3685	3390	2987	2583	2246	35
25	3236	2964	2739	2589	2537	2589	2739	2964	3236	3508	3714	3508	3236	2964	2739	25
	0	15	30	45	60	75	90	105	120	135	150	165	180	195	210	Strike

Table 11. Results of taking the average of effective reactivation stress and the effective normal stress derived from T.P. Sims #2 stress state.

Fracture Summary

Table 12 is a summary of Tables 9, 10, and 11 for the reported natural fracture set in the Barnett Shale that strike of 105° and dip of 74° (red ellipses). The estimated normal stress is 6399 psi (44.1 MPa), the reactivation pressure is 4560 psi (31.4 MPa) and the average of the effective reactivation pressure and the effective normal stresses is 1480 psi (10.2 MPa).

Discussion: Interactions of Hydraulic Fracture Treatment with Natural Fractures

Considering the T.P. Sims #2 stress situation and known natural fractures striking 105° and dipping at approximately 75°, the estimated reactivation pressure is 4560 psi (31.4 MPa). Such pressure is probably out of reach for most natural processes within the "oil field time frame" (last few decades). However, this pressure is easily reached during hydraulic fracturing operation (see Table 10, yellow colored cells), since the typical down-hole treating pressure is equal to the sum of S_h (estimated at approximately 5000 psi or 34.5 MPa) and the net pressure (net pressure approximately 1000 psi or 6.9 MPa; Lancaster et al., 1992). Such reactivation can act to divert the fracturing fluids from the expected linear-elastic Mode I direction of 60° (S_{Haz}) to 105°. Since the orientation of the natural fracture is close to the yellow–blue transition on Table 10, it can be easily imagined that a complicated "switching" back and forth between 60° and 105° exists thereby creating a relatively wide corridor of a complex fracture network compared to that of a linear-elastic Mode I fracture with a general orientation of approximately 60°.

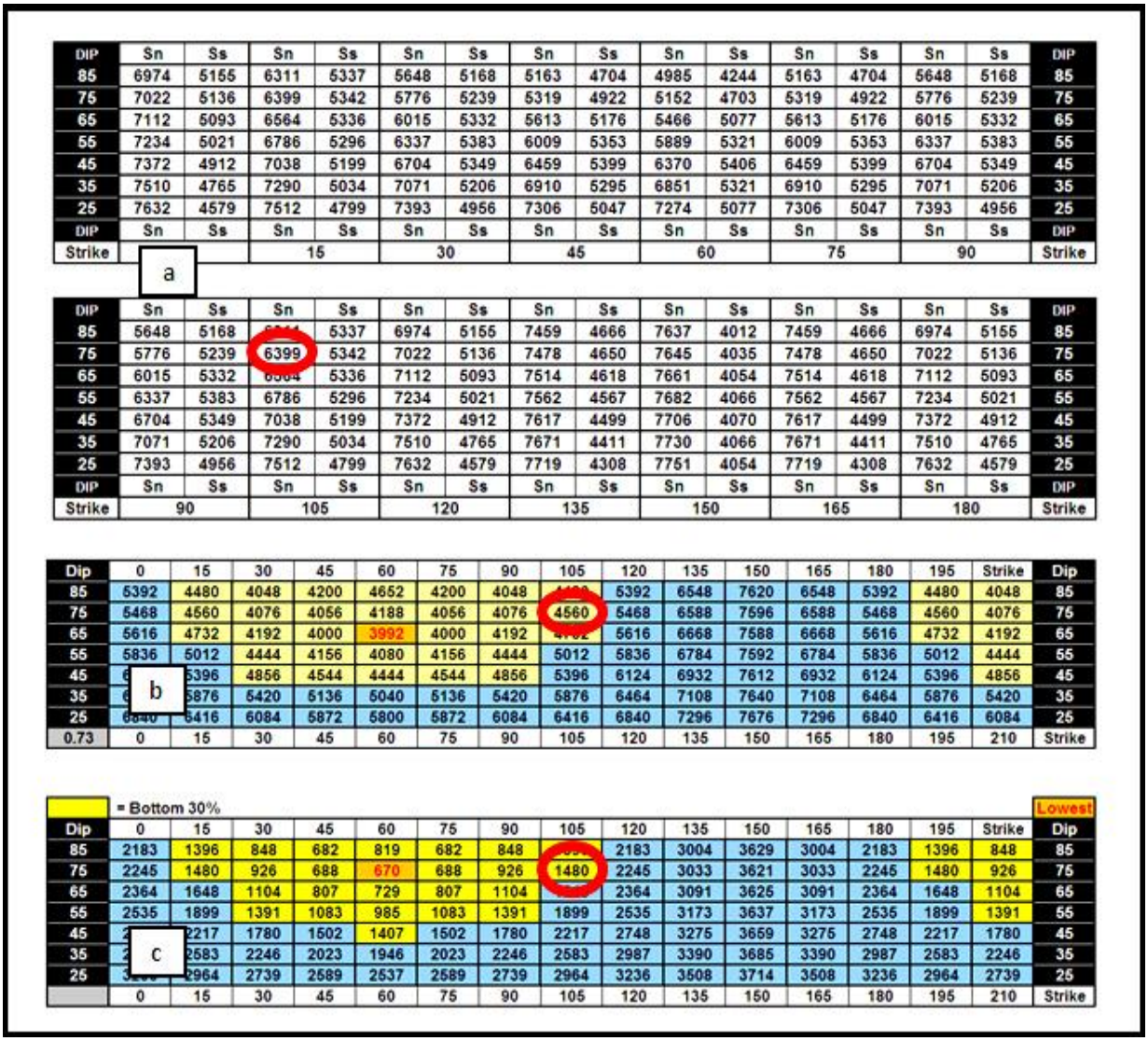

DIP	Sn	Ss	Sn	Ss	Sn	Ss	Sn	Ss	Sn	Ss	Sn	Ss	Sn	Ss	DIP
85	6974	5155	6311	5337	5648	5168	5163	4704	4985	4244	5163	4704	5648	5168	85
75	7022	5136	6399	5342	5776	5239	5319	4922	5152	4703	5319	4922	5776	5239	75
65	7112	5093	6564	5336	6015	5332	5613	5176	5466	5077	5613	5176	6015	5332	65
55	7234	5021	6786	5296	6337	5383	6009	5353	5889	5321	6009	5353	6337	5383	55
45	7372	4912	7038	5199	6704	5349	6459	5399	6370	5406	6459	5399	6704	5349	45
35	7510	4765	7290	5034	7071	5206	6910	5295	6851	5321	6910	5295	7071	5206	35
25	7632	4579	7512	4799	7393	4956	7306	5047	7274	5077	7306	5047	7393	4956	25
DIP	Sn	Ss	Sn	Ss	Sn	Ss	Sn	Ss	Sn	Ss	Sn	Ss	Sn	Ss	DIP
Strike			15		30		45		60		75		90		Strike

a

DIP	Sn	Ss	Sn	Ss	Sn	Ss	Sn	Ss	Sn	Ss	Sn	Ss	Sn	Ss	DIP
85	5648	5168	[illegible]	5337	6974	5155	7459	4666	7637	4012	7459	4666	6974	5155	85
75	5776	5239	6399	5342	7022	5136	7478	4650	7645	4035	7478	4650	7022	5136	75
65	6015	5332	[illegible]	5336	7112	5093	7514	4618	7661	4054	7514	4618	7112	5093	65
55	6337	5383	6786	5296	7234	5021	7562	4567	7682	4066	7562	4567	7234	5021	55
45	6704	5349	7038	5199	7372	4912	7617	4499	7706	4070	7617	4499	7372	4912	45
35	7071	5206	7290	5034	7510	4765	7671	4411	7730	4066	7671	4411	7510	4765	35
25	7393	4956	7512	4799	7632	4579	7719	4308	7751	4054	7719	4308	7632	4579	25
DIP	Sn	Ss	Sn	Ss	Sn	Ss	Sn	Ss	Sn	Ss	Sn	Ss	Sn	Ss	DIP
Strike	90		105		120		135		150		165		180		Strike

Dip	0	15	30	45	60	75	90	105	120	135	150	165	180	195	Strike	Dip
85	5392	4480	4048	4200	4652	4200	4048	[illegible]	5392	6548	7620	6548	5392	4480	4048	85
75	5468	4560	4076	4056	4188	4056	4076	4560	5468	6588	7596	6588	5468	4560	4076	75
65	5616	4732	4192	4000	3992	4000	4192	[illegible]	5616	6668	7588	6668	5616	4732	4192	65
55	5836	5012	4444	4156	4080	4156	4444	5012	5836	6784	7592	6784	5836	5012	4444	55
45	6	5396	4856	4544	4444	4544	4856	5396	6124	6932	7612	6932	6124	5396	4856	45
35	6	5876	5420	5136	5040	5136	5420	5876	6464	7108	7640	7108	6464	5876	5420	35
25	6840	6416	6084	5872	5800	5872	6084	6416	6840	7296	7676	7296	6840	6416	6084	25
0.73	0	15	30	45	60	75	90	105	120	135	150	165	180	195	210	Strike

b

	= Bottom 30%															Lowest
Dip	0	15	30	45	60	75	90	105	120	135	150	165	180	195	Strike	Dip
85	2183	1396	848	682	819	682	848	[illegible]	2183	3004	3629	3004	2183	1396	848	85
75	2245	1480	926	688	670	688	926	1480	2245	3033	3621	3033	2245	1480	926	75
65	2364	1648	1104	807	729	807	1104	[illegible]	2364	3091	3625	3091	2364	1648	1104	65
55	2535	1899	1391	1083	985	1083	1391	1899	2535	3173	3637	3173	2535	1899	1391	55
45	2	2217	1780	1502	1407	1502	1780	2217	2748	3275	3659	3275	2748	2217	1780	45
35	2	2583	2246	2023	1946	2023	2246	2583	2987	3390	3685	3390	2987	2583	2246	35
25	3	2964	2739	2589	2537	2589	2739	2964	3236	3508	3714	3508	3236	2964	2739	25
	0	15	30	45	60	75	90	105	120	135	150	165	180	195	210	Strike

c

Table 12. For the reported natural fractures from the T. P. Sims #2 well with a strike of 105° and a dip 74° (red ellipses) the estimated normal stress is 6399 psi (44.1 MPa) (a. Table 9), the reactivation pressure is 4560 psi (31.4 MPa) (b. Table 10), and the average of the effective reactivation pressure and the effective normal stresses is 1480 psi (10.2 MPa) (c. Table 11).

CONCLUSIONS

1. Laboratory experiment and field observations indicate that fractures can be reactivated and fail in shear. Such shear failure results in movement along the surface, subsequently increases the ability of fluid to flow.
2. The method presented provides a means to quantitatively evaluate both shear and normal stresses acting on a fracture.
3. The method presented provides a means to quantitatively evaluate the fracture reactivation pressure.
4. Traditional "closure pressure" may or may not be equivalent in value to the minimum horizontal stress (S_h).
5. The presented method provides insight into the interaction of hydraulic fracture treatments with the reactivation of natural fractures in low permeability reservoirs.

REFERENCES

Aguilera, R., 1980, Naturally Fractured Reservoirs. The Petroleum Publishing Company, 703 p.

Anderson, E.M., 1951, Dynamics of Faulting and Dike Formation With Application in Britain: Oliver and Boyd, Edinburgh, 206 p.

Bandis, S.C., Lumsden, A.C., and Barton, N.R., 1983, Fundamentals of rock joint deformation: Int. J. Rock Mech. Min. Sci. & Geomech., v. 20, no. 6, p. 249-268.

Barton, C.A., Zoback, M.D., and Moos, D., 1995, Fluid flow along potentially active faults in crystalline rock: Geology, v. 23, p. 683-686.

Barton, N., Bandis, S.C., and Bakhtar, K., 1985, Strength, deformation and conductivity coupling of rock joints: Int. J. Rock Mech. Min. Sci. & Geomech., v. 22, no. 3, p. 121-140.

Byerlee, J.D., 1978, Friction of Rocks: Pure & Applied Geophysics, v. 116, p. 615-626.

Committee on Fracture Characterization and Fluid Flow, National Research Council, 1996, Rock Fractures and Fluid Flow: Contemporary Understanding and Applications Committee on Fracture Characterization and Fluid Flow, 586 p.

Couzens-Schultz, B.A. and Chan, A.W., 2010, An Alternative Leak-off Pressure Interpretation: Journal of Structure Geology, v. 6, no. 13.

Cumella, S.P., and Scheevel, J., 2008, The influence of stratigraphy and rock mechanics on Mesaverde gas distribution, Pieance basin, Colorado: AAGP Hedberg Series, No. 3, Understanding, exploring, and developing tight-gas sands, p. 137-155.

Eaton, B.A., 1969, Fracture gradient prediction and its application in oilfield operations: Journal of Petroleum Technology, n. 246, p. 1353-1360.

Engelder, T., Geiser, P.A., and Alvarec, W., 1981, Role of pressure solution and dissolution in geology: Penrose Conference Report, Geology, v. 9, p. 44-45.

Gale, J.F.W., Reed, R.M., and Holder, J., 2007, Natural fractures in the Barnett Shale and their importance for hydraulic fracture treatments: AAPG Bulletin, v. 91 no. 4, p. 603-622.

Gidley, J.L., Holditch, S.A., Nierode, D.E., and Veatch, R.W., 1989, Recent advances in hydraulic fracturing: Society of Petroleum Engineers, monograph v. 12, 452 p.

Goodman, R.E., 1989, Introduction to rock mechanics: John Wiley & son, New York, 220p.

Gretner, P.E., 1981, Pore pressure: Fundamentals, general ramifications, and implication for structural geology (revised): AAPG Education Course Notes 4, 131p.

Gutierrez, M., Oino, L.E., and Nygard, R., 2000, Stress-dependent permeability of a de-mineralised fracture in shale: Marine and Petroleum Geology v. 17, p. 895-907.

Halliburton, 1978, Halliburton Cementing Tables: Halliburton, Duncan, OK, 240 p.

Jaeger, J.C., and Cook, N.G., 1979, Fundamentals of rock mechanics, Chapman and Hall, New York, 585 p.

Kent, W., 1899, Mechanical Engineer's Pocket-Book: John Wiley & Sons, New York, 1119 p.

Kirsch, G., 1898, Die Theorie der Elastizität und die Bedürfnisse der Festigkeitslehre: Zeitschrift des Vereines Deutscher Ingenieure, v. 42, p. 797-807.

Lancaster, D.E., McKetta, S.F., Hill, R.E., Guidry, F.K., and Jochen, J.E., 1992, Reservoir evaluation, completion techniques, and recent results from Barnett Shale development in the Fort Worth Basin: SPE 24884.

Laubach, S.E., Olson, J.O., Gale, J.F.W., 2004, Are open fractures necessarily aligned with maximum horizontal stress?: Earth and Planetary Science Letters, v. 222, p. 191-195.

Levorsen, A.I., 1967, Geology of Petroleum. W.H. Freeman and Company, San Francisco, 724 p.

Loucks, R.D., and Ruppel, S.J., 2007, Mississippian Barnett Shale: Lithofacies and depositional setting of a deep-water shale-gas succession in the Fort Worth Basin, Texas: AAPG Bulletin, v. 91 no. 4, p. 579-601.

Moos, D., 2007, Constraints on in situ stresses from strength of materials. SPE/AAPG/SEG Workshop on Integrating Stresses and Pore Pressure Predictions for Exploration, Drilling, and Production, Galveston, TX.

Moos, D. and Zoback, M.D., 1990, Utilization of observation of well bore failure to constrain the orientation and magnitude of crustal stresses: application to continental deep sea drilling project and ocean drilling program boreholes: J. Geophys. Res. v. 95, p. 9305-9325.

Olsson, W.A., 1992, The effect of slip on the flow of fluids through a fracture. Geophysical Research Letters, v. 19. no. 6, p.5 41-543

Ostensen, R.W., 1983, Microcracks Permeability in Tight Gas Sandstones: SPE Journal, v. 23, no. 6, p. 919-927.

Plumb, R.A. and Hickman, S.H., 1985, Stress-induced borehole elongation: A comparison between the four-arm dipmeter and the borehole televiever in the Auburn geothermal well: J. Geophys. Res. v. 90, p. 5513-5521.

Ramos, G.G., Chin, L.Y., Enderlin, M.B., 2008, Up-scaling of Rock Mechanical and Petrophysical Properties from Grain Scale to Log Scale by Point-Stress and Wedge Indentation Tests. 42nd U.S. Rock Mechanics Symposium, San Francisco, California. U.S.A.

Ruppel, S.C., Loucks, R.G., and Gale, J.F.W., 2008, Barnett, Woodford, and Related Mudrocks Succession in Texas Core and Outcrop: Bureau of Economic Geology, Jackson School of Geosciences, University of Texas at Austin.

Schlumberger, 1972, Log interpretation: Volume I – Principles: Schlumberger Limited, New York, 113 p.

Terzaghi, K., 1943, Theoretical soil mechanics: John Wiley, New York.

Tolman, C.F., 1937, Ground Water: McGraw-Hill, New York, 593 p.

Van der Pluijm, B.A., and Marshak, S., 2004, Earth Structure: an introduction to structural geology and tectonics: W. W. Norton & Company, Inc., 656 p.

Warpinski, N.R. 2009, Integrating Microseismic Monitoring With Well completions Reservoir Behavior, and Rock Mechanics: SPE 125239, SPE Tight Gas Completions Conference, San Antonio, TX, 15-17 June 2009.

Weingarten, J.S. and Perkins, T.K., 1995, Prediction of sand production in gas wells: methods and Gulf of Mexico case studies: SPE 24797.

Zoback, M.D., 2007, Reservoir Geomechanics: Cambridge University Press, 449 p.

APPENDICES

Appendix 1: Flow data plots for each hour between hour 19 and 34.

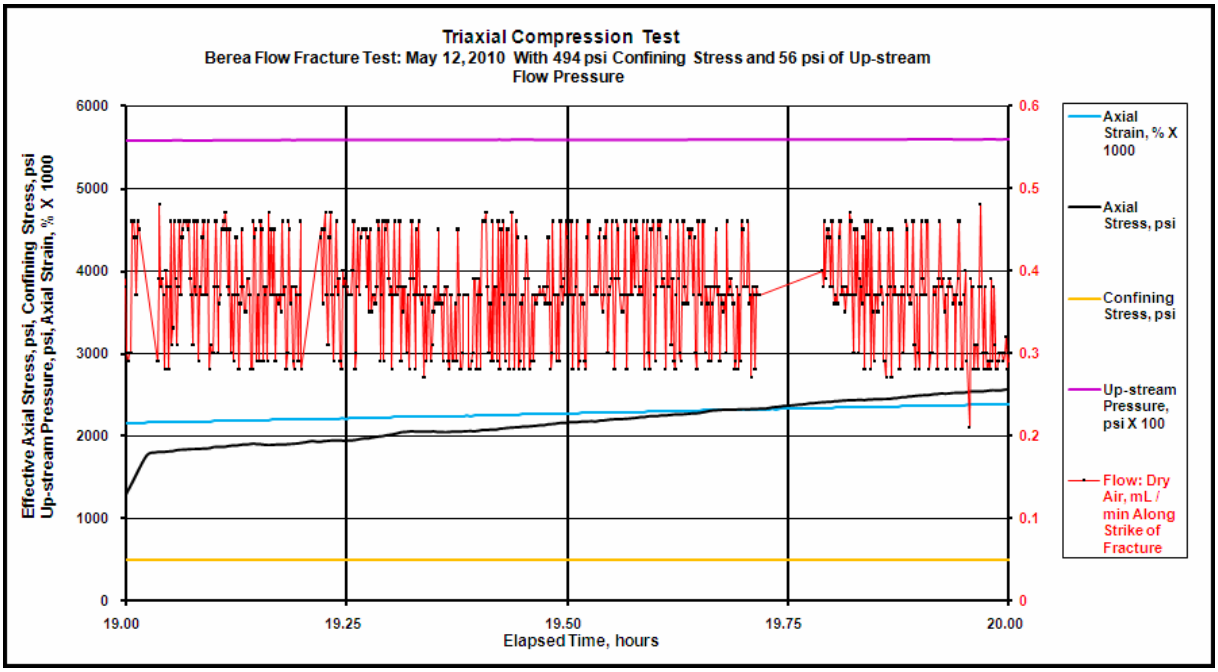

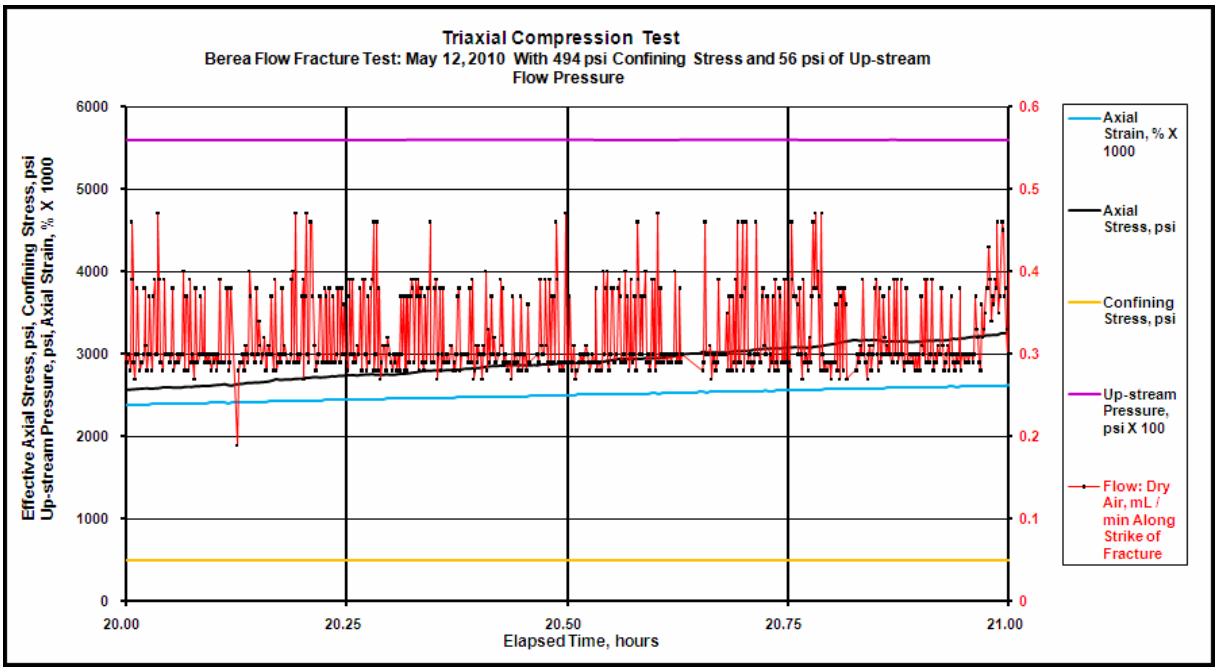

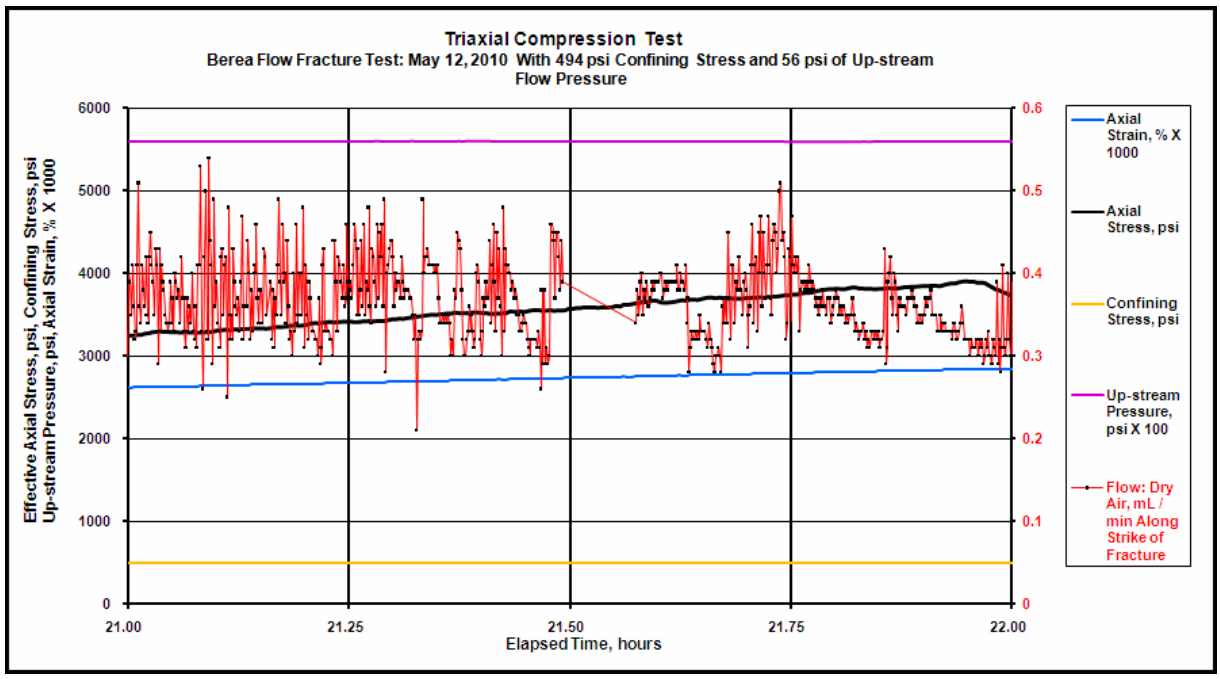
Triaxial Compression Test
Berea Flow Fracture Test: May 12, 2010 With 494 psi Confining Stress and 56 psi of Up-stream Flow Pressure
Effective Axial Stress, psi, Confining Stress, psi Up-stream Pressure, psi, Axial Strain, % X 1000
Elapsed Time, hours
Axial Strain, % X 1000
Axial Stress, psi
Confining Stress, psi
Up-stream Pressure, psi X 100
Flow: Dry Air, mL / min Along Strike of Fracture

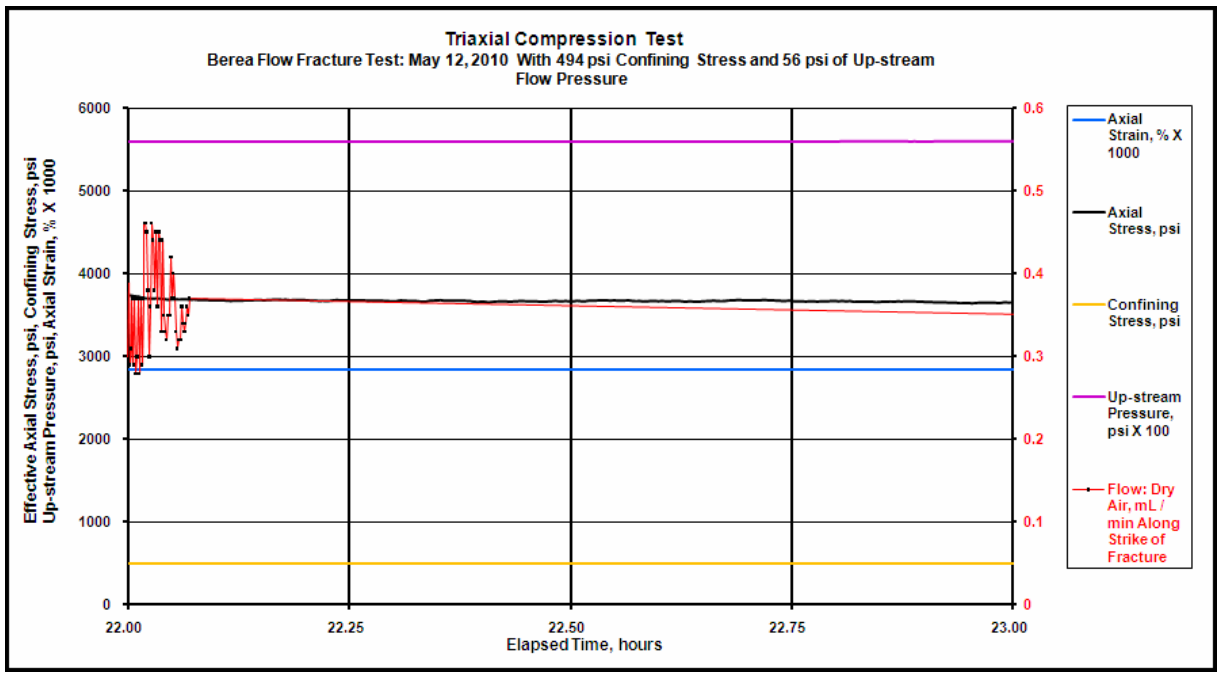
Triaxial Compression Test
Berea Flow Fracture Test: May 12, 2010 With 494 psi Confining Stress and 56 psi of Up-stream Flow Pressure
Effective Axial Stress, psi, Confining Stress, psi Up-stream Pressure, psi, Axial Strain, % X 1000
Elapsed Time, hours
Axial Strain, % X 1000
Axial Stress, psi
Confining Stress, psi
Up-stream Pressure, psi X 100
Flow: Dry Air, mL / min Along Strike of Fracture

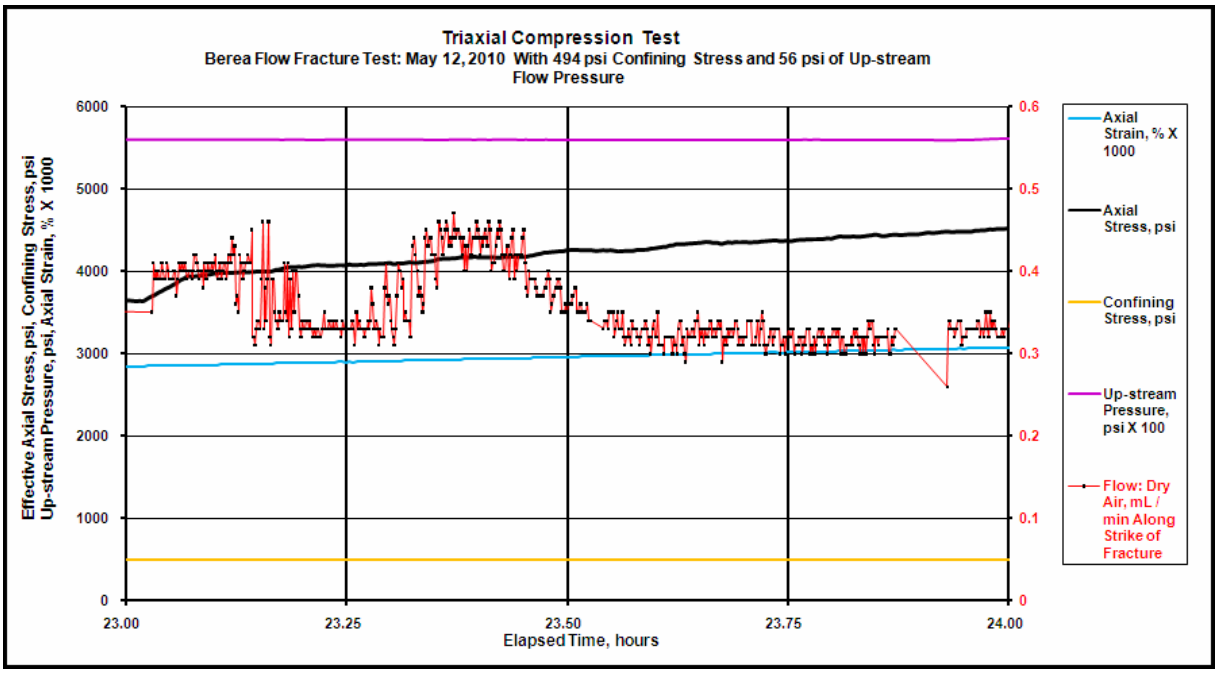
Triaxial Compression Test
Berea Flow Fracture Test: May 12, 2010 With 494 psi Confining Stress and 56 psi of Up-stream Flow Pressure
Effective Axial Stress, psi, Confining Stress, psi
Up-stream Pressure, psi, Axial Strain, % X 1000
6000
5000
4000
3000
2000
1000
0
0.6
0.5
0.4
0.3
0.2
0.1
0
23.00
23.25
23.50
23.75
24.00
Elapsed Time, hours
Axial Strain, % X 1000
Axial Stress, psi
Confining Stress, psi
Up-stream Pressure, psi X 100
Flow: Dry Air, mL / min Along Strike of Fracture

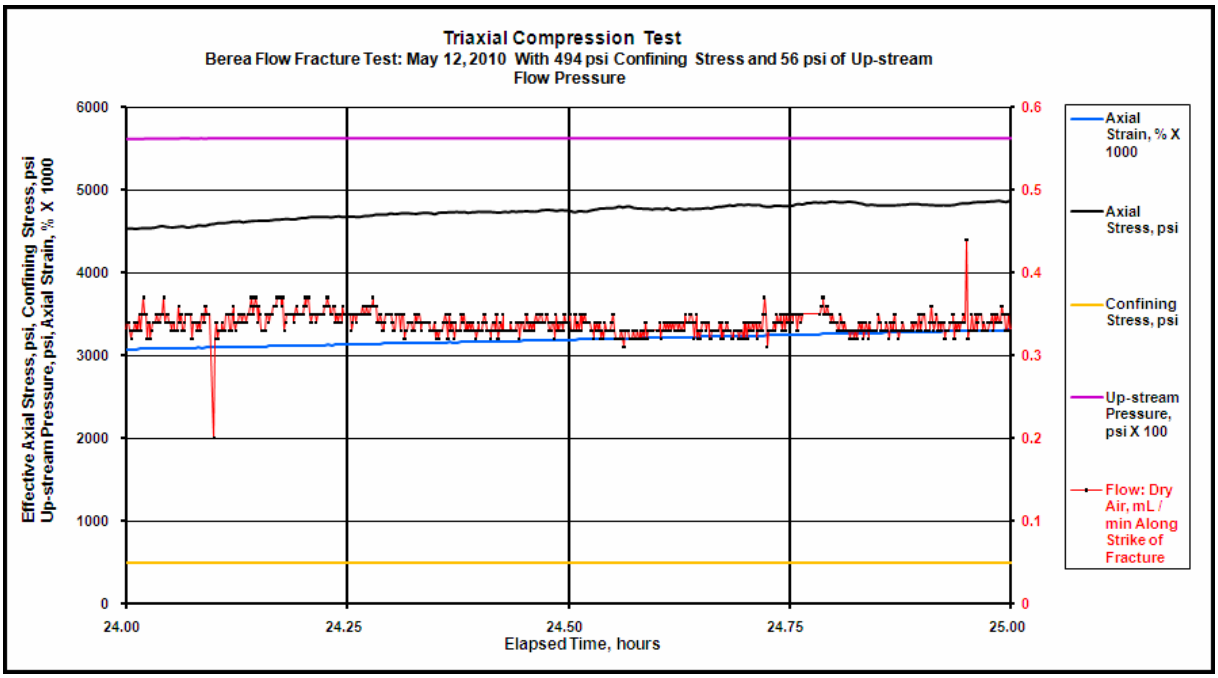
Triaxial Compression Test
Berea Flow Fracture Test: May 12, 2010 With 494 psi Confining Stress and 56 psi of Up-stream Flow Pressure
Effective Axial Stress, psi, Confining Stress, psi
Up-stream Pressure, psi, Axial Strain, % X 1000
6000
5000
4000
3000
2000
1000
0
0.6
0.5
0.4
0.3
0.2
0.1
0
24.00
24.25
24.50
24.75
25.00
Elapsed Time, hours
Axial Strain, % X 1000
Axial Stress, psi
Confining Stress, psi
Up-stream Pressure, psi X 100
Flow: Dry Air, mL / min Along Strike of Fracture

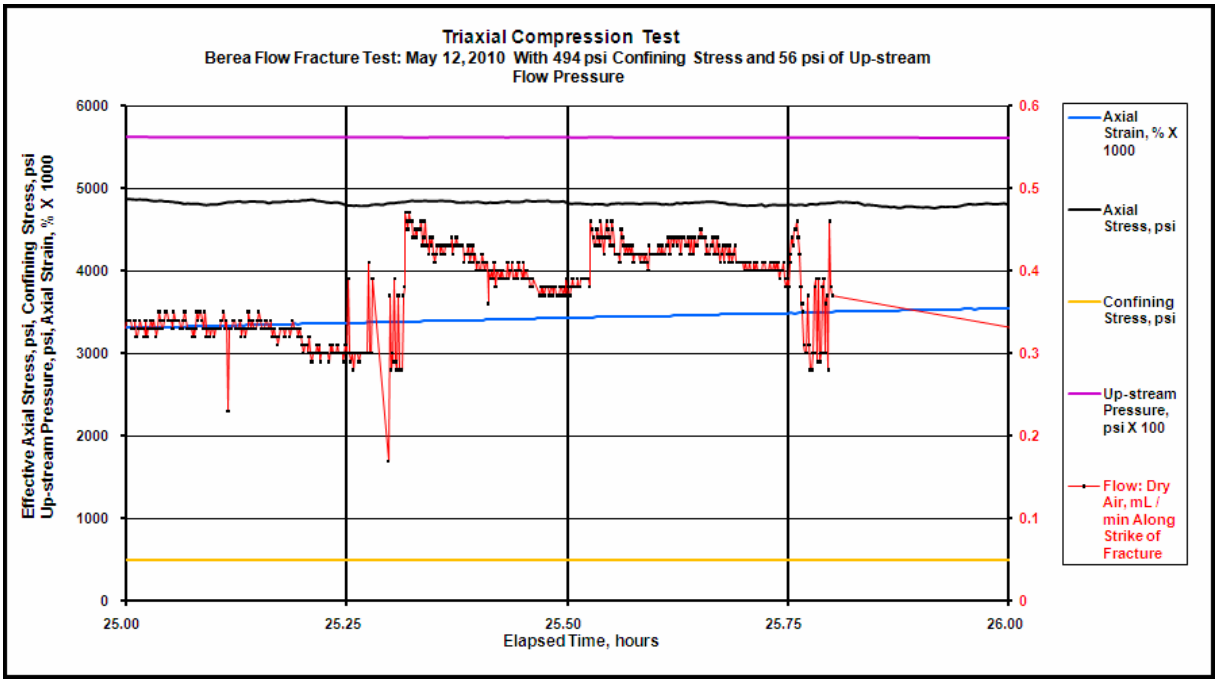
Triaxial Compression Test
Berea Flow Fracture Test: May 12, 2010 With 494 psi Confining Stress and 56 psi of Up-stream Flow Pressure
Effective Axial Stress, psi, Confining Stress, psi
Up-stream Pressure, psi, Axial Strain, % X 1000
6000
5000
4000
3000
2000
1000
0
0.6
0.5
0.4
0.3
0.2
0.1
0
25.00
25.25
25.50
25.75
26.00
Elapsed Time, hours
Axial Strain, % X 1000
Axial Stress, psi
Confining Stress, psi
Up-stream Pressure, psi X 100
Flow: Dry Air, mL / min Along Strike of Fracture

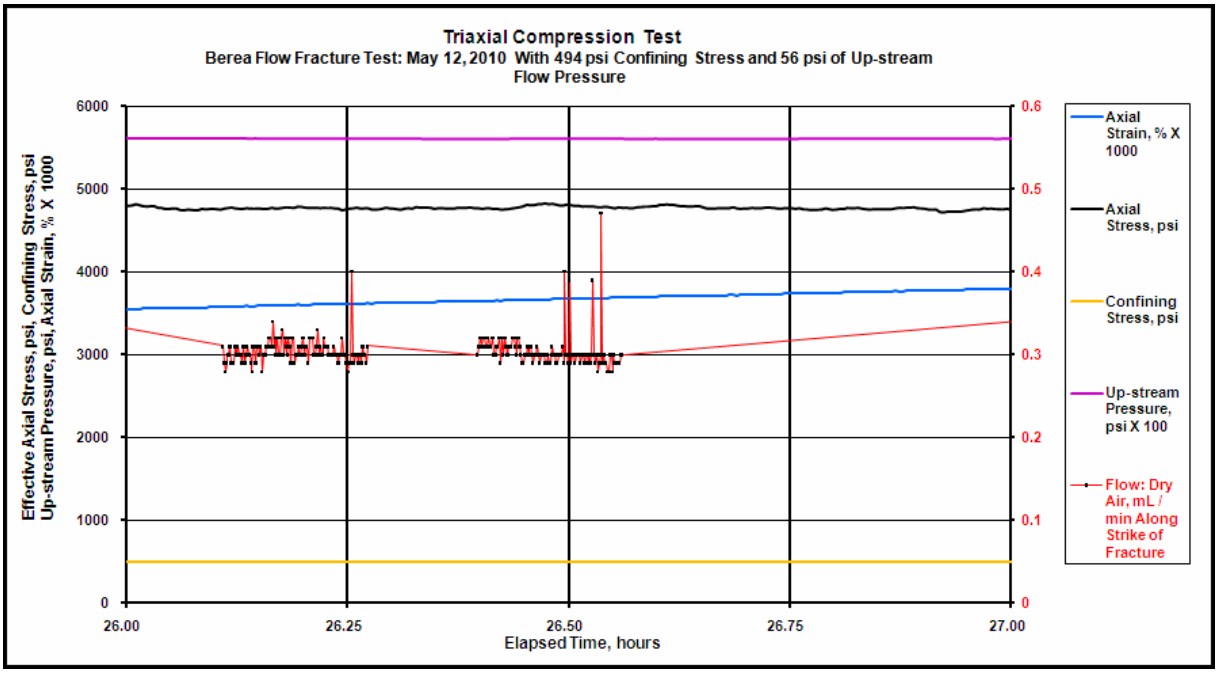
Triaxial Compression Test
Berea Flow Fracture Test: May 12, 2010 With 494 psi Confining Stress and 56 psi of Up-stream Flow Pressure
Effective Axial Stress, psi, Confining Stress, psi
Up-stream Pressure, psi, Axial Strain, % X 1000
6000
5000
4000
3000
2000
1000
0
0.6
0.5
0.4
0.3
0.2
0.1
0
26.00
26.25
26.50
26.75
27.00
Elapsed Time, hours
Axial Strain, % X 1000
Axial Stress, psi
Confining Stress, psi
Up-stream Pressure, psi X 100
Flow: Dry Air, mL / min Along Strike of Fracture

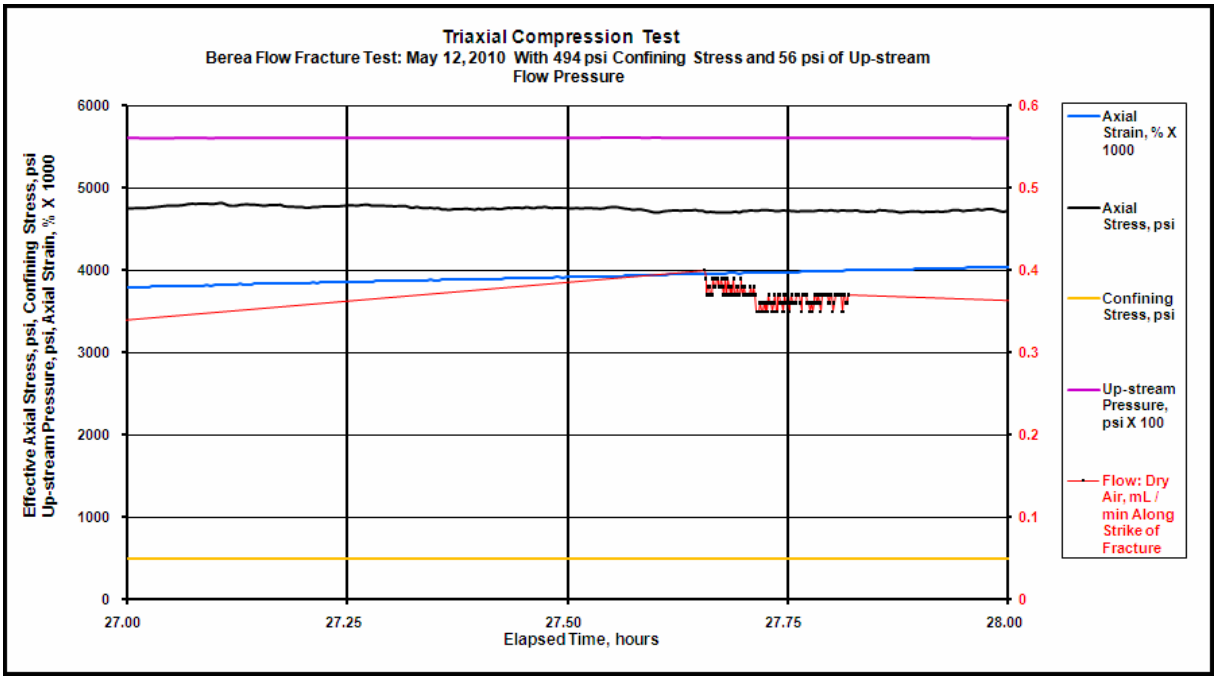
Triaxial Compression Test
Berea Flow Fracture Test: May 12, 2010 With 494 psi Confining Stress and 56 psi of Up-stream Flow Pressure
Effective Axial Stress, psi, Confining Stress, psi
Up-stream Pressure, psi, Axial Strain, % X 1000
6000
5000
4000
3000
2000
1000
0
0.6
0.5
0.4
0.3
0.2
0.1
0
27.00
27.25
27.50
27.75
28.00
Elapsed Time, hours
Axial Strain, % X 1000
Axial Stress, psi
Confining Stress, psi
Up-stream Pressure, psi X 100
Flow: Dry Air, mL / min Along Strike of Fracture

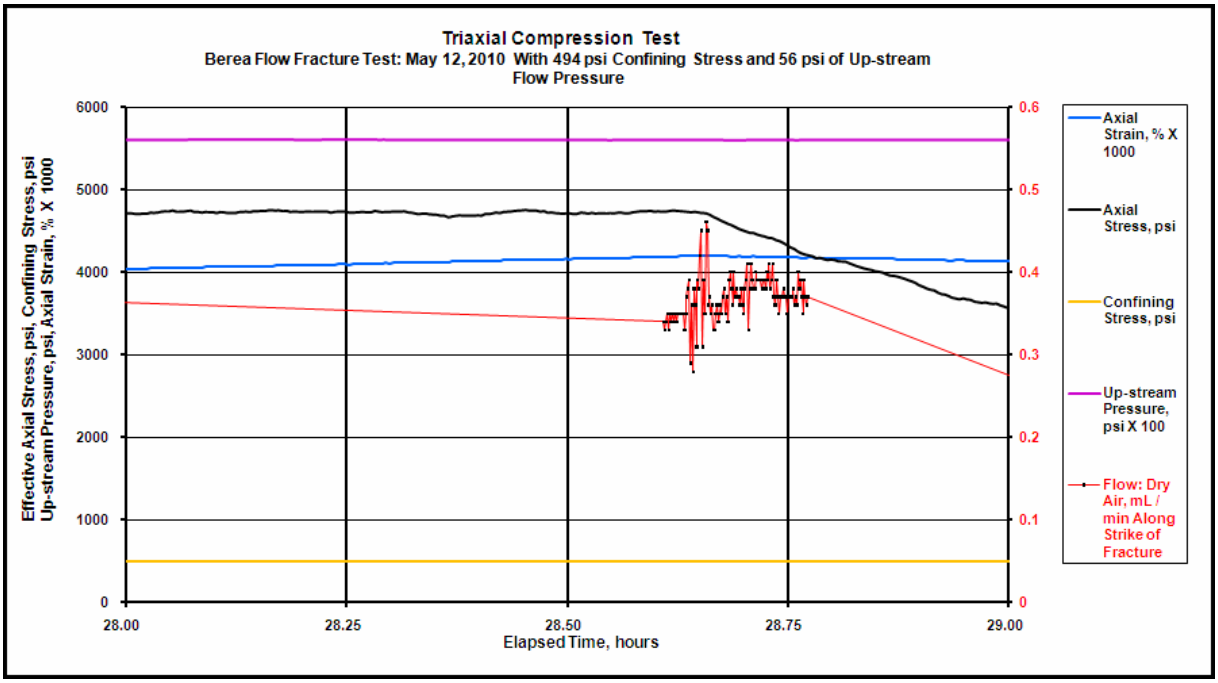
Triaxial Compression Test
Berea Flow Fracture Test: May 12, 2010 With 494 psi Confining Stress and 56 psi of Up-stream Flow Pressure
Effective Axial Stress, psi, Confining Stress, psi
Up-stream Pressure, psi, Axial Strain, % X 1000
6000
5000
4000
3000
2000
1000
0
0.6
0.5
0.4
0.3
0.2
0.1
0
28.00
28.25
28.50
28.75
29.00
Elapsed Time, hours
Axial Strain, % X 1000
Axial Stress, psi
Confining Stress, psi
Up-stream Pressure, psi X 100
Flow: Dry Air, mL / min Along Strike of Fracture

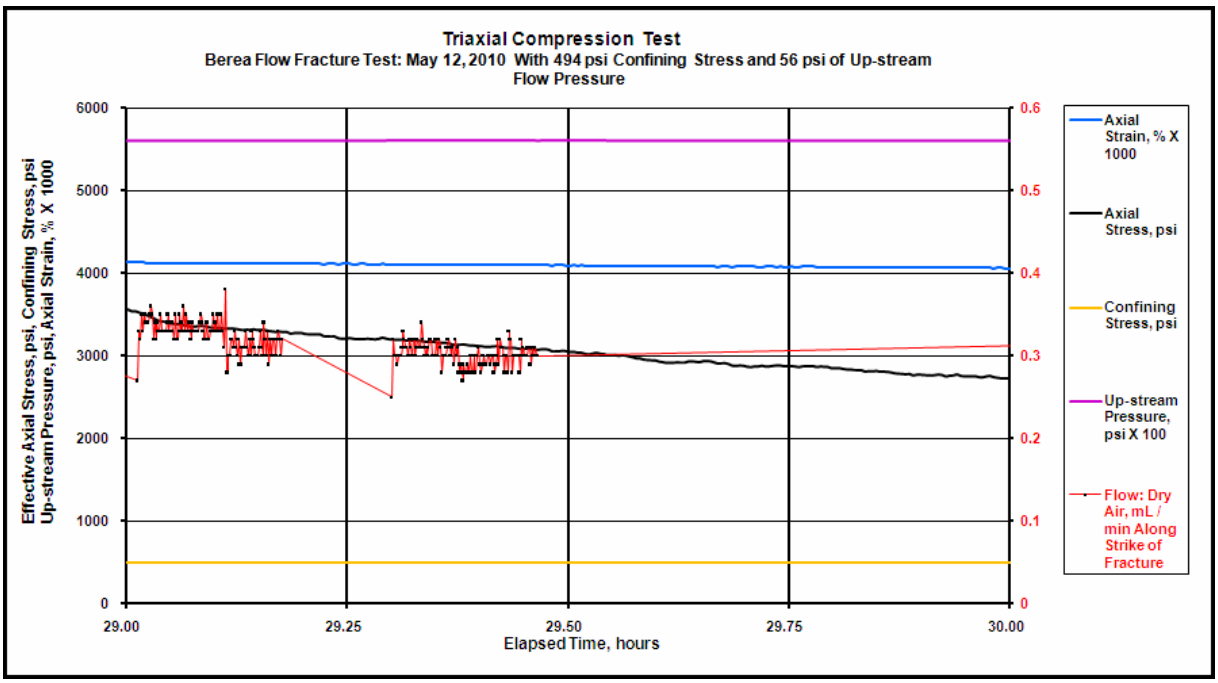
Triaxial Compression Test
Berea Flow Fracture Test: May 12, 2010 With 494 psi Confining Stress and 56 psi of Up-stream Flow Pressure
Effective Axial Stress, psi, Confining Stress, psi
Up-stream Pressure, psi, Axial Strain, % X 1000
6000
5000
4000
3000
2000
1000
0
0.6
0.5
0.4
0.3
0.2
0.1
0
29.00
29.25
29.50
29.75
30.00
Elapsed Time, hours
Axial Strain, % X 1000
Axial Stress, psi
Confining Stress, psi
Up-stream Pressure, psi X 100
Flow: Dry Air, mL / min Along Strike of Fracture

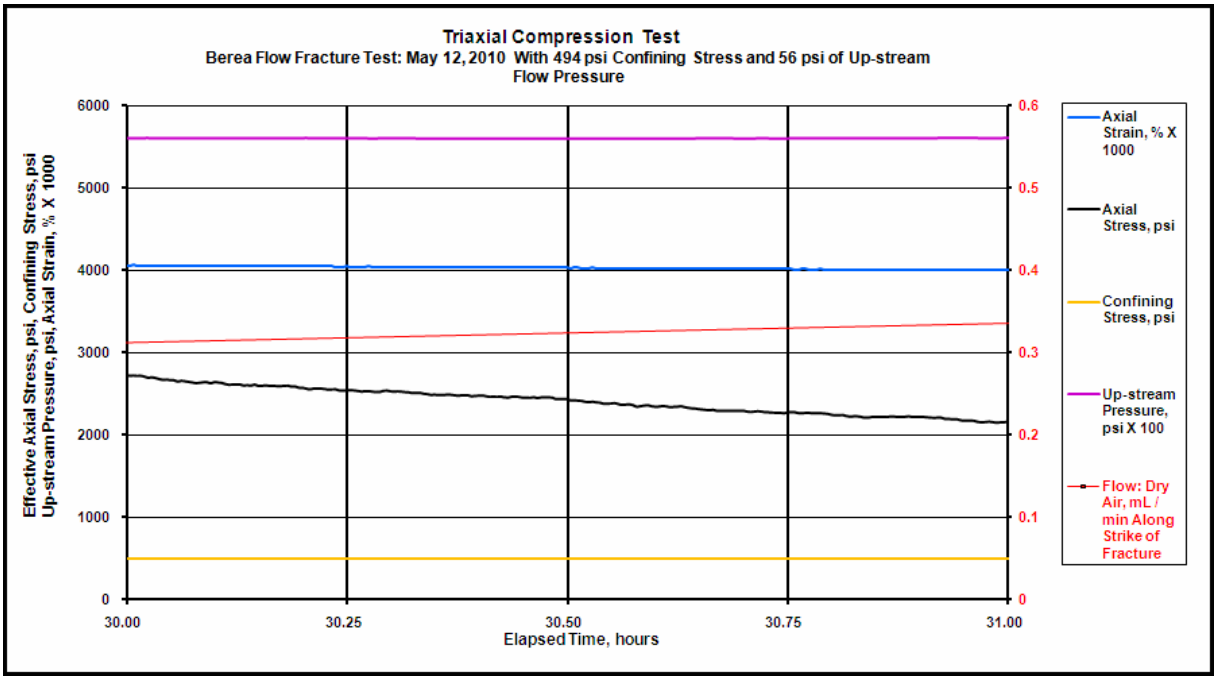
Triaxial Compression Test
Berea Flow Fracture Test: May 12, 2010 With 494 psi Confining Stress and 56 psi of Up-stream Flow Pressure
Effective Axial Stress, psi, Confining Stress, psi
Up-stream Pressure, psi, Axial Strain, % X 1000
6000
5000
4000
3000
2000
1000
0
0.6
0.5
0.4
0.3
0.2
0.1
0
30.00
30.25
30.50
30.75
31.00
Elapsed Time, hours
Axial Strain, % X 1000
Axial Stress, psi
Confining Stress, psi
Up-stream Pressure, psi X 100
Flow: Dry Air, mL / min Along Strike of Fracture

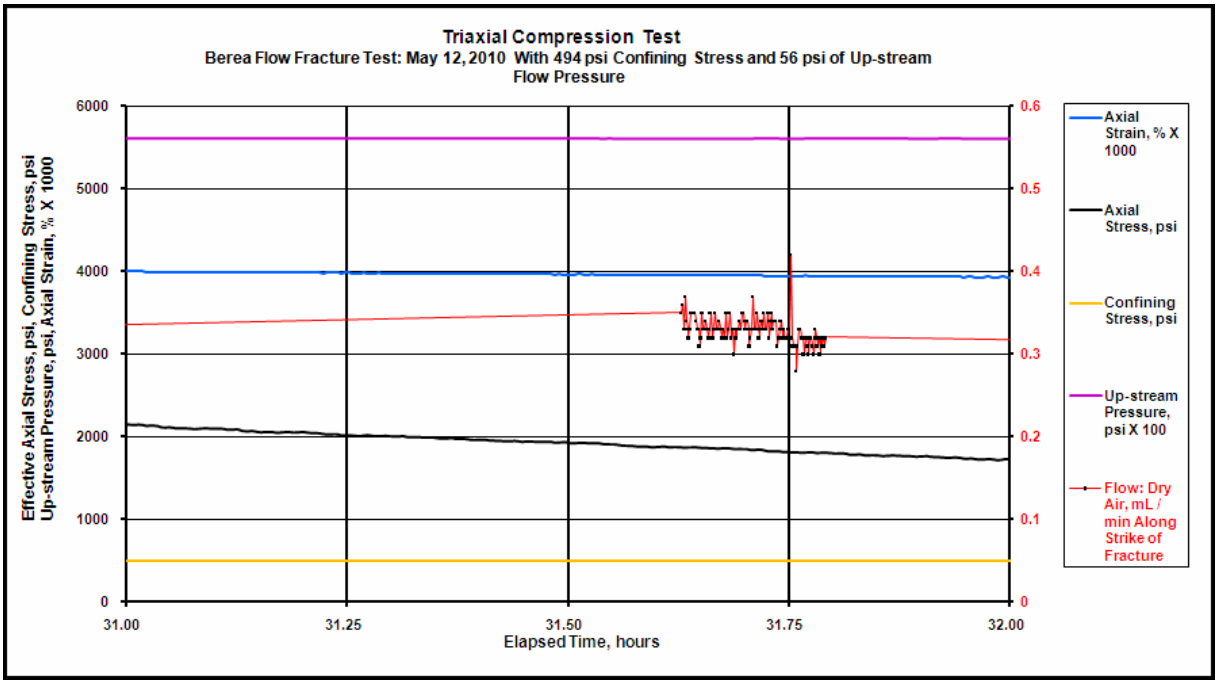
Triaxial Compression Test
Berea Flow Fracture Test: May 12, 2010 With 494 psi Confining Stress and 56 psi of Up-stream Flow Pressure
Effective Axial Stress, psi, Confining Stress, psi
Up-stream Pressure, psi, Axial Strain, % X 1000
6000
5000
4000
3000
2000
1000
0
0.6
0.5
0.4
0.3
0.2
0.1
0
31.00
31.25
31.50
31.75
32.00
Elapsed Time, hours
Axial Strain, % X 1000
Axial Stress, psi
Confining Stress, psi
Up-stream Pressure, psi X 100
Flow: Dry Air, mL / min Along Strike of Fracture

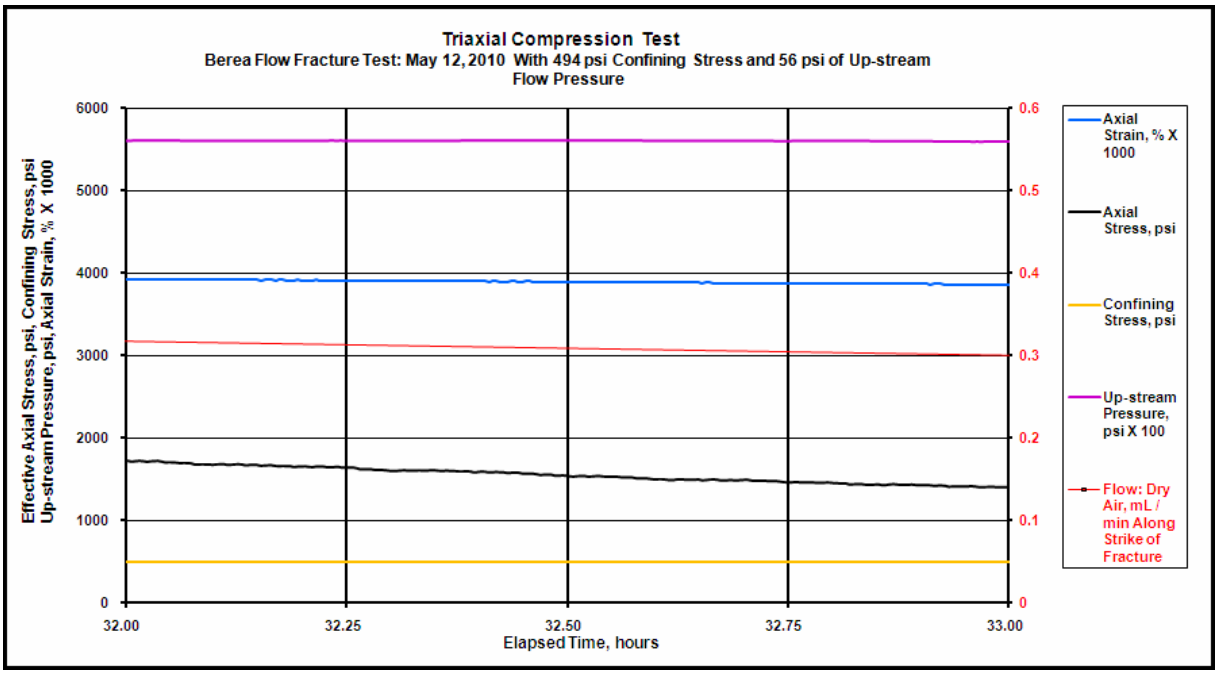
Triaxial Compression Test
Berea Flow Fracture Test: May 12, 2010 With 494 psi Confining Stress and 56 psi of Up-stream Flow Pressure
Effective Axial Stress, psi, Confining Stress, psi
Up-stream Pressure, psi, Axial Strain, % X 1000
6000
5000
4000
3000
2000
1000
0
0.6
0.5
0.4
0.3
0.2
0.1
0
32.00
32.25
32.50
32.75
33.00
Elapsed Time, hours
Axial Strain, % X 1000
Axial Stress, psi
Confining Stress, psi
Up-stream Pressure, psi X 100
Flow: Dry Air, mL / min Along Strike of Fracture

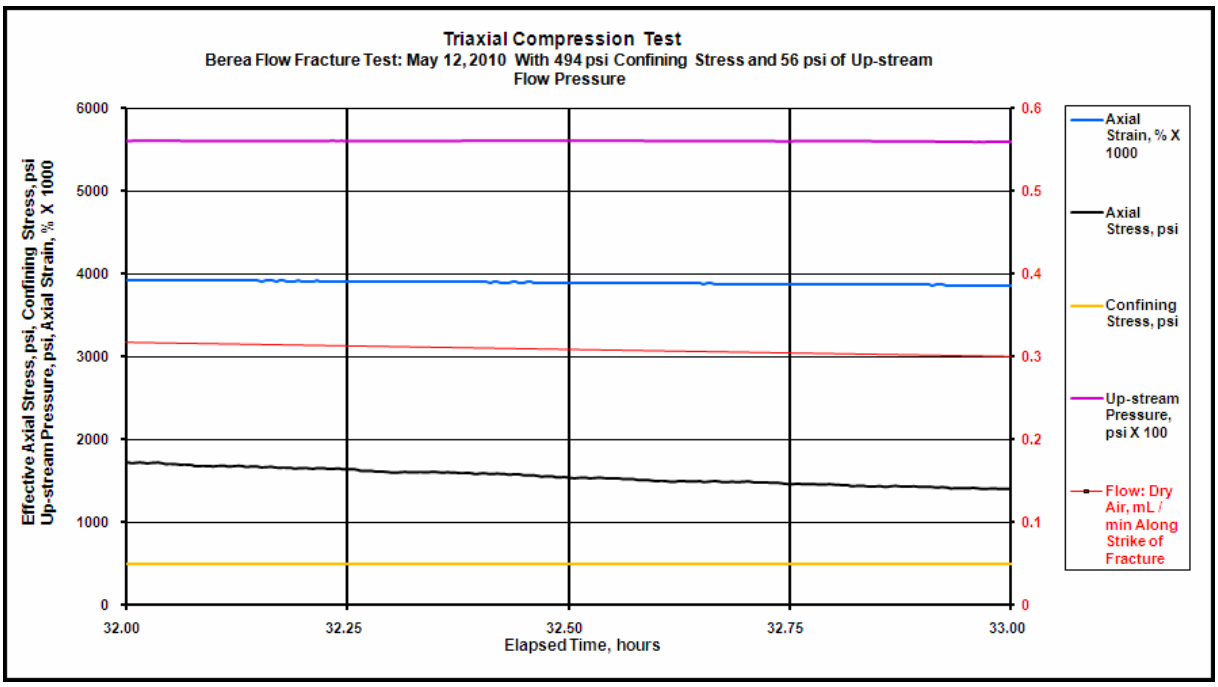
Triaxial Compression Test
Berea Flow Fracture Test: May 12, 2010 With 494 psi Confining Stress and 56 psi of Up-stream Flow Pressure
Effective Axial Stress, psi, Confining Stress, psi Up-stream Pressure, psi, Axial Strain, % X 1000
6000
5000
4000
3000
2000
1000
0
0.6
0.5
0.4
0.3
0.2
0.1
0
32.00
32.25
32.50
32.75
33.00
Elapsed Time, hours
Axial Strain, % X 1000
Axial Stress, psi
Confining Stress, psi
Up-stream Pressure, psi X 100
Flow: Dry Air, mL / min Along Strike of Fracture

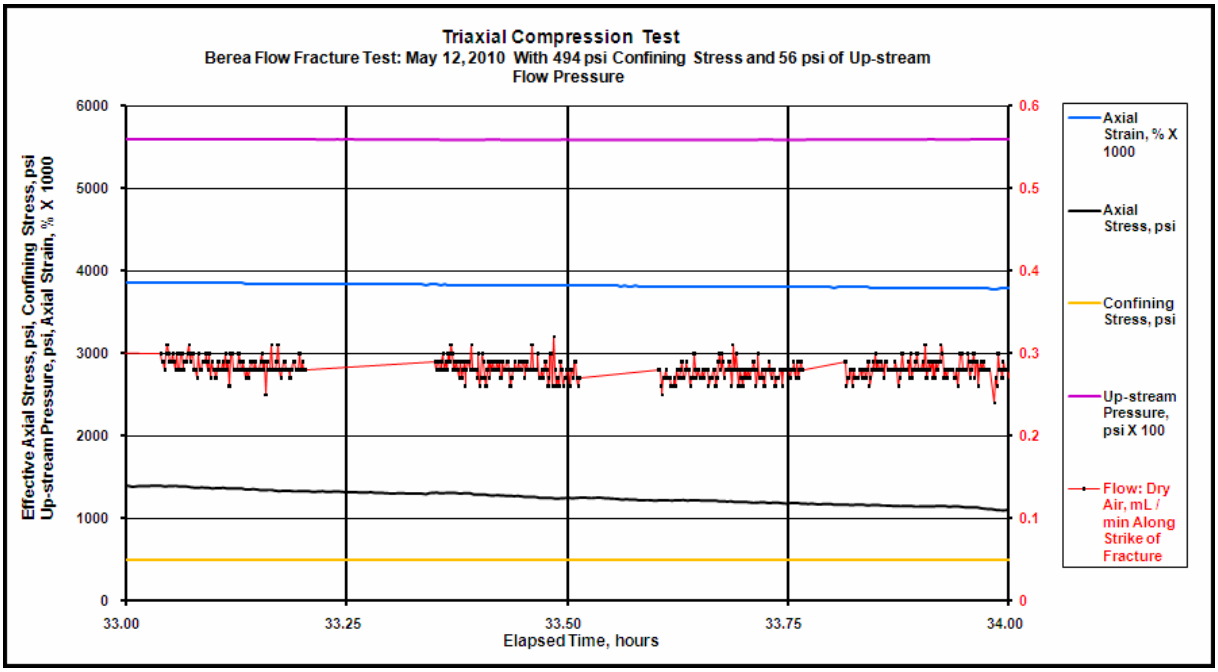
Triaxial Compression Test
Berea Flow Fracture Test: May 12, 2010 With 494 psi Confining Stress and 56 psi of Up-stream Flow Pressure
Effective Axial Stress, psi, Confining Stress, psi Up-stream Pressure, psi, Axial Strain, % X 1000
6000
5000
4000
3000
2000
1000
0
0.6
0.5
0.4
0.3
0.2
0.1
0
33.00
33.25
33.50
33.75
34.00
Elapsed Time, hours
Axial Strain, % X 1000
Axial Stress, psi
Confining Stress, psi
Up-stream Pressure, psi X 100
Flow: Dry Air, mL / min Along Strike of Fracture

Appendix 2:

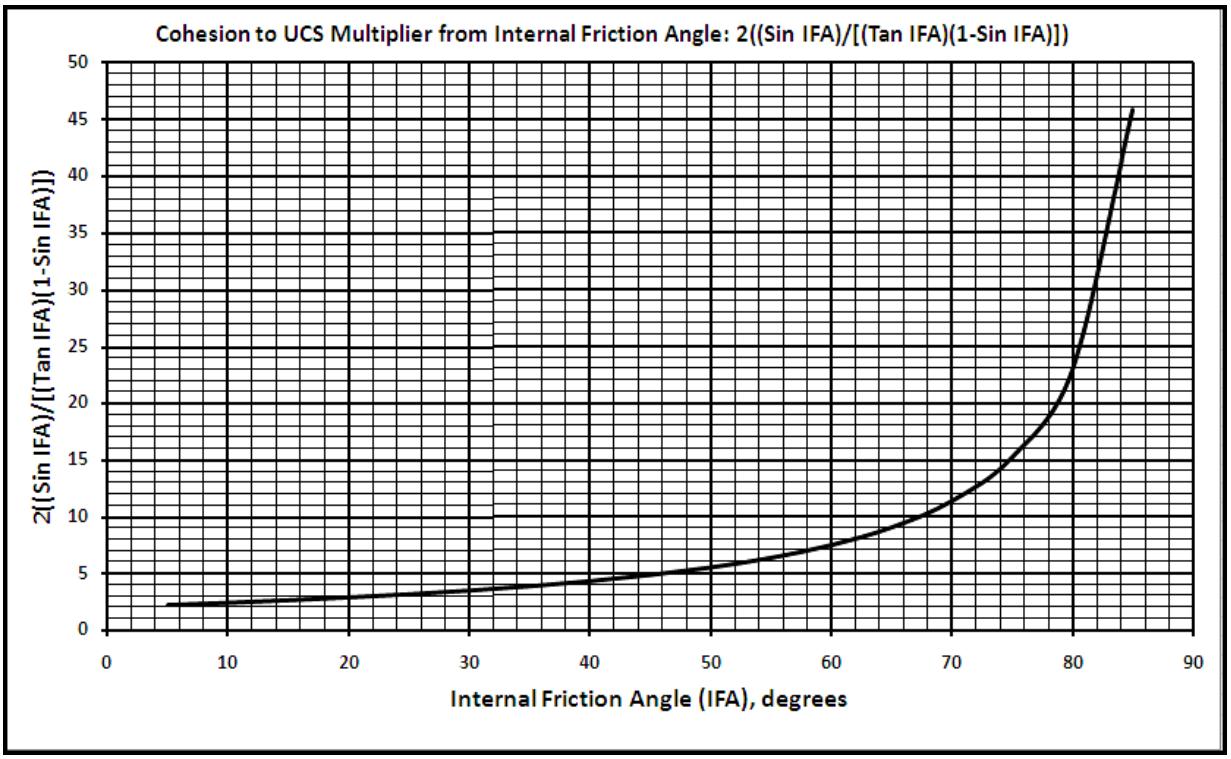
Cohesion to UCS Multiplier from Internal Friction Angle: 2((Sin IFA)/[(Tan IFA)(1-Sin IFA)])
2[(Sin IFA)/[(Tan IFA)(1-Sin IFA)]]
0
5
10
15
20
25
30
35
40
45
50
0
10
20
30
40
50
60
70
80
90
Internal Friction Angle (IFA), degrees

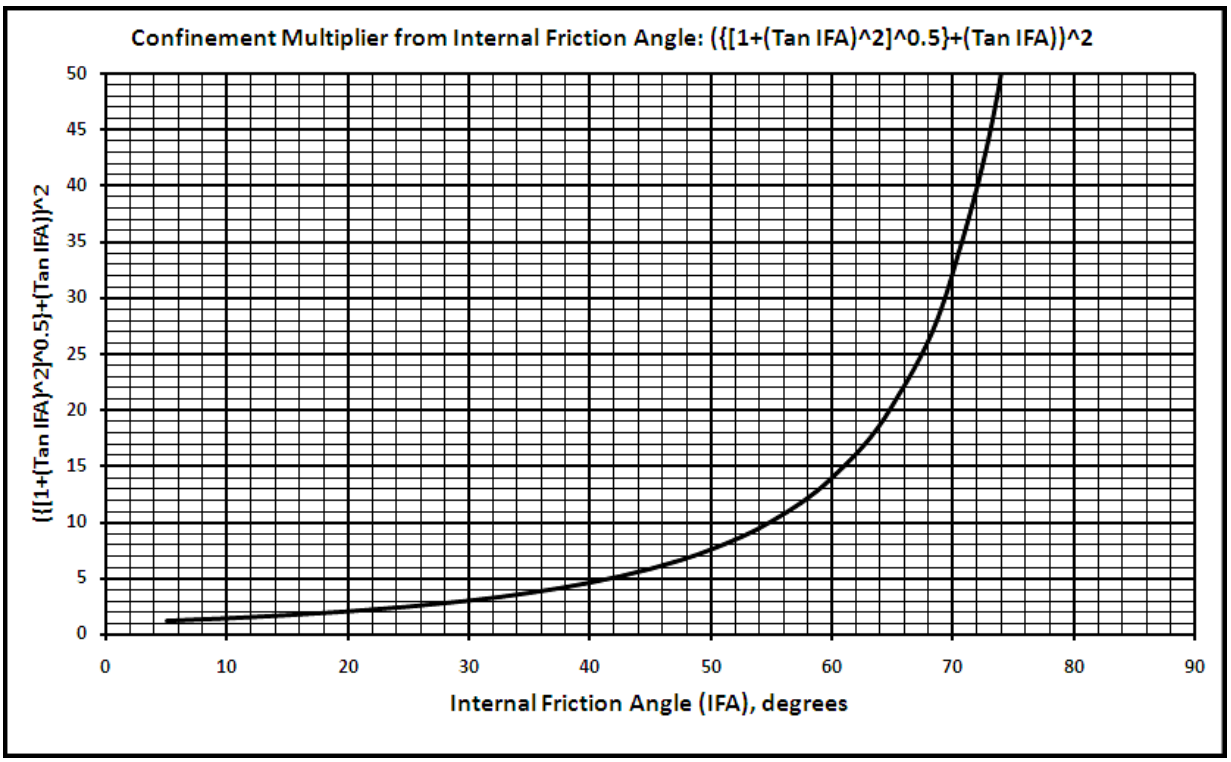
Confinement Multiplier from Internal Friction Angle: ({[1+(Tan IFA)^2]^0.5}+(Tan IFA))^2
({[1+(Tan IFA)^2]^0.5}+(Tan IFA))^2
0
5
10
15
20
25
30
35
40
45
50
0
10
20
30
40
50
60
70
80
90
Internal Friction Angle (IFA), degrees

VITA

Personal Background	Milton Bock Enderlin Born June 21, 1945, San Angelo, TX Son of George and Audrey Enderlin Married to Victoria Travaglini, December 23, 1983
Education	Bachelor of Science in Chemistry, 1977 Sonoma State University, Rohnert Park, CA Bachelor of Science in Geology, 1977 Sonoma State University, Rohnert Park, CA Master of Science in Geology, 2010 Texas Christian University, Fort Worth, TX
Experience	Cryptographic System Specialist, 1966-1969 U.S. Air Force, Texas, Guam, Viet Nam Intern Geologist, 1975-1976 California State Department of Water Resources, Rohnert Park, CA Water Well Engineer's Aide, 1976-1977 Sonoma County Water Agency, Rohnert Park, CA Field Service Operations, 1977-1984: District Manager, General Field Engineer, Regional Engineer, Dipmeter Specialist, Open hole Engineer, Halliburton Logging Services Development Program Coordinator, 1984-1987 Halliburton Logging Services, Fort Worth, TX Manager Laboratory Petrophysics, 1987-1991 Halliburton Logging Services, Fort Worth, TX Petrophysicist, 1991-2004 ConocoPhillips Petroleum Company, Bartlesville,OK Structural Petrophysicist, 2004-2007 ConocoPhillips Petroleum Company, Houston, TX

ABSTRACT

A METHOD FOR EVALUATING THE EFFECTS OF STRESSES AND ROCK STRENGTH ON FLUID FLOW ALONG THE SURFACES OF MECHANICAL DISCONTINUITIES IN LOW PERMEABILITY ROCKS

By Milton Bock Enderlin, M.S. 2010
Department of Geology
Texas Christian University

Dr. Helge Alsleben – Professor of Geology

Changing stress can affect the ability of fluid to flow along mechanical discontinuities such as faults, fractures, or bedding planes. Stress can cause mechanical discontinuity to reactivate in shear, resulting in an increase in fluid flow. The values for present-day horizontal stress orientation and magnitude can be constrained from structural geology principles via interpretation of mapped active features and wellbore information such as drilling history and image logs. Stress magnitudes and orientation information is used to calculate the shear and normal stress magnitudes acting on the mechanical discontinuities of all possible orientations. Furthermore, the necessary magnitudes of fluid pressure within each mechanical discontinuity that would be required to encourage shear failure reactivation are evaluated.

A laboratory experiment and an example from the Barnett Shale play are presented as an application of the method. The Barnett example identifies likely orientations of pre-existing fractures that could interact with fluids during hydraulic fracture stimulation.